STRUCTURAL ANALYSIS OF A COMPOSITE MONOCOQUE CHASSIS FOR USE IN A HIGH PERFORMANCE ELECTRIC VEHICLE

Nicholas Tjebbe Witteveen

Submitted in fulfilment of the academic requirements for the degree of Master of Science in Mechanical Engineering, College of Agriculture, Engineering and Science, University of KwaZulu-Natal

Supervisor: Mr Jean-François Philippe Pitot de la Beaujardiere

Co-Supervisor: Dr Clinton Bemont

Co-Supervisor: Dr Michael Brooks

ABSTRACT

The adoption of electric vehicle technology is becoming more prevalent, as society strives to reduce the negative impact of greenhouse gas emissions and focuses on a sustainable future. This thesis details the design and structural analysis of a carbon composite monocoque chassis for application in a light-weight, high-performance electric vehicle for a South African market, based on the fundamental principles of automotive vehicle design.

Handling characteristics and the design impacts they have on the decisions made in developing a vehicle chassis were explored. The two-dimensional geometry of the chassis structure was developed in the Siemens NX design environment, taking into account the spatial requirements of the mechanical and electrical system components, as well as occupant ergonomics. A zoned-based approach was taken in defining the composite layup for the chassis panels, using material data for locally obtained fabrics and epoxy resin. The chassis' composite lay-up configuration was developed using several static load cases, simulating operational loading, as well as extreme loading arising in certain accident scenarios. The composite structure was analysed, with the first ply composite failure criterion being used to predict failure in the constituent materials. Design refinement was undertaken until the failure criterion predicted structural survivability for all the extreme loading cases considered.

DECLARATION 1 - PLAGIARISM

I, Nicholas Tjebbe Witteveen declare that

1. The research reported in this thesis, except where otherwise indicated, is my original research.
2. This thesis has not been submitted for any degree or examination at any other university.
3. This thesis does not contain other persons' data, pictures, graphs or other information, unless specifically acknowledged as being sourced from other persons.
4. This thesis does not contain other persons' writing, unless specifically acknowledged as being sourced from other researchers. Where other written sources have been quoted, then:

a. Their words have been re-written but the general information attributed to them has been referenced
b. Where their exact words have been used, then their writing has been placed in italics and inside quotation marks, and referenced.

5. This thesis does not contain text, graphics or tables copied and pasted from the Internet, unless specifically acknowledged, and the source being detailed in the thesis and in the References sections.

Signed _____ Date _____

Nicholas Tjebbe Witteveen

As the candidate's supervisor, I agree/do not agree to the submission of this thesis.

Signed _____ Date _____

Mr. Jean-Francois Pitot de la Beaujardiere

As the candidate's co-supervisor, I agree/do not agree to the submission of this thesis.

Signed _____ Date _____

Dr Michael Brooks

As the candidate's co-supervisor, I agree/do not agree to the submission of this thesis.

Signed _____ Date _____

Dr Clinton Bemont

ACKNOWLEDGEMENTS

Firstly I'd like to express my deepest gratitude to my supervisor Mr Jean Pitot, and my co-supervisors Dr Clinton Bemont and Mr Michael Brooks for their guidance, support, and encouragement throughout the course of my research project.

I'd like to thank to Mr Lionel Dedekind from Esteq Pty (Ltd) for his support and assistance with the Siemens NX software and FEA advice in general.

A special thank you to my wife, Carmen, for her unending patience and motivation, and to my family who supported and encouraged me.

The financial assistance of the National Research Foundation (NRF) towards this research is hereby acknowledged. Opinions expressed and conclusions arrived at, are those of the author and are not necessarily to be attributed to the NRF.

CONTENTS

NOMENCLATURE

Symbol

C_1	Front roll stiffness
C_2	Rear roll stiffness
CoG	Centre of gravity
F_f	Vertical load on the front wheels
$F_{f,y}$	Lateral load on the front wheel
$F_{f,y(inner)}$	Lateral load on the inner front wheel
$F_{f,y(outer)}$	Lateral load on the outer front wheel
$F_{f,z}$	Vertical load on the front wheel
$F_{f,z(inner)}$	Vertical load on the inner front wheel
$F_{f,z(outer)}$	Vertical load on the outer front wheel
F_r	Vertical load on the rear wheels
$F_{r,y}$	Lateral load on the rear wheel
$F_{r,y(inner)}$	Lateral load on the inner rear wheel
$F_{r,y(outer)}$	Lateral load on the outer rear wheel
$F_{r,z}$	Vertical load on the rear wheel
$F_{r,z(inner)}$	Vertical load on the inner rear wheel
$F_{r,z(outer)}$	Vertical load on the outer rear wheel
F_y	Force in the lateral direction
F_z	Force in the vertical direction
g	Gravitational acceleration
h	Centre of gravity vertical height
h'	Distance from the roll axis to the CoG
k_1	Front shock stiffness
k_2	Rear shock stiffness
$k_{chassis,f}$	Final chassis torsional stiffness
$k_{chassis,i}$	Initial chassis torsional stiffness
L	Wheelbase
L_f	Longitudinal distance from CoG to front wheel contact patch
L_r	Longitudinal distance from CoG to rear wheel contact patch
m	Vehicle mass
m_b	Vehicle sprung mass

R_c	Cornering radius
s_1	Front shock track
s_2	Rear shock track
t	Vehicle track
t_1	Front track
t_2	Rear track
t_l	Lateral distance from CoG to left hand side wheel contact patch
t_r	Lateral distance from CoG to right hand side wheel contact patch
α	Kingpin inclination angle
v	Velocity
φ	Body roll

Abbreviations

2DS	Two degree scenario
B2DS	Beyond two degree scenario
CFRP	Carbon fibre reinforced polymer
DOF	Degree of freedom
EV	Electric vehicle
FEM	Finite element method
FPF	First ply failure
GFRP	Glass fibre reinforced polymer
GHG	Greenhouse gas
ICE	Internal combustion engine
LPF	Last ply failure
PAN	Polyacrylonitrile
PHEV	Plug-in hybrid electric vehicle
RTM	Resin transfer mould

LIST OF FIGURES

LIST OF TABLES

CHAPTER 1

Introduction

1.1 Background

In the automotive industry there are two main driving factors for new technology and material development: vehicle weight and cost. A global focus on pollution reduction and the impact CO_2 emissions are having on the environment has led to the development of more efficient vehicles, through the implementation of stricter regulations.

For vehicles with internal combustion engines (ICE's) fuel economy is directly linked to CO_2 emissions, a decrease in fuel consumption per kilometre (l/km) decreases CO_2 emissions measured in grams per kilometre (g/km). After energy losses in the engine due to heat and mechanical inefficiencies, and losses in the transmission due to mechanical inefficiency, the usable energy at the wheels goes to overcoming tractive forces. The tractive force comprises of tyre rolling resistance, acceleration or braking force, and aerodynamic drag. Tyre rolling resistance, acceleration or braking, and the force required to climb a gradient are directly impacted upon by the mass of the vehicle. By reducing vehicle mass the tractive force decreases, which in turn decreases the fuel consumption. A 10% reduction in mass can reduce the fuel consumption by approximately 7% (Cheah, 2010).

While designing more efficient ICE vehicles is a step in the right direction for reducing society's carbon emissions, eventually fossil fuel powered drivetrains need to be replaced with more sustainable methods. The global focus on a sustainable future has been the driving force behind electric vehicles (EV's), due to their reduced carbon emissions, with many governments implementing policies to promote renewable forms of transportation. Since EV's are driven by stored energy in battery packs, there are no carbon emissions, however many EV's are still charged through electricity generated by burning fossil fuels. Coupling EV's with renewable methods of charging would have the largest impact in reducing carbon emissions.

Enforced in November 2016, the Paris Agreement (United Nations Framework Convention on Climate Change, 2015), which is an agreement within the United Nations Framework Convention on Climate Change signed by 195 countries, set the objective of holding the global average temperature rise to below 2°C above the average temperature of Earth before the industrialisation of society. This objective is referred to as the 2 degree scenario (2DS). The Paris agreement also aims at pursuing limiting the global average temperature rise to below 1.5°C above pre-industrial

levels, which is referred to as the beyond 2 degree scenario (B2DS). In order to achieve the 2DS, or even the B2DS, various sectors in society will have to become more efficient and reduce their greenhouse gas (GHG) emissions. Figure 1-1 shows the predicted reduction of GHG emissions by sector to 2050, as outlined in the 2DS. With the transportation sector accounting for 23% of the energy sectors emissions, EV's can play a vital role in the reduction of global emissions and in achieving the desired 18% reduction in GHG emissions in 2050 for the transportation sector.

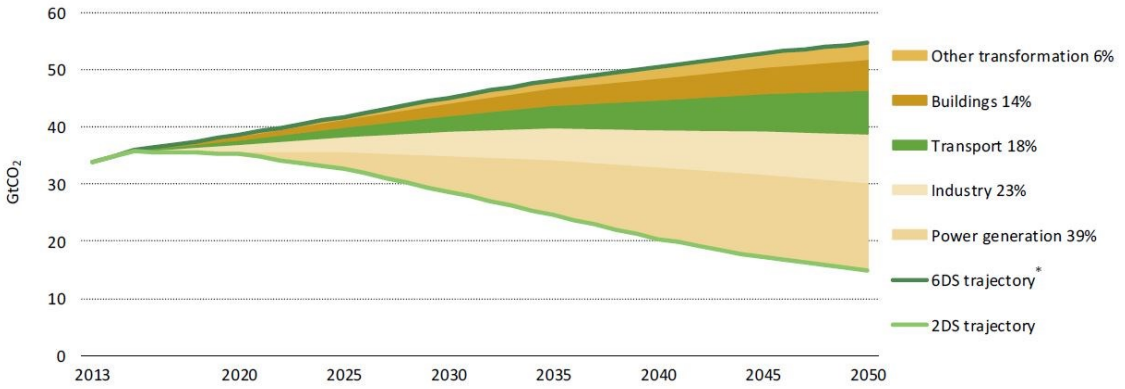

Figure 1-1. GHG emissions reductions by sector (International Energy Agency, 2016).

In order to achieve these targets the 2DS requires a global EV deployment of roughly 70 million vehicles by 2025, with the B2DS requiring 90 million by the same year (International Energy Agency, 2017).

Governments are not the only ones supporting the transition from ICE's to EV's. Recently automakers have been developing electric alternatives to their products and setting ambitious goals for the future. Ford plans to release thirteen electrified vehicles into the market by 2020, including an SUV with a range of at least 300 miles (Ford, 2017, Jan 3). Toyota has aimed to sell more than 5.5 million electrified vehicles per year by 2030 (Toyota, 2017, Dec 18). Volkswagen plans to release an electric version of 300 vehicle models by 2030 ("Volkswagen plans electric option for all models by 2030," 2017, Sept 11). Tesla aims at producing 5000 vehicles per week by the end of the first quarter of 2018, produce 1 million vehicles per year by 2020, and introduce a compact SUV by the same year (Thompson, 2017, Nov 15). BMW aims at releasing twelve new EV's by 2025, with a shorter term goal of selling 500 000 hybrid EV's by 2019 (Sheahan, 2017, Dec 21). GM plans to release twenty new EV models by 2023, including two all-electric vehicles by early 2019 (Waldmeir, 2017, Oct 2).

Two major barriers to the growth of the EV market are lower range and higher purchasing cost, but as key technologies are being developed these barriers may soon be mitigated. Research released by Bloomberg New Energy Finance predicts that by 2040 EV's will make up 54% of new car sales and account for a third of the world's vehicles. Bloomberg New Energy Finance also predicts that EV's will become price competitive from 2025 (Bloomberg New Energy Finance, 2017). The increased adoption of EV's is promoted by several factors, including consumer acceptance, increased commitments from automakers, regulatory support in key markets, and decline in battery cost. As can be seen in Figure 1-2 battery costs have reduced 73% between 2008 and 2015, while energy densities have increased by 391% over the same time period. This translates to an increased vehicle range, reducing range anxiety in drivers, and lower vehicle cost.

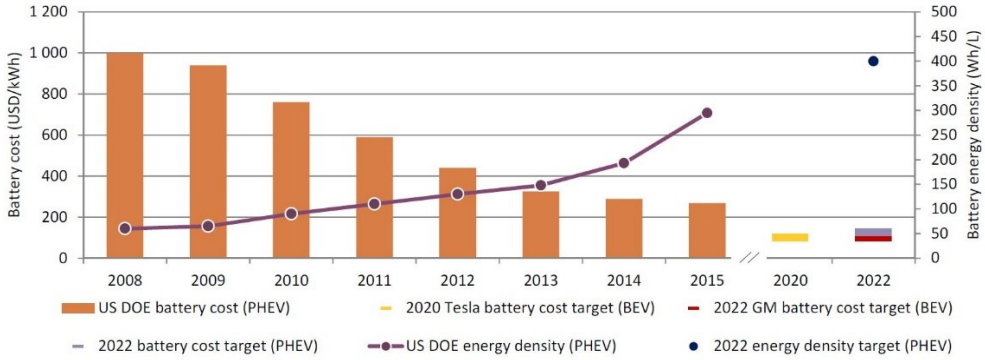

Figure 1-2. Evolution of battery energy density and cost (International Energy Agency, 2016).

With governments and automakers backing the transition from ICE's to EV's, coupled with the reduction in cost of key technologies and higher consumer confidence, it is an opportune time for South Africa to investigate how EV's can positively impact personal transport and our economy.

1.2 The Mamba EV

The Mamba EV project is an initiative that aims at lowering the barrier to electric vehicle use in South Africa, and promoted the growth of a local EV manufacturing industry. The project strategy is to first develop a low production volume, light-weight, and performance EV to establish a sustainable position in the local transport industry, and then progress to developing a more cost effective alternative to personal transport. Initially a prototype EV would be produced to allow for the extensive testing of subsystems as well as novel manufacturing methods.

1.3 Chassis Development

A key aspect in the development of a prototype EV is the structure that encompasses all other subsystems of the vehicle. With mass optimisation being critical in achieving the desired vehicle performance and minimising material cost, composites have become integral with chassis design. By reducing the mass of the body and chassis the load on components such as suspension is reduced, along with the required energy to achieve the same level of vehicle performance. This allows for a reduction in engine or motor size, which results in a reduction to the drivetrain mass, creating a knock-on effect. Carbon fibre chassis have become synonymous with modern high performance supercars, to the extent that the use of the material has significant marketing implications. The project team decided to develop a carbon fibre composite monocoque chassis for the Mamba EV, and had a strong belief that the chassis could be produced more affordably by exploring novel manufacturing methods.

In order to manufacture a prototype composite monocoque chassis structural analysis would need to be done to ensure the chassis could withstand all the loading that would be experienced under normal driving conditions, as well as irregular shock loading, such as pothole or kerb impacts which cause high loading but are not an everyday occurrence. The Siemens NX 10.0 software, which is capable of facilitating finite element analysis of composite structures, was applied for design and analysis purposes.

1.4 Objectives

1. To develop a geometric model of the chassis, allocating space for all internal components. This will be an iterative process as components are selected. Placement of the internal components heavily effects the mass distribution which is critical in vehicle handling.

2. To ensure that the suspension mounts prioritise handling. The position of the mounts influences the various suspension settings, which in turn vary the handling of the vehicle.

3. To discretise the geometric model and define material properties so as to accurately represent the structure to be manufactured.

4. To analyse the response and behaviour of the model subjected to expected worst case scenario loading conditions, ensuring the survivability of the structure.

1.5 Chapter Breakdown

This thesis incorporates nine chapters. The contents of the chapters that follow-on from this introductory chapter are as follows:

Chapter 2 reviews prior research and theory related to chassis design and vehicle handling, in addition to composite manufacture, composite finite element analysis, and composite fracture and failure.

Chapter 3 defines the iterative approach taken to develop the carbon composite monocoque chassis.

Chapter 4 details the approach taken to develop the geometry for the initial chassis, incorporating the spatial analysis, and the initial internal structure and outer body integration.

Chapter 5 details the pre-processing of the model. This includes surface refinements to remove discontinuities once the model was meshed, material definition, initial lay-up prediction, and mesh independence. The chapter also indicates the applied constraints, loads, and results on the initial chassis structure for each of the driving load cases.

Chapter 6 discusses the refinements to the geometry and lay-up based on the results of chapter 5, as well as the final results for the load cases, indicating the survival of the chassis.

Chapter 7 details the manufacturing process of the carbon composite monocoque chassis and the assembly of the mechanical and electrical systems of the vehicle.

Chapter 8 discusses and evaluates the results of the final simulations, before Chapter 9 concludes the thesis as well as highlights recommended areas of improvement for a potential second iteration of the electric vehicle.

CHAPTER 2

Literature Review

2.1 Chassis Design

A chassis is a structure whose function is to connect the wheels to the vehicle and absorb all the torsion and bending loads the vehicle experiences, while neither sagging, twisting, nor deflecting excessively (Costin & Phipps, 1961). The chassis needs to be able to support all the required components of the vehicle and offer adequate mounting points.

2.1.1 Contemporary Chassis Designs

Several types of chassis designs are currently used in vehicles. The defining characteristics of each design may remain constant, however, the method of manufacture and materials used are constantly changing as new developments arise. For instance, composite body vehicles are becoming more prevalent in modern designs.

Space Frame

A space frame chassis comprises of circular or rectangular cross section tubing welded together to form a triangulated structure. In an ideal or true space frame chassis all the joints could be flexible without the structure losing stiffness (Costin & Phipps, 1961). The loading at the joints should have no bending moments, and should therefore only be subject to tension and compression forces (Costin & Phipps, 1961). Space frames are lightweight, have a high torsional stiffness, and can be assembled with simple welding. However due to the complexity of the manufacturing process, automated manufacture is not achievable. Due to a high manufacturing time and the inability to be produced in an automated process, space frame chassis are limited to low volume production. Figure 2-1 shows a space frame chassis for a Factory Five GTM Supercar (FactoryFive, n.d.).

Figure 2-1. Space frame chassis (FactoryFive, n.d.).

Ladder

One of the more simple chassis designs is the ladder frame chassis. This design incorporates two main longitudinal beams with several cross members to form the load bearing structure of a vehicle. The ladder chassis offers good beam stiffness and is relatively easy to manufacture, however the design has a poor torsional stiffness. The torsional stiffness can be improved using cross members and by adding the body, however convertible car bodies have less of an effect as the roof helps to stiffen the assembly (Adams, 1992). Figure 2-2 shows a custom designed ladder chassis by Art Morrison Enterprises (Art Morrison, n.d.).

Figure 2-2. Ladder chassis (Art Morrison, n.d.).

Backbone

A backbone chassis incorporates a main central support member, linking the front and rear axles, which is usually a tubular beam with a rectangular or circular cross section. Since the support member is hollow, the drive shaft of the vehicle can be placed within it. Due to the chassis being required to fit within the centre of the body, the stiffness is limited by the size the support member's cross section, which can be made larger until it encroaches on the vehicles interior space. With the structural member being at the centre of the structure, the chassis offers little protection from side collisions and the vehicle has to rely on the body of the vehicle for passenger safety. Figure 2-3 shows the backbone chassis of a Toyota 2000GT (The Truth About Cars, n.d.).

Figure 2-3. Toyota 2000GT backbone chassis (The Truth About Cars, n.d.).

Monocoque

A monocoque chassis is a single structure, a combination of the body and chassis, in which the surface panels carry stresses of the vehicle in shear, as well as define the vehicle shape. This approach to chassis design is highly space efficient, since there is no need for a central box or high sills, and offers a good crash protection for the passengers. Crumple zones can be incorporated into the design to increase occupant safety. Steel monocoque chassis have a low manufacturing cost for high-volume production, however for low-volume production the initial costs for the tooling and machinery is too high for it to be viable. Steel monocoque chassis are produced by welding pressed panels together to form the single structure, which can be robotised allowing for a rapid production time per chassis. The downside to steel monocoque chassis is their high mass, which can be overcome by using other materials such as aluminium and various composites which drastically reduce the mass while maintaining the structural strength and stiffness. These chassis can be full or semi monocoque, with the semi monocoque chassis typically incorporating space frame sub-structures. Figure 2-4 shows a carbon fibre reinforced polymer monocoque chassis for the Porsche 918 Spyder (AUSmotive, 2013).

Figure 2-4. *Porsche 918 Spyder* CFRP monocoque chassis (AUSmotive, 2013).

2.1.2 Current Market Trends

With the aim of the project being to develop a light-weight, high performance EV, an understanding of the design methods used for high performance vehicle chassis in the global market was critical. A review of high performance EV's and plug-in hybrid electric vehicles (PHEV's) was performed with a focus on chassis structures within the selected group. Table 2-1 shows the chassis type's used for the selected vehicles.

Table 2-1. Chassis used for production high performance EV's and PHEV's

Vehicle	Chassis Type
Koenigsegg Regera[1]	Carbon fibre monocoque tub
Tesla Model S[2]	Aluminium unibody chassis
Porsche 918 Spyder[3]	Carbon fibre monocoque tub
Mclaren P1[4]	Carbon fibre monocoque tub
Rimac Concept 1[5]	Cromoly steel space frame chassis
Ferrari LaFerrari[6]	Carbon fibre monocoque tub
BMW i8[7]	Two part structure, incorporating an aluminium chassis and a structural passenger cell made from carbon fibre

From the table it can be seem that the CFRP monocoque tub design is popular across a variety of manufacturers, utilising light-weight honeycomb cores and pre-impregnated carbon fibre fabrics in order to produce mass efficient and stiff structures. Drilled and tapped inserts are placed within the layup of the tub structure for mounting components. For the CFRP monocoque tub chassis the sub frames are either made from CFRP, as seen in the Porsche 918 Spyder (Figure 2-5), or a metal cross bracing, as seen in the Koenigsegg Regera (Figure 2-6).

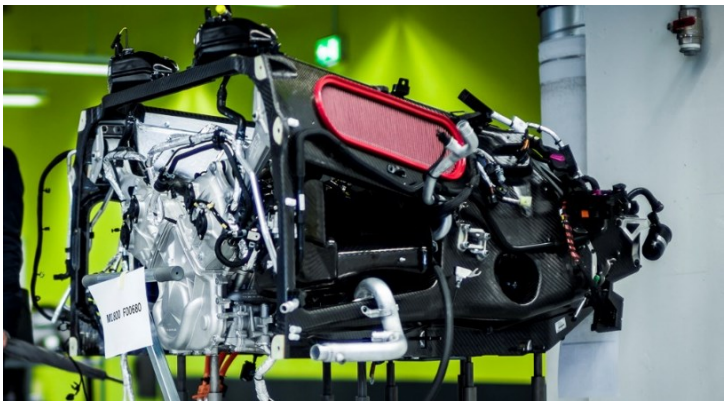

Figure 2-5. Rear CFRP sub frame of the Porsche 918 Spyder (Barnett, 2014).

[1] (Koenigsegg, n.d.)
[2] (Tesla, n.d.)
[3] (Barnett, 2014)
[4] (McLaren, n.d.)
[5] (RIMAC, n.d.)
[6] (Ferrari, n.d.)
[7] (BMW, n.d.)

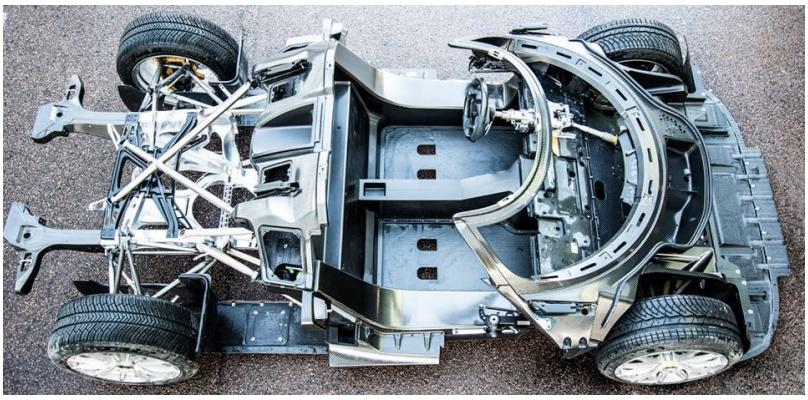

Figure 2-6. Chassis structure of the Koenigsegg Regera (Tutu, 2016).

A common feature across many of the CFRP monocoque tub designs in the use of aluminium crumple zones, coupled to the tub, for energy absorption in crashes, seen in Figure 2-7.

Figure 2-7. McLaren P1 chassis (Kong, 2013).

2.2 Vehicle Handling

Vehicle handling can be described as the way in which a vehicle responds to inputs from the driver while in operation. Various factors contribute to 'good handling', where the vehicle has good traction, and is highly responsive to the driver's inputs.

2.2.1 Slip Angle

While cornering a vehicle, as the tyre turns, the contact patch deforms due to the elastic nature of rubber, and lags behind the position of the wheel. The difference in angle between the treads of the contact patch and the direction of the wheel is known as the slip angle. Due to adhesion and hysteresis, as the slip angle increases the co-efficient of friction increases. This results in a higher lateral load, up to a point where the tyre is at its elastic limit and any further increase to the slip angle causes a loss of traction (Puhn, 1976).

Oversteer and understeer

Slip angle differences between the rear and front tyres results in the vehicle either understeering or oversteering. If the slip angle is larger on the rear tyres, the vehicle will oversteer, while if the slip angle at the front tyres is greater the vehicle will understeer. In cornering, a vehicle that understeers will drift outward away from the centre of rotation, increasing the radius of rotation which reduces the lateral loading on the wheels. A vehicle that oversteers in cornering will turn in towards the centre of rotation, reducing the radius of rotation which increases the slip angle. If this isn't corrected, eventually the lateral load will exceed the centrifugal force causing the vehicle to spin-out. With regards to handling, neutral steer is considered ideal, however it is not always achievable. In cases where neutral steer cannot be achieved, it is considered safer for standard road vehicles to understeer, whereas for track-racing vehicles, a skilled driver has more control in corners with oversteer (Puhn, 1976).

2.2.2 Roll Centre

A vehicle's mass can be divided into two mass categories, sprung and un-sprung mass. The sprung mass is all the mass of the components that is supported by the spring and damper. Conversely the un-sprung mass comprises of the mass of all the components not supported by the spring and damper. Since the sprung mass is not rigidly linked but is supported by compressible spring and damper, it can rotate relative to the ground plane, causing higher compression in the springs on one side of the vehicle. Lateral rotation of the sprung mass is called 'roll'. The roll centre of a vehicle is the theoretical point that the sprung mass will rotate around when experiencing a lateral load. The front and rear of the vehicle have their own roll centres which, if connected with a straight line, result in the roll axis. The front and rear roll centres are determined by the suspension type and geometry.

Two main types of independent suspension systems will be explored in this review, as seen in Figure 2-8, the double wishbone suspension and the MacPherson suspension. For the MacPherson suspension system the roll centre is calculated by extending a line from the centre of the wheel contact patch to where a plane running parallel with the suspension 'A' arm and a plane running orthogonal to the shock absorber intersect, as seen in Figure 2-9. The roll centre of a double wishbone suspension system is calculated by extending a line from the centre of the wheel contact patch to where planes running parallel with the suspension arms intersect. The roll centre is the intersection point of the extended line and the centre line of the vehicle body, as shown in Figure 2-10. (Happian-Smith, 2001).

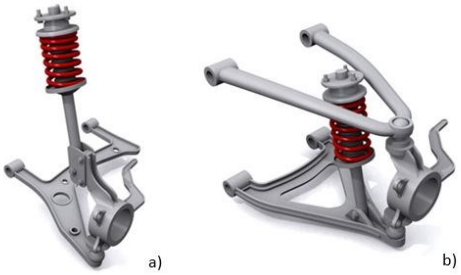

Figure 2-8. Independent suspension types: a) MacPherson, b) Double Wishbone (Speed Industries, 2011).

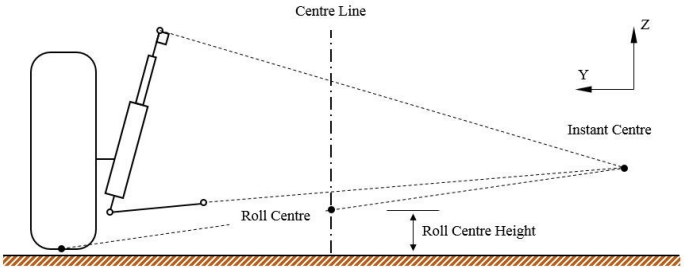

Figure 2-9. MacPherson suspension roll centre.

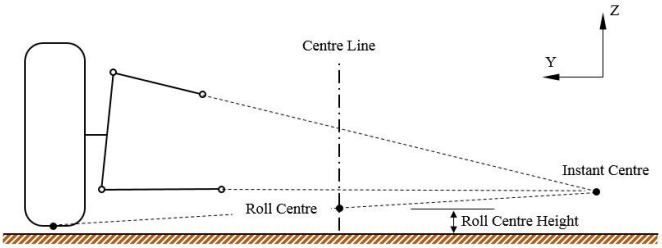

Figure 2-10. Wishbone suspension roll centre.

2.2.3 Centre of Mass

The centre of mass is the point in a body where the weighted position of the mass sums to zero. The centre of mass and the centre of gravity coincide if a body is in a uniform gravitational field (Beatty, 2006).

2.2.3.1 Static Weight Distribution

The weight distribution of a vehicle is the percentage of vehicle mass that is imposed on each wheel, which is determined from the vehicle's centre of gravity. The static front and rear distribution is calculated by taking a ratio of the distance in the x-direction from the centre of gravity to the front or rear axle and the wheelbase of the vehicle, as seen in Figure 2-11. The static lateral distribution is calculated by taking the ratio of the distance in the y-direction from centre of gravity to the contact patch of the left or right wheels and the vehicle track, as seen in Figure

2-12. Static weight distribution is applicable when the vehicle is at rest or moving in a straight line at constant velocity. Longitudinally it can be calculated by,

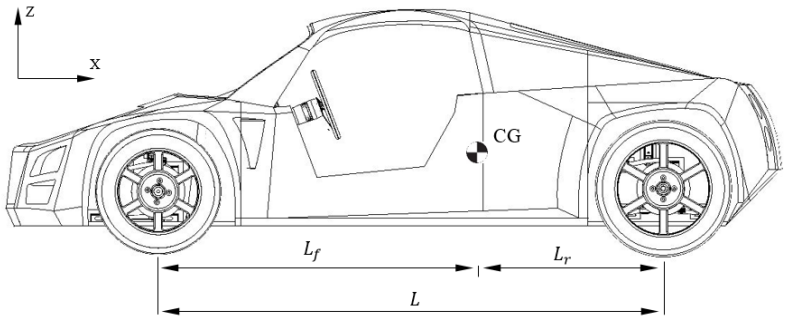

Figure 2-11. Front and rear weight distribution.

$$\%\, Weight\ on\ Front\ Tyres = \frac{L_r}{\mathrm{L}} \times 100 \tag{2.1}$$

$$\%\, Weight\ on\ Rear\ Tyres = \frac{L_f}{L} \times 100 \tag{2.2}$$

and laterally by,

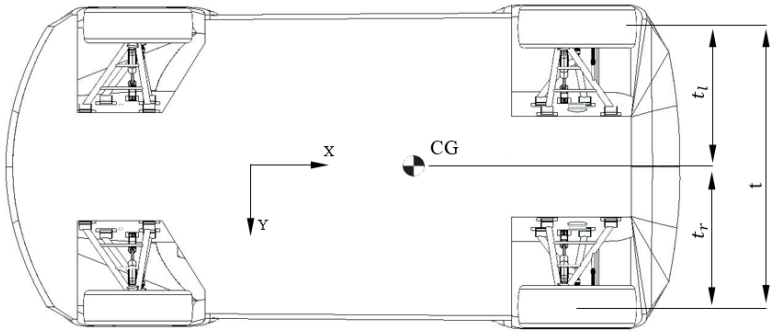

Figure 2-12. Left and right weight distribution.

$$\%\, Weight\ on\ Left\ Tyres = \frac{t_r}{t} \times 100 \tag{2.3}$$

$$\%\, Weight\ on\ Right\ Tyres = \frac{t_l}{t} \times 100 \tag{2.4}$$

2.2.3.2 Body Roll

In cornering a vehicle experiences a centripetal force which acts at the centre of gravity. The induced moment results in a transfer of mass to the outer wheels, increasing the load, while reducing the mass on the inner wheels. The centripetal force causes the sprung mass to 'roll' or

rotate about the instantaneous roll axis, compressing the shocks of the outer side of the vehicle. The weight transfer affects the slip angle of the tyres which causes roll steer, which will be discussed in section 2.2.6.

Body roll, φ, can be calculated using the front and rear roll stiffness's, C_1 and C_2, the sprung mass, m_b, the radius of curvature, R_c, the vehicles velocity, v, and the distance between the roll axis and the centre of mass, h' (Pauwelussen, 2014). This results in,

$$\varphi = \frac{m_b\, h'}{C_1 + C_2 - m_b\, h'} \frac{v^2}{g\, R_c} \tag{2.5}$$

2.2.3.3 Front and Rear Transfer

Inertia forces act upon a vehicle in both acceleration and in braking causing a longitudinal mass transfer, increasing the load on the front or rear axle. In braking the inertial force, ma, acts on the centre of mass in the direction of motion, as seen in Figure 2-13, resulting in mass being transferred forwards onto the front axle (Meywerk, 2015).

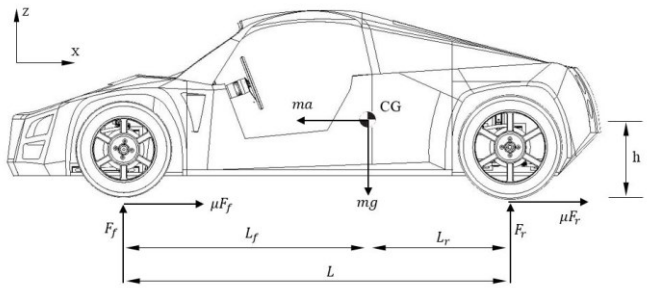

Figure 2-13. Vehicle loading while braking.

The loads at the axles can be calculated by summing the moments about the front and rear contact patches,

$$F_r = \frac{m}{L}\left(g\, L_f - a\, h\right) \tag{2.6}$$

$$F_f = \frac{m}{L}\left(g\, L_r + a\, h\right) \tag{2.7}$$

When a vehicle accelerates the inertial and frictional forces act in the opposite direction to the braking loading. This results in a rearward mass transfer, increasing the loading on the rear axle. In this case the loads at the axles can be calculated by summing the moments about the front and rear contact patches,

$$F_r = \frac{m}{L}\left(g\, L_f + a\, h\right) \tag{2.8}$$

$$F_f = \frac{m}{L}\left(g\, L_r - a\, h\right) \tag{2.9}$$

2.2.3.4 Polar Moment of Inertia

The polar moment of inertia of a vehicle is a measurement of the resistance to the change of direction of the vehicle. The polar moment of inertia is calculated by multiplying the mass of the individual components by the square of their distance to the centre of mass of the vehicle. The further the bulk of the mass of the vehicle is away from its centre of mass, the higher the polar moment of inertia, which results in a higher resistance to steering inputs. However a vehicle with a high polar moment of inertia also tends to be more stable at higher speeds (Puhn, 1976).

2.2.4 Caster Angle

The caster angle is the angle between the steering axis and the line perpendicular to the road surface through the contact patch, as seen in Figure 2-14, a). If the contact patch of the tyre is behind where the steering axis intersects the ground plane, the caster is considered positive, conversely, if the contact patch of the tyre is behind where the steering axis intersects the ground plane, the caster is considered negative. As the steering is turned the wheel pivots about the steering axis, resulting in the contact patch shifting to the side of the direction of travel. This creates a self-aligning force which aids in the straightening of the wheels after a turn, as seen in Figure 2-14 (Puhn, 1976).

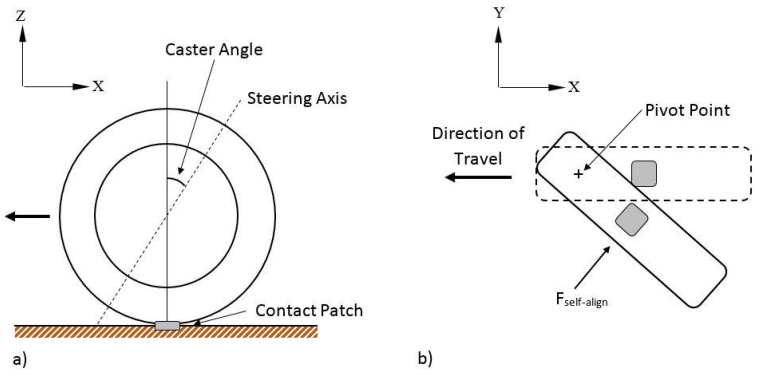

Figure 2-14. a) Caster angle, b) Self-aligning force while wheel is turning.

2.2.5 Kingpin Angle and Scrub Radius

The kingpin inclination angle is the angle between the axis perpendicular to the road and the steering axis that runs between the pivot points on the suspension. The scrub radius is the distance from the point at which the steering axis intersects the ground plane and the centre of the contact patch. The kingpin inclination angle and the scrub radius can be seen in Figure 2-15.

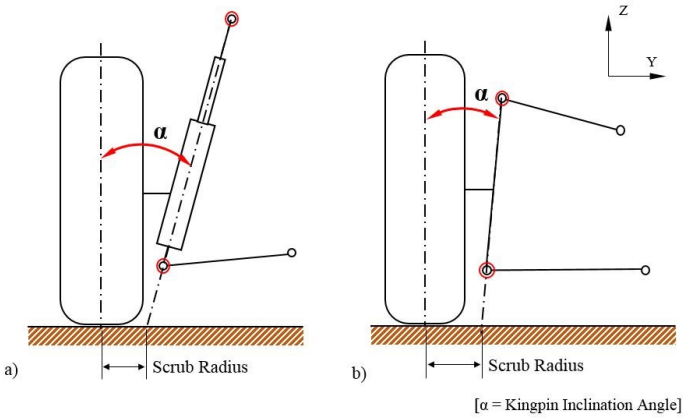

Figure 2-15. Kingpin inclination and scrub radius: a) MacPherson, b) Double Wishbone.

The scrub radius can affect the handling and steering 'feel' of the vehicle. There are three options for setting the scrub radius, positive, negative, and zero scrub. If the steering axis intersects the ground plane on the outside of the contact patch centre the scrub radius is negative, conversely if the steering axis intersects the ground plane on the inside of the contact patch centre the scrub radius is positive (Adams, 1992; Reimpell, Stoll, & Betzler, 2001). If the steering axis intersects the centre of the contact patch there is zero scrub radius. Any loads experienced by the contact patch, such as the loads during braking and acceleration, cause the wheel to twist about the steering axis, inducing a moment. The larger the scrub radius the larger the moment. This steering moment can cause a dynamic toe angle change and additional suspension component loading.

2.2.6 Toe Angle

The toe angle is the angle between the direction of travel and the centre plane of the wheel, as seen in Figure 2-16. The toe setting of a wheel impacts the slip of the tyre and the steering characteristics of the vehicle. Road interaction forces acting on the contact patch of the tyre can cause variations in toe angle, due to deflections in the rubber bushings, which are often used to damp some of the road vibrations. Depending on the scrub radius setting of the suspension the toe change can either be positive or negative, and the toe will be set to counteract the changes while driving.

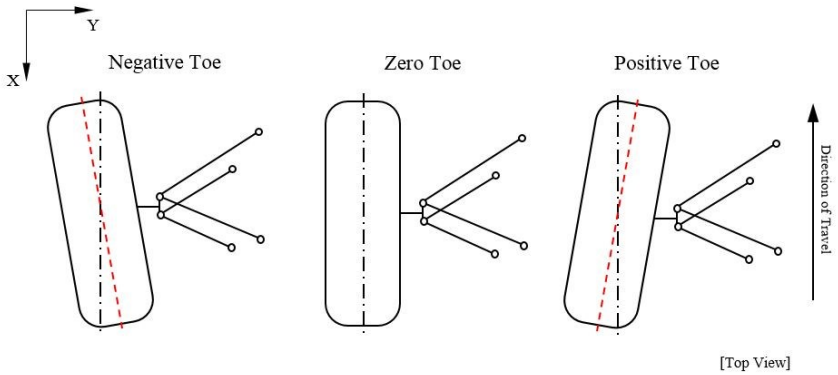

Figure 2-16. Toe angle settings.

The toe setting can also change as the suspension moves vertically, which is called bump steer, and as the body rolls in cornering, which is called roll steer. Ideally one would want zero bump steer as it has negative effects on handling and steering, which are more pronounced at higher speeds. Roll steer is caused by the weight transfer in cornering, which alters the slip angle at the tyres. The outer tyres experience an increased load which increases the slip, where the converse is true of the inner tyres. Roll steer can be used to change oversteer and understeer characteristics of a vehicle, in order to counteract inherent design characteristics, however large differences in the outer and inner wheel slip angles can drastically reduce handling of the vehicle (Puhn, 1976).

2.2.7 Camber Angle

For a tyre to provide maximum traction it needs to be perpendicular to the road surface. When the tyre is perpendicular it is considered to have a zero camber angle, a positive camber is when the top of the tyre leans outward, and conversely a negative camber is when the top of the tyre tilts inward. Camber tilt is measured in degrees, and the three possible settings can be seen in Figure 2-17.

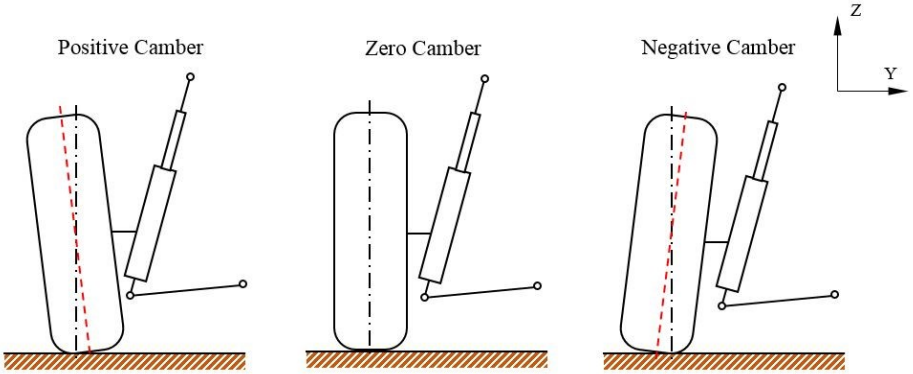

Figure 2-17. Camber Settings.

As a vehicle corners the camber of the outer wheel gains negative camber due to body roll. The degree of change is affected by suspension geometry factors such as roll centre height, swing arm and knuckle dimensions, and the length and position of the control arms. In order to compensate for the positive camber gain in cornering a negative camber can be set with the vehicle at rest. This will cause the outer tyres to be more perpendicular to the road in cornering, which results in greater traction which facilitates faster cornering (Puhn, 1976).

2.2.8 Body Torsional Stiffness

A vehicles torsional stiffness is its resistance to twisting about the longitudinal axis, which is experienced in cornering and single wheel loading scenarios. The calculations for determining lateral load transfer assume that the chassis is infinitely stiff, however if there is a large degree of twist there will be a variation in the distribution of mass between the front and rear tyres. This will impact the ability to predict the handling of the vehicle. A chassis stiffness should be high enough to consider the deflection negligible, as long as the performance of the vehicle is not hindered (Milliken & Milliken, 1995). The torsional stiffness can be calculated by fixing the rear suspension while loading the front suspension equally but in opposite directions, and then measuring the deflection angle, as seen in Figure 2-18.

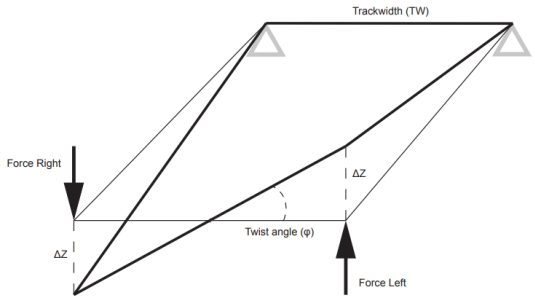

Figure 2-18. Torsional stiffness load case (Danielsson & Cocaña, 2015).

2.3 Composite Material Design

A composite material is a combination of two constituent materials, a matrix and a reinforcement, that forms a new material that has enhanced properties relative to the individual constituents (Barbero, 2010). The use of composites in industry has spread at a rapid rate, from military applications to consumer products, each utilising the benefits composites have to offer.

2.3.1 Reinforcement Material

Reinforcement materials can be split into the several categories, namely continuous fibres, discontinuous fibres, particles and whiskers. For the purpose of this review, only fibre reinforced composites were investigated, as particle and whisker reinforced composites are rarely used in

vehicle applications for structural components. A fibre is defined as a cylindrical material formation that has a high aspect ratio; that is, its length is much greater than its diameter, generally larger than a factor of 100 (Campbell, 2010). Continuous fibres in a continuous fibre reinforced composite run unbroken through the matrix material and are the primary load carriers along the load direction. Continuous fibres can be used in a uniaxial orientation, a multiaxial orientation or a random orientation in continuous mats. Discontinuous fibres are short fibres which can be randomly orientated or arranged preferentially in the direction of known loads. While there are many aspects to deciding which category and type of material to use in a design, cost plays a large role. Continuous fibre manufacture can be costly in both the manufacture of the fibres themselves and in the methods used to produce continuous fibre reinforced composite products. Discontinuous fibre reinforced composites are a less expensive alternative to continuous fibre reinforced composites, however, they offer reduced mechanical properties (Barbero, 2010).

2.3.1.1 Carbon Fibre Reinforced Polymer

Carbon fibre reinforced polymer (CFRP) is a composite comprising carbon strands as the reinforcement and polymer resin as the matrix. Carbon fibres comes in a variety of tensile strengths and tensile moduli. Fibre stiffness is controlled by the thermal treatment of the fibres in manufacture. Higher modulus fibres require higher heat treatment temperatures and therefore have a more costly manufacturing process. There are two types of fibres, pitch and polyacrylonitrile (PAN) fibre. Pitch fibres are weaker than PAN fibres, therefore PAN fibres dominate the market for high strength applications, such as the automotive industry for performance vehicles. Carbon fibres are brittle and have low shock resistance. Due to high cost in comparison to other lower strength fibre, carbon fibres are best used in weight critical applications or high performance applications (Barbero, 2010).

2.3.1.2 Glass Fibre Reinforced Polymer

Glass fibre reinforced polymer (GFRP) uses glass fibres derived from simultaneously extruding and cooling a molten mixture of silica and other chemicals through micro-fine bushings (Campbell, 2010). By altering the chemical composition of the mixture several grades of glass fibres can be produced, namely E-glass, C-glass and S-glass. E-glass is a widely-used grade of glass fibre due to good mechanical properties, chemical resistance and cost effectiveness. S-glass has the highest tensile strength and modulus, however, it is more expensive in comparison to E-glass. C-glass has a high resistance to chemical corrosion which makes it ideal for use in water and chemical tanks and pipes. Glass fibre can be obtained as continuous roving's, mats, yarn and, chopped strands.

2.3.1.3 Aramid Fibre

Aramid fibre is an organic compound that is used in various applications such as reinforced plastics, protective apparel, ropes, cables and tires. Due to exceptional toughness characteristics aramid fibre has a high damage tolerance and is used in ballistic protection in bulletproof vests, aircraft and tanks. Using aramid fibre in composite systems offers resistance to fatigue and stress rupture (US Department of Defense, 2002). Aramid fibres have a low compressive strength, are sensitive to ultraviolet light and the strength properties are temperature dependant (Barbero, 2010).

2.3.1.4 Fabric Weaves

Reinforcement material strands can be formed into unwoven or woven 2D textiles. Reinforcement material textiles have the potential to offer increased strength and performance while reducing the cost of manufacture. Usually woven fabrics are biaxial with the two fibre directions aligned orthogonal to each other. The primary direction is called the warp fibre and the secondary direction is called the fill or weft fibre. Fabrics can be uniaxial or multiaxial and can be selected based on how many reinforcement directions the design requires. Uniaxial woven fabrics offer strength in one direction, and are comprised of reinforcement fibres in the warp direction and a non-structural binder in the fill direction to hold the warp fibres together. Biaxial woven fabrics come in a variety of woven patterns, some of which are shown in Figure 2-19. Each woven pattern has different fabric properties which effect the strength of the fibres and the manufacturability of products using the fabric (Barbero, 2010). A table comparing pattern properties is shown in Table 2-2.

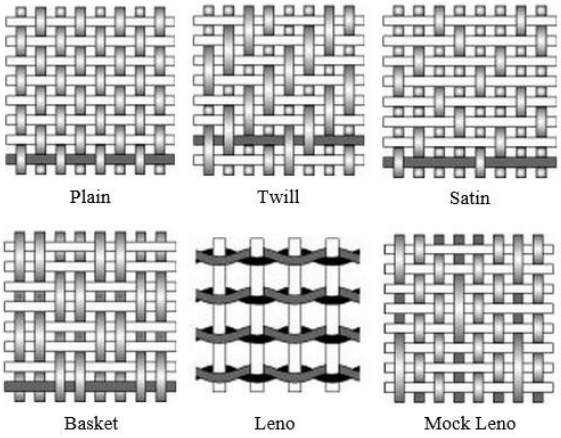

Figure 2-19. Bidirectional fabric weaves (NetComposites, n.d.).

Table 2-2. Bidirectional Weave Property Comparison (NetComposites, n.d.).

Property	Plain	Twill	Satin	Basket	Leno	Mock Leno
Good Stability	⋆⋆⋆⋆	⋆⋆⋆	⋆⋆	⋆⋆	⋆⋆⋆⋆⋆	⋆⋆⋆
Good Drape	⋆⋆	⋆⋆⋆⋆	⋆⋆⋆⋆⋆	⋆⋆⋆	⋆	⋆⋆
Low Porosity	⋆⋆⋆	⋆⋆⋆⋆	⋆⋆⋆⋆⋆	⋆⋆	⋆	⋆⋆⋆
Smoothness	⋆⋆	⋆⋆⋆	⋆⋆⋆⋆⋆	⋆⋆	⋆	⋆⋆
Balance	⋆⋆⋆⋆	⋆⋆⋆⋆	⋆⋆	⋆⋆⋆⋆	⋆⋆	⋆⋆⋆⋆
Symmetrical	⋆⋆⋆⋆⋆	⋆⋆⋆	⋆	⋆⋆⋆	⋆	⋆⋆⋆⋆
Low Crimp	⋆⋆	⋆⋆⋆	⋆⋆⋆⋆⋆	⋆⋆	⋆⋆/⋆⋆⋆⋆⋆	⋆⋆
⋆⋆⋆⋆⋆ = Excellent, ⋆⋆⋆⋆ = Good, ⋆⋆⋆ = Acceptable, ⋆⋆ = Poor, ⋆ = Very Poor						

Crimp in a fabric is a measure of undulation, or how frequently a fibre goes over and under orthogonal fibres. An increase in crimp results in a decrease in fabric mechanical strength. Drapability is the fabric's ability to conform to complex curvature. Fabric stability is the ability to maintain fibre orientation while being draped or during the manufacturing process. Selecting a fabric for a design is largely dependent on the application, and often there is a compromise. For example if one requires a high drapability one compromises the stability of the fabric, whereas more stable fabrics have higher crimp and are therefore mechanically weaker (ASM International, 2001).

Fabric weaves can be supplied pre-impregnated with activated resin (prepreg). The benefit of using prepreg fabrics over a wet lay-up process, where dry fabric is first laid-up in the mould and then infiltrated with resin, is that the optimal amount of resin has already been applied by the manufacturer. This avoids the possibility of over-saturating the fabric with resin, which would lead to a heavier component. It also allows for accurate thickness control. Disadvantages of using prepreg fabrics include a higher material cost and the requirement of higher curing temperatures. Prepreg fabrics need to be refrigerated in order to extend their shelf life, as the resin is already partially cured (Barbero, 2010).

2.3.2 Matrix Materials

The matrix material fulfils a number of roles. The matrix binds the fibres together and transfers loads between fibres. Without the matrix material fibres would not be able to transmit compressive loads. The matrix material carries some of the loads experienced by the composite, particularly via transverse stress, interlaminar shear stresses and bearing stresses. Service properties such as acceptable temperature range, chemical resistance, abrasion resistance and resistance to moisture and fluids are matrix dependent. The surface finish of the cured composite is also heavily affected by the matrix. Selecting a matrix material is critical in that it limits the manufacturing processes and techniques available to the designer. Therefore selecting a material that fits within anticipated design limitations and constraints is best done at the beginning of the design phase. Matrix materials can be polymers, metals or ceramics. Polymers are the most

common due to low cost and the ease of manufacturing high complexity parts and will be focused upon in this review. Polymer matrices can come in the form of either thermosetting or thermoplastic resins (Mallick, 2007).

2.3.2.1 Thermoset Matrix Materials

During the curing of a thermoset matrix the resin system undergoes an irreversible chemical transformation forming a cross-linked polymer. Thermoset matrices are the most popular type of polymer matrices since they are available in a large range of properties, have high processing speeds and achieve high fibre impregnation due to the fact that they typically possess a low viscosity. Thermoset resins have a limited handling time, referred to as pot life, before they become too viscose to use. Pot life and curing time varies for each resin system depending on the catalyst used and the chemical composition of the resin. Furthermore the curing reaction can either be exothermic or endothermic. During curing thermoset resin shrinks volumetrically and considering that reinforcement materials exhibit negligible shrinkage, this phenomenon can cause internal stresses if not taken into account (Barbero, 2010). Table 2-3 shows a comparison of characteristics for some common thermoset polymers.

Table 2-3. Polymer Matrix Properties (Barbero, 2010; Campbell, 2010).

Type	Characteristics
Polyester Resin	-Have a high performance-to-cost ratio making them popular -Medium mechanical strength -Fillers may be added to achieve favourable properties
Vinyl Ester Resin	-Higher elongation and corrosion properties than polyester -Highly resistant to acids, alkalis, solvents and peroxides -Costs are between polyesters and epoxies
Epoxy Resin	-Versatile in processing -High mechanical properties -High corrosion resistance -Less shrinkage than other thermosets -Electrically insulative -More expensive than polyesters and vinyl esters
Phenolic Resin	-Have low flammability and smoke production making them attractive for use in aircraft and vehicle interior panels -Have a good dimensional stability under temperature fluctuations -Have good adhesive properties -Brittle -Large shrinkage -Difficult to process

2.3.2.2 Thermoplastic Matrix

During processing a thermoplastic polymer does not undergo a chemical transformation and does not form cross linked bonds. A thermoplastic is softened in order to be processed then hardens back to a solid after processing is complete. Thermoplastics are harder to process than thermosets due to a higher viscosity. The high viscosity hinders impregnation of the resin into the reinforcement fibres. Damage to a thermoplastic can be repaired since the polymer bonds are

reversible by applying heat. Due to the difficulties in manufacture which lead to a higher manufacturing cost, thermoplastic types were not explored for the use in the Mamba EV.

2.3.3 Sandwich Laminates

A method of increasing the bending stiffness of a laminate without greatly increasing its mass is to introduce a lightweight core between fibre layers, forming a sandwich structure. The benefit of the increased bending stiffness needs to be weighed up against the increased difficulty and complexity of forming the sandwich laminate, as well as the increased manufacturing costs. Several part quality considerations must be taken into account when selecting the skin fabric, core and adhesive to use, such as, the surface and skin quality, the adhesive bond and core strengths, and the resistance to moisture absorption (US Department of Defense, 2002).

There are several types of core materials to select from, namely metallic and non-metallic honeycomb structures, as well as various foams. Table 2-4 highlights characteristics of some commonly used honeycomb materials, while Table 2-5 highlights characteristics of some commonly used foam cores materials.

Table 2-4. Honeycomb core characteristics (U.S. Department of Transportation, 2012).

Type of Honeycomb	Characteristics
Thermoplastics	-Good insulating properties -Good energy absorption -Relatively low cost
Aluminium	-Best strength-to-weight ratio -Best energy absorption -Good heat transfer -Relatively low cost
Steel	-Good heat transfer -Electromagnetically shielded -Heat resistant
Aramid	-Flame resistant -Fire retardant -Good insulating properties -Good formability
Glass Fibre	-Good insulating properties -Good formability
Carbon Fibre	-Good dimensional stability -High stiffness -Expensive
Ceramics	-Heat resistant to high temperatures -Good insulating properties -Expensive

Table 2-5. Foam core characteristics (Campbell, 2010; U.S. Department of Transportation, 2012).

Type of Foam	Characteristics
Polystyrene	-Low mechanical strength -Low cost -Easy to form -Resistant to water penetration
Phenolic	-Fire resistant -Low mechanical strength
Polyurethane	-Inexpensive -Medium mechanical strength -Surface bonds tend to deteriorate with age leading to delamination
Polyvinyl Chloride	-High compression strength -Excellent fire resistance -Durable
Polymethacrylimide	-Excellent mechanical strength -High dimensional stability under heat -Good solvent resistance -Resistant to creep compression -Most expensive foam core

2.3.4 Hardpoints

A popular method of joint two or more structures is to uses fasteners, which in composite component design can become an issue. For composite sandwich laminates that incorporate core materials to increase stiffness, bolted joints apply a high localised stress which can crush the core, resulting in a damaged laminate and an ineffective joint. In order to used bolted joints materials with a higher compressive strength are added to the localise region within the core material, replacing the low density core. These regions of mechanically stronger but denser materials are termed hardpoints.

2.3.5 Forming Methods

CFRP components can be manufactured using several methods, such as vacuum bagging (in and out of an autoclave), vacuum infusion, bladder or foam core moulding, and using a resin transfer moulding (RTM) press.

Vacuum bagging is a relatively inexpensive method of manufacturing components. It can be used in conjunction with various different mould materials and does not require highly expensive equipment. A mould is coated with a release agent to allow the component to be separated from the mould surface. The fabric, either prepreg or dry, is then placed into the mould. If dry fabric is used the resin is then applied. The fabric is covered in a release film, with a breather fabric on top of that. Finally a bagging film is placed over the mould and edges sealed with a sealant tape, or the mould is placed inside a bagging film envelope. A vacuum pump then removes the air within the bag causing the atmosphere to apply a pressure evenly over the component (US Department of Defense, 2002). Figure 2-20 shows a diagram of the vacuum bagging layers.

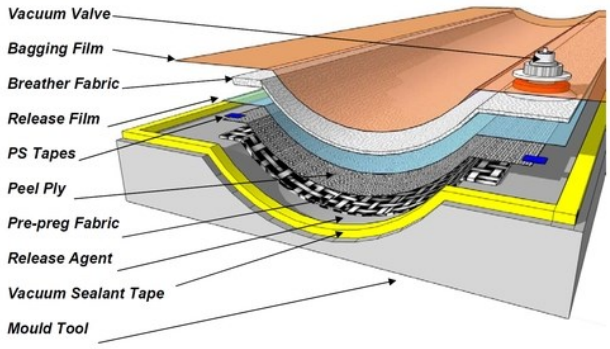

Figure 2-20. Vacuum bagging diagram (Multitex Composites, n.d.).

Resin infusion moulding is a variation of vacuum bagging, where the vacuum draws the resin into the component, post-bagging, instead of impregnation occurring during the lay-up process. The mould is coated with a release agent, and a dry fabric is then placed into the mould with a peel ply on top. Instead of a breathing fabric, a resin flow medium is placed on top of the peel ply. This allows for the resin to be drawn across the component. The flow medium is either removed after the forming process or in some cases it becomes part of the component. The last layer is the vacuum bag. As a vacuum is applied to the component, the decreasing pressure draws the resin through the flow medium, wetting the fabric. A diagram depicting resin infusion moulding is shown in Figure 2-21.

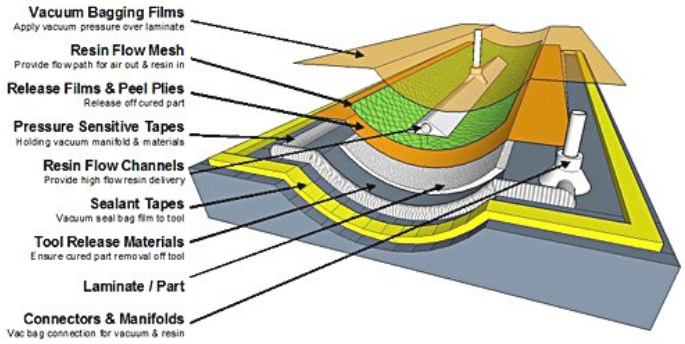

Figure 2-21. Resin infusion moulding diagram (AlexPB, n.d.).

RTM press moulding uses a hydraulic press to form composites. The fabric is preformed and placed within the mould beneath the press and a vacuum is applied. The resin is drawn through the component, which is then cured under high compressive loading. The advantages of this process are that there is a low tolerance in part thickness and short cycle time (Graf et al., n.d.). Figure 2-22 describes the RTM press process.

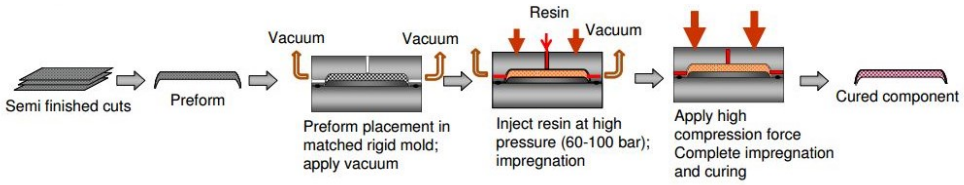

Figure 2-22. RTM process diagram (Graf et al., n.d.).

2.4 Finite Element Method

The finite element method (FEM) is a numerical method for approximating solutions to problems that are too complex to solve with analytical methods. Typical problems solved with this approach include structural, thermal, mass flow, and fluid flow problems. Modern structural analysis using FEM is done using computational software. In order to approximate a continuous solution over a complex geometry the geometry needs to be 'broken' into smaller, simpler, regions, after which a discrete approximated solution is then solved for. The FEM discretises the body being modelled, dividing it up into an equivalent system of smaller bodies interconnected at points (nodes), boundary lines, and/or surfaces. These bodies are termed finite elements. Element can be 1D, 2D or 3D, as well as first or second order. First order elements have nodal points at the corners of the element, and use a linear shape function to interpolate results between nodal points. Second order elements use quadratic shape functions to interpolate results between the corner nodes, and therefore utilises a midpoint node between the corner nodes. Second order elements generally result in a more accurate solution, however they are more computationally expensive due to the extra nodal points.

Each nodal point is associated with a set of governing equations which are used to solve an unknown quantity. The values calculated at nodal points are interpolated to approximate the values within the element and along boundaries, resulting in an approximate solution for the entire body. Each of the nodal points have six degrees of freedom (DOF), three translational and three rotational.

There are two primary methods for structural analysis, the force or flexibility method and the stiffness or displacement method. The force method uses internal forces as the unknown parameter and aims at determining the response of a statically indeterminate structure to applied loads or deformations. The stiffness method uses displacement as the unknown parameter. Since the stiffness method was simpler to implement computationally most finite element software packages incorporate it as the method for solving structural problems (Logan, 2011). Since Siemens NX incorporates the stiffness method it will be explored further.

For the stiffness method force-displacement relations are determined, after which equations are developed which satisfy the equilibrium conditions of the structure. Each element has a stiffness [k] that relates nodal forces $\{f\}$ to nodal displacement $\{\delta\}$,

$$\{\delta\} = [k]^{-1}\{\mathrm{f}\} \tag{2.10}$$

which for the entire system results in the global equation,

$$\{\delta\} = [K]^{-1}\{F\} \tag{2.11}$$

Where [K] is the global stiffness matrix and $\{F\}$ is a vector containing the global forces acting on the whole body. Using known forces and boundary conditions, such that the equilibrium conditions are satisfied, the displacements can then be calculated. Stresses and strains can then be calculated using the constitutive and compatibility equations (Logan, 2011).

2.4.1 Governing Equations

In structural analysis one aims at determining the resulting response of a physical structure to a defined input, solving principally for displacement, and secondarily for stress and strain. There are three fundamental equations which govern the response of an elastic, homogeneous material, the equilibrium, compatibility, and constitutive equations (Barbero, 2013).

The three equilibrium equations are,

$$\begin{aligned} \frac{\partial \sigma_{xx}}{\partial x} + \frac{\partial \sigma_{xy}}{\partial y} + \frac{\partial \sigma_{xz}}{\partial z} + f_x = 0 \\ \frac{\partial \sigma_{xy}}{\partial x} + \frac{\partial \sigma_{yy}}{\partial y} + \frac{\partial \sigma_{yz}}{\partial z} + f_y = 0 \\ \frac{\partial \sigma_{xz}}{\partial x} + \frac{\partial \sigma_{yz}}{\partial y} + \frac{\partial \sigma_{zz}}{\partial z} + f_z = 0 \end{aligned} \tag{2.12}$$

The compatibility equation for small deflections, which aims at determining the material strains, ε_{ij}, using the displacement of the body, u_i, is represented by, with $i, j = 1,2,3$,

$$\varepsilon = \varepsilon_{ij} = \frac{1}{2}\left(u_{i,j} + u_{j,i}\right) \tag{2.13}$$

which expands to,

$$\begin{aligned}
\varepsilon_{11} &= \frac{\partial u_1}{\partial x_1} = \epsilon_1; & 2\varepsilon_{12} = 2\varepsilon_{21} &= \left(\frac{\partial u_1}{\partial x_2} + \frac{\partial u_2}{\partial x_1}\right) = \gamma_6 = \epsilon_6 \\
\varepsilon_{22} &= \frac{\partial u_2}{\partial x_2} = \epsilon_2; & 2\varepsilon_{13} = 2\varepsilon_{31} &= \left(\frac{\partial u_1}{\partial x_3} + \frac{\partial u_3}{\partial x_1}\right) = \gamma_5 = \epsilon_5 \\
\varepsilon_{33} &= \frac{\partial u_3}{\partial x_3} = \epsilon_3; & 2\varepsilon_{23} = 2\varepsilon_{32} &= \left(\frac{\partial u_2}{\partial x_3} + \frac{\partial u_3}{\partial x_2}\right) = \gamma_4 = \epsilon_4
\end{aligned} \tag{2.14}$$

The constitutive equation aims at determining the stresses induced in a body using the stiffness matrix, $[C]$, and material strain. This equation is represented by,

$$\{\sigma\} = [C]\{\varepsilon\} \tag{2.15}$$

The compliance matrix, $[S]$, is the inverse of the stiffness matrix, therefore equation (2.15) can be written in terms of the compliance matrix,

$$\{\varepsilon\} = [S]\{\sigma\} \tag{2.16}$$

For a three dimensional orthotropic material,

$$[S] = \begin{bmatrix}
\frac{1}{E_1} & \frac{-\nu_{21}}{E_2} & \frac{-\nu_{31}}{E_3} & 0 & 0 & 0 \\
\frac{-\nu_{12}}{E_1} & \frac{1}{E_2} & \frac{-\nu_{32}}{E_3} & 0 & 0 & 0 \\
\frac{-\nu_{13}}{E_1} & \frac{-\nu_{23}}{E_2} & \frac{1}{E_3} & 0 & 0 & 0 \\
0 & 0 & 0 & \frac{1}{G_{23}} & 0 & 0 \\
0 & 0 & 0 & 0 & \frac{1}{G_{13}} & 0 \\
0 & 0 & 0 & 0 & 0 & \frac{1}{G_{12}}
\end{bmatrix} \tag{2.17}$$

For plane stress the constitutive equation can be reduced, since $\sigma_3 = 0$, with two sets of equations being used to determine in-plane stresses and transverse stresses. Using the reduced compliance matrix the equation for in-plane stress-strain relationship is shown to be,

$$\begin{Bmatrix} \epsilon_1 \\ \epsilon_2 \\ \gamma_6 \end{Bmatrix} = \begin{bmatrix}
\frac{1}{E_1} & \frac{-\nu_{21}}{E_2} & 0 \\
\frac{-\nu_{12}}{E_1} & \frac{1}{E_2} & 0 \\
0 & 0 & \frac{1}{G_{12}}
\end{bmatrix} \begin{Bmatrix} \sigma_1 \\ \sigma_2 \\ \sigma_6 \end{Bmatrix} \tag{2.18}$$

and for the transverse stress-strain relationship,

$$\begin{Bmatrix} \gamma_4 \\ \gamma_5 \end{Bmatrix} = \begin{bmatrix} \frac{1}{G_{23}} & 0 \\ 0 & \frac{1}{G_{13}} \end{bmatrix} \begin{Bmatrix} \sigma_4 \\ \sigma_5 \end{Bmatrix} \tag{2.19}$$

2.4.2 Siemens NX Analysis Workflow

In order to run various computational analyses within Siemens NX, users follow a defined design process utilising a linked file structure. The file structure allows the user to make changes at any point along the analysis process, updating the subsequent files based on the new user inputs. For structural analysis, the applicable file workflow comprises three steps. Firstly, the user generates the model geometry in a part file, then meshes the geometry in a .fem file, adding material properties, and then finally defines boundary conditions and global loads in the .sim file, which then permits the solution of the problem via the appropriate solver.

2.4.3 Material Properties

In Siemens NX, the geometry needs to be assigned a material in order to define directionality and stress-strain behaviour. In terms of directionality, a material can be defined as isotropic, orthotropic, or anisotropic. Isotropic materials have uniform properties in all directions, orthotropic materials have three planes of symmetry, and anisotropic materials have no planes of symmetry. Within NX, separate composite plies can be defined as either isotropic or orthotropic, with nine elastic constants being required to define a 3D orthotropic material: E_1, E_2, E_3, ν_{12}, ν_{13}, ν_{23}, G_{12}, G_{13}, and G_{23}. For a 2D orthotropic material, only three elastic constants are required: E_1, E_2, and ν_{12} (Siemens PLM Software, 2013).

Isotropic materials can be defined with only two of the three elastic constants. The third property can be calculated according to the relationship:

$$E = 2G(1 + \nu) \tag{2.20}$$

A composite ply's material properties can also be defined based on its constituents. The constituent materials are defined as isotropic and the user defines the warp and weft fibres, matrix, volume fractions, and final ply thickness.

2.4.4 Zone-based vs Ply-based Modelling

Composite materials modelling in Siemens NX can employ either a zone based or ply based approach. The general process followed for each approach is shown in Figure 2-23. The primary difference between the two approaches is that in zone based modelling, the plies are projected onto the surfaces with the fibre orientation following the element material orientation, whereas in the ply based approach, draping of plies can be simulated allowing one to predict areas of high fibre distortion and insert cut lines to relieve distortions. Of the two modelling methods, the ply based approach more closely simulates the manufacturing process, resulting in a more accurate model. In addition, it aids in defining the manufacturing process in terms of weave patterns and cut lines for complex curves. However this approach is more time consuming since each ply requires draping. The zone based approach is a less time-consuming method for designs with lower ply lay-up variation and can be used for preliminary designs or prototyping, before the subsequent application of a ply based approach. However in developing a preliminary design, depending on the geometry and the variation in ply lay-up, the use of a ply based approach with a projection drape setting may be more time-effective than using the zone based approach (Siemens PLM Software, 2013).

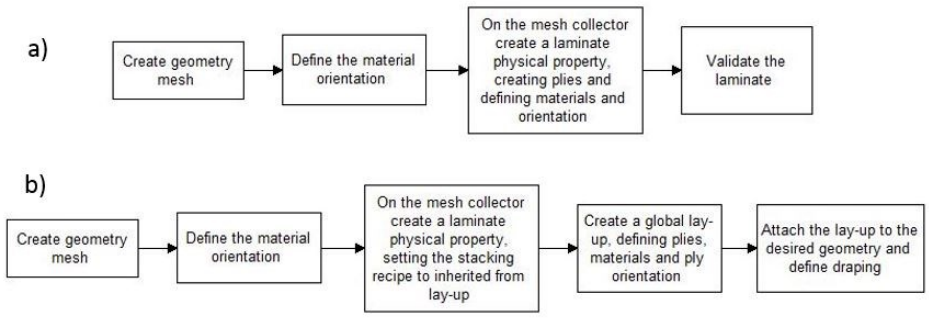

Figure 2-23. Composite modelling process in NX: a) zone base, b) ply-based (Siemens PLM Software, 2013).

2.5 Composite Failure Analysis

A laminate is considered to have failed when it is unable to fulfil its intended function. There are a large variety of failure modes for composite plies, such as fibre failure, matrix crazing and cracking, debonding along the fibre-matrix interface, and delamination (Barbero, 2013). Failure theories have been developed using micromechanical and macromechanical models, with the aim of predicting the failure of composite materials in advance of component production.

2.5.1 Failure Theories

With the chassis design and analysis being undertaken in Siemens NX, only the criteria that are valid for a 2D composite analysis using a carbon weave were explored. Table 2-6 shows the

failure theories allowed in a Siemens NX simulation, and under which conditions they are applicable (Siemens PLM Software, 2013).

Table 2-6. Allowable failure theories in Siemens NX for a zone-based FEM.

Failure Theory	Valid for:
Maximum Stress	2D & 3D composites
Maximum Strain	2D & 3D composites
Hill	2D & 3D composites
Hoffman	2D & 3D composites
Tsai-Wu	2D & 3D composites
Puck	Unidirectional fibres
LaRC02	Unidirectional fibres
Von Mises Yield	Isotropic materials
Von Mises Ultimate	Isotropic materials

Of the allowable failure theories, the maximum stress, maximum strain, Hill, Hoffman, and Tsai-Wu theories are applicable for 2D composite analyses. These theories can be further split into two groups: limit failure theories, and interactive failure theories.

2.5.1.1 Limit Failure Theories

Limit failure theories relate the experienced stresses and strains to the strength properties of the materials, and consider the different modes of failure of the constituents in a composite due to its heterogeneous nature (Camanho, 2002).

Maximum Stress Theory

The maximum stress failure theory predicts failure if any stress exceeds the corresponding experimentally-derived failure stress. Failure is predicted if the failure index, I_f, exceeds 1, (Siemens PLM Software, 2013)

$$I_f = max \begin{cases} {\sigma_1}/{F_{1t}} \; if \;\; \sigma_1 > 0 \\ {|\sigma_1|}/{F_{1c}} \; if \;\; \sigma_1 < 0 \\ {\sigma_2}/{F_{2t}} \; if \;\; \sigma_2 > 0 \\ {|\sigma_2|}/{F_{2c}} \; if \;\; \sigma_2 < 0 \\ {|\sigma_4|}/{F_4} \end{cases} \tag{2.21}$$

Maximum Strain Theory

The maximum stress failure theory predicts failure if any strain exceeds the corresponding experimentally-derived failure strain. Failure is predicted if the failure index, I_f, exceeds 1, (Siemens PLM Software, 2013)

$$I_f = max \begin{cases} \epsilon_1/\epsilon_{1t} \ if \ \epsilon_1 > 0 \\ |\epsilon_1|/\epsilon_{1c} \ if \ \epsilon_1 < 0 \\ \epsilon_2/\epsilon_{2t} \ if \ \epsilon_2 > 0 \\ |\epsilon_2|/\epsilon_{2c} \ if \ \epsilon_2 < 0 \\ |\epsilon_4|/\epsilon_4 \end{cases} \quad (2.22)$$

2.5.1.2 Interactive Failure Theories

Interactive failure theories consider the interaction between stress or strain components, and can be classified by three types based on their formulation: polynomial, direct mode determining, and strain energy theories. The following three failure theories are all polynomial theories:

Hill

For the Hill failure theory failure is predicted if the failure index, I_f, exceeds 1. I_f is calculated by (Siemens PLM Software, 2013),

$$I_f = \left(\frac{\sigma_1}{A}\right)^2 - \frac{\sigma_1\sigma_2}{(A)^2} + \left(\frac{\sigma_2}{B}\right)^2 + \left(\frac{\sigma_4}{F_4}\right)^2 \quad (2.23)$$

where,

$$A = F_{1t} \ if \ \sigma_1 > 0, or \ A = F_{1c} \ if \ \sigma_1 < 0 \quad (2.24)$$
$$B = F_{2t} \ if \ \sigma_2 > 0, or \ B = F_{2c} \ if \ \sigma_2 < 0 \quad (2.25)$$

Hoffman

For the Hill failure theory failure is predicted if the failure index, I_f, exceeds 1. I_f is calculated by (Siemens PLM Software, 2013),

$$I_f = \frac{{\sigma_1}^2}{F_{1t}F_{1c}} - \frac{\sigma_1\sigma_2}{F_{1t}F_{1c}} + \frac{{\sigma_2}^2}{F_{2t}F_{2c}} - \frac{(F_{1t} - F_{1c})}{F_{1t}F_{1c}}\sigma_1 - \frac{(F_{2t} - F_{2c})}{F_{2t}F_{2c}}\sigma_2 - \left(\frac{\sigma_4}{F_4}\right)^2 \quad (2.26)$$

Tsai-Wu

For the Tsai-Wu failure theory failure is predicted if the failure index, I_f, exceeds 1. I_f is calculated by (Siemens PLM Software, 2013)

$$I_f = F_1\sigma_1 + F_{11}{\sigma_1}^2 + F_2\sigma_2 + F_{22}{\sigma_2}^2 + 2F_{12}\sigma_1\sigma_2 + F_{66}\sigma_4 \tag{2.27}$$

where,

$$\begin{aligned} F_1 &= \frac{1}{F_{1t}} - \frac{1}{F_{1c}} \\ F_{11} &= \frac{1}{F_{1t}F_{1c}} \\ F_2 &= \frac{1}{F_{2t}} - \frac{1}{F_{2c}} \\ F_{22} &= \frac{1}{F_{2t}F_{2c}} \\ F_{66} &= \frac{1}{{F_4}^2} \end{aligned} \tag{2.28}$$

F_{12} is a strength interaction term which requires a biaxial test. However, due to testing difficulties, the following range for F_{12} has been recommended:

$$-\frac{1}{2}\sqrt{\frac{1}{F_{1t}F_{1c}F_{2t}F_{2c}}} \leq F_{12} \leq 0 \tag{2.29}$$

If an experimental value cannot be obtained the lower limit is frequently used (Mallick, 2007).

2.5.1.3 Ply Failure

In composite component design, failure can be defined by either first ply failure (FPF) or last ply failure (LPF). FPF assumes that once the first ply in the laminate fails, the entire laminate fails; resulting in a more conservative design. LPF analysis uses FPF methods to determine when a ply fails, then degrades the stiffness of the failed region, reiterating the solution using the updated stiffness matrix. Failure is then defined as when the final ply in the laminate fails. This results in a more accurate prediction of failure within a composite model. However degradation of the element stiffness needs to account for the mode of failure, resulting in a more complex and time-consuming analysis (Barbero, 2010).

CHAPTER 3

Methodology

For the development of a chassis for the Mamba EV a spatial analysis first needed to be done to ensure the chassis could incorporate the required components of the vehicle. Placement of the components indicated spatial design constraints, regions of higher loads within the chassis, as well as regions that would require mounting points. This analysis also aided in defining the desired overall dimensions of the vehicle, such as track and wheelbase. A basic internal structure was then be developed to allow for component mounting, driver safety, and ease of manufacture. Once the initial internal structure was developed, it was then mated with the initial outer body, which together eventually formed the geometric model of the monocoque.

The model of the chassis was then discretised, dividing the surfaces into a series of mesh collectors, with the meshed surface edges being stitched to ensure mesh continuity. In order to ensure that loads would be transmitted through the suspension arms into the chassis structure the one-dimensional representation of the suspension system was connected to the two-dimensional mounting brackets using point-to-edge connection elements. Once the structure had a continuous mesh, material properties were applied to all the collectors. Assumed composite stacking recipes were initially applied to create a starting point for the iterative analysis process.

Siemens NX utilises the stiffness finite element method for analysing static structures, which requires boundary conditions to be applied to ensure that the system is non-singular. Once the chassis was correctly constrained, load cases were applied to represent the worst case loading the chassis would experience under normal urban driving conditions. Simulations were run in order to monitor the response of the chassis structure under the various load cases. Four parameters were monitored, structure deflection, element stresses, the ply failure index, and the bond failure index. The results from load case simulations were used to refine the design of the geometry as well as the composite lay-up. The simulations were then iteratively re-run with the refined geometry and composite lay-up, and once the peak values of the monitored parameters were within an acceptable range, structural survivability was predicted, and the design was considered ready for prototype manufacture. Figure 3-1 shows the process followed in the development of the chassis design for the Mamba EV.

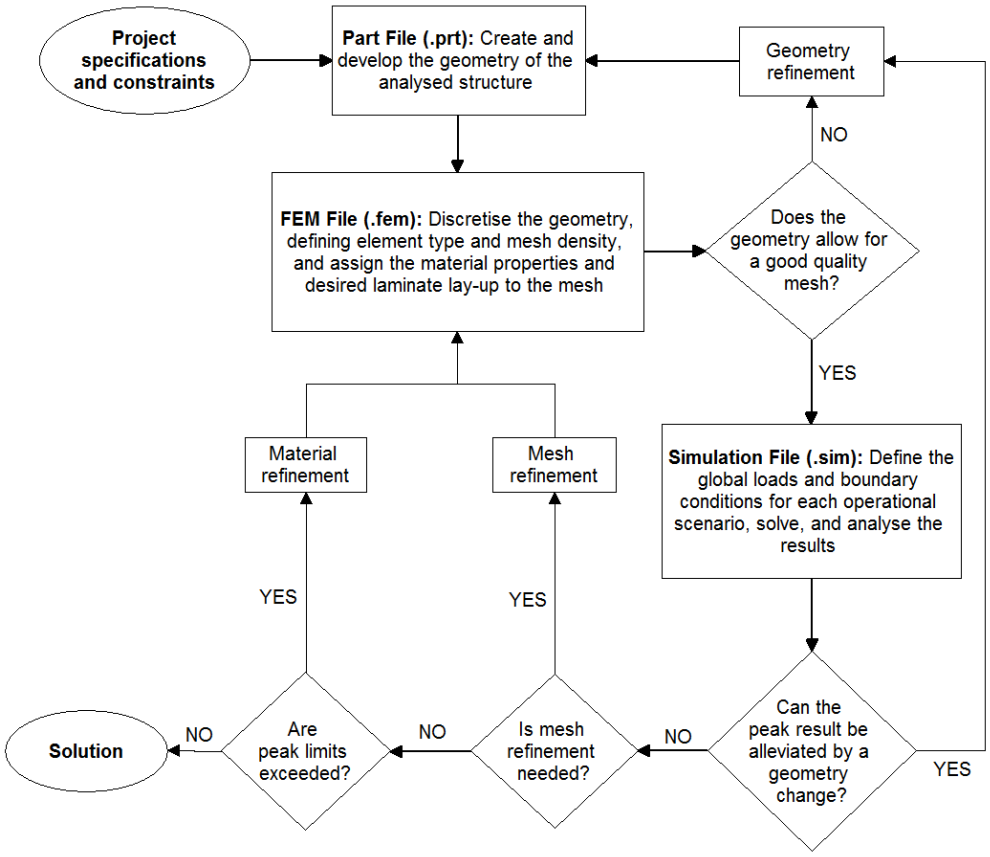

Figure 3-1. Flow diagram describing the Mamba EV chassis design development process.

CHAPTER 4

Chassis Design

This chapter details the development of the Mamba EV chassis geometry which comprises principally of two-dimensional flat plate panels bonded together to form the three-dimensional box-chassis structure. The influences of sub-components on the design, spatial constraints, and vehicle handling characteristics that influenced the design configuration are also discussed.

4.1 Initial Specifications

At the start of the Mamba EV project, the project team had to define the type of vehicle to design, as well as the desired performance specifications. Seed funding was secured for manufacture of the prototype, however a time constraint was imposed by the funders, which resulted in the team needing to make various decisions to constrain the design and allow progress to be made at a more rapid pace. This included the purchase of particular components, as well as basing initial dimensions on existing vehicles of a similar performance class and size. The team had one year to complete the design and produce the finished prototype vehicle.

A two seater "urban sports car" was the design aim, with an emphasis on acceleration rather than top speed performance. The defining outer dimensions of the vehicle, including the track, wheel base, ride height and roof height, were based on the Lotus Elise (Lotus Cars Ltd, 1996). This gave a starting point for the chassis design process, from which the dimensions were adjusted based on the spatial requirements of selected components and ergonomics.

4.2 Spatial Design

Since the function of a chassis is to house all components required for a vehicle to operate, while retaining structural integrity and required stiffness under all expected driving conditions, a spatial analysis was first required to ensure the components could be suitably incorporated. Components were represented either by detailed computer aided design models or simply as volume blocks. These representations were placed within the boundaries of the wheel base and track, and where necessary, the dimensions were adjusted to ensure the selected components could be mounted and would act as intended. Component placement was also dictated by ease of assembly and mass distribution, while maintaining accessibility for maintenance. The spatial model can be seen in Figure 4-1.

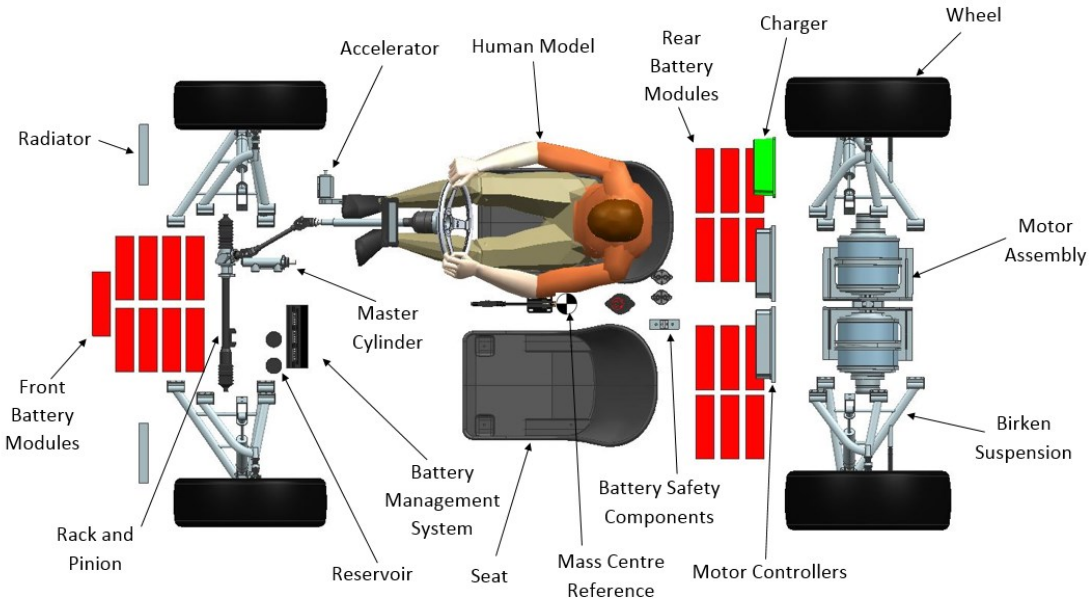

Figure 4-1. Spatial layout of major EV components.

4.2.1 Drivetrain

For the Mamba EV, two options were discussed for potential drivetrain configurations: either a single motor with a differential, or a split rear axle with either two motors or a dual shaft motor. Based on the available motors that fitted the required output parameters, a split axle rear wheel drive system (with "electric diff") was decided upon, this resulted in a more compact, light-weight configuration. The motors chosen for the Mamba EV were EnerTrac Dual 603 (Enertrac Corporation, n.d.), which are liquid-cooled BLDC motors providing 60 kW each of peak power.

CAD models for the Dual 603 motor, Figure 4-2(a), were provided by the manufacturer and subsequently imported into Siemens NX. Since the motors were a derivative of motors designed as hub motors for motorbike electric conversions, the outer housing forms the rotor while the fixed inner stator is constrained to the chassis via a circular array of mounting bolt holes.

The mounting brackets for the motors were designed by a Mamba EV project member (Sim, Woods, Mons, & Chetty, 2016). The mounts needed to withstand the loads generated by the motor as well as allow for access to the cooling ports, to which the coolant tubes would connect. The two motors and their mounts needed to fit between the rear suspension mounting panels, which influenced the track dimensions. Figure 4-2(b) shows the complete motor assembly without the connected cooling system.

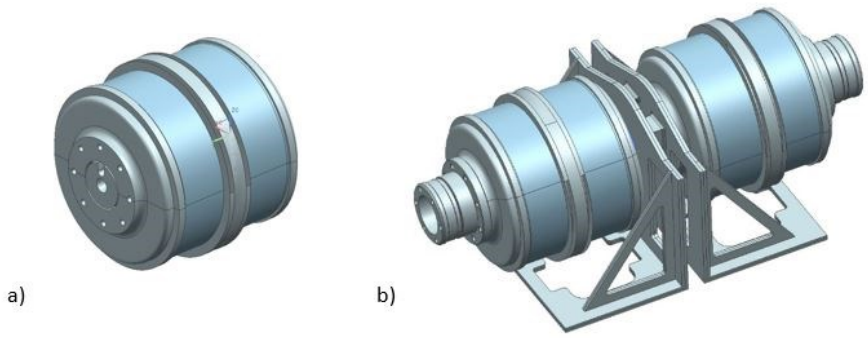

Figure 4-2. a) EnerTrac Dual 603, b) Mamba EV motor assembly.

Separate motor controllers were used to control motor operation and needed to be accommodated by the chassis. Four Kelly KLS12601-8080IPS motor controllers were selected for this purpose, based on cost and compatibility with the EnerTrac motors. A controller was required for each of the stators. Based on the layout of the electrical system, it was decided to mount the controllers on the rear firewall, which allowed for an easier wiring connection between the batteries, controllers, and motors. A CAD model of each controller was generated using the datasheet provided by the manufacturer. The controllers were each fitted with a heatsink mounted to the aluminium base plate, which required air flow for cooling. The heatsinks were mounted through the firewall, allowing a cooling air channel to be created in the rear firewall, adjacent to the motor assembly.

4.2.2 Suspension

The function of a vehicle's suspension system is to flexibly link the body to the wheels which improves vehicle handling over uneven surfaces by keeping the tires in contact with the driving surface, and to dampen road vibration and noise, which increases occupant comfort.

Two primary suspension types were considered for use in the Mamba EV, a double wishbone system and a MacPherson strut system. It was ultimately decided to implement a double wishbone suspension, since the double wishbone suspension offers better handling characteristics and allows the ride height to be lower, resulting in a lower centre of mass.

Due to time constraints and the complex nature of designing a suspension system, it was decided that for the initial prototype, a suspension system would be purchased rather than being custom developed. The chosen suspension system would have to have been designed for a vehicle of a similar weight and class of performance. Purchasing a suspension system reduced the development time of the vehicle, however, the trade-off was a reduced ability to adjust handling parameters.

A complete suspension system was purchased from Birken Performance Cars, which included disc brakes and callipers. Spatially, the system limited the rear track width of the vehicle, since it was designed for use on a Birken Lotus 7, which uses a longer A-arm due to its outrigger configuration. The Birken suspension was re-modelled in Siemens NX, as seen in Figure 4-3, to add to the spatial model, and to aid in setting the suspension positioning and mount angle.

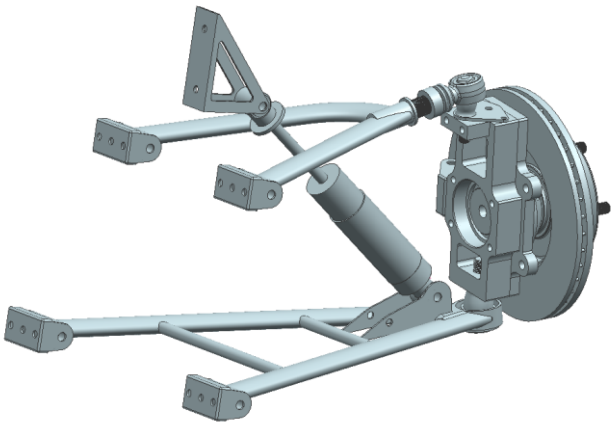

Figure 4-3. Birken front right double wishbone suspension.

4.2.3 Battery Pack

Since the battery pack for a light-weight EV generally accounts for a large percentage of vehicle mass, the placement of the pack modules is critical in respect of vehicle weight distribution.

With a focus on mass reduction, the cells used needed to have the highest energy density possible, while still being able to deliver the required power output. For this purpose, Panasonic NCR18650PF lithium ion battery cells were selected, since they were the most cost-effective cells that could meet the performance requirements. The final battery design incorporated 42 series packs, each with 48 cells in parallel.

Due to spatial constraints it was decided to split the battery into two sections, the first being positioned in the nose of the vehicle, while the second was positioned behind the occupants, as shown in Figure 4-1. This configuration allowed for easy assembly, was optimal in maintaining a 45/55 mass distribution, and did not constrict the wiring of the electrical system.

Besides the battery cells, the battery pack included a battery management system (BMS), safety components, such as a fuse and contactors, as well as a charger. Since the BMS needed to be wired to all the cells, a mid-point between the two mounting locations was optimal to avoid

excessively long wiring harnesses. It was decided to mount the BMS under the dashboard, while the charger was placed on the rear firewall, next to the motor controllers, as per Figure 4-1.

4.2.4 Steering and Driver Cabin

The spatial considerations for the steering system included rack and pinion mounting, steering column mounting, and seat mounting such that the driver would be able to reach the steering wheel comfortably. The rack and pinion, shown Figure 4-4, was mounted in the nose of the vehicle, in plane with the tie rod mounts for the front suspension, and was raised in order to allow for the front battery wiring. An AC Cobra steering column was used for the Mamba EV, and was obtained from TR Tec, an industrial partner in the project.

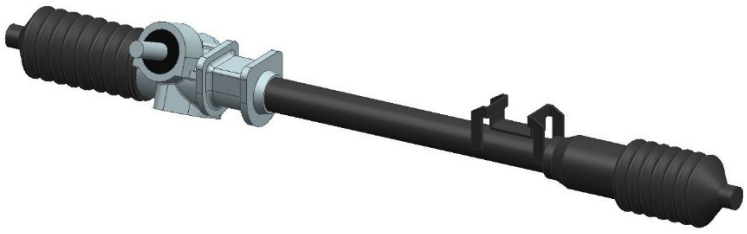

Figure 4-4. Ford escort MK1 rack and pinion.

In sports cars, the occupants typically sit lower to the base of the vehicle in order to reduce the height of the centre of gravity, and to reduce the overall height of the vehicle, which results in a lower frontal area and thus reduced aerodynamic drag. Human models were used in the design to aid in defining the angle of the steering column, the height of the dashboard, and the roof height. The dimensions of the human models in Siemens NX are based on either the U.S. Army Anthropometric Survey (U.S. Army Natick Soldier Research Development and Engineering Center, 2014) or National Health and Nutrition Examination Survey database (National Center for Health Statistics, 2018), and can be defined by a height percentile and gender. Three models were used, a 95th percentile male model, which defined the roof height, and two 50th percentile models, one male and one female, which were used as a check to see if the human models line of vision was above the dashboard, as demonstrated in Figure 4-5. Based on the height of the human models in Siemens NX, the steering column was mounted at 21° to the ground plane.

The positioning of the seat mounts, which were obtained from TR Tec, relative to the brake and accelerator pedals was determined by physically measuring team members seated in the Mamba EV seats. The longitudinal distance between the point that the test subject's heel touched the floor and their hip point was measured. Several people, varying in height, were measured and the seat

rails were positioned accordingly. The rails allowed the seat to be adjusted longitudinally over a range of 200 mm.

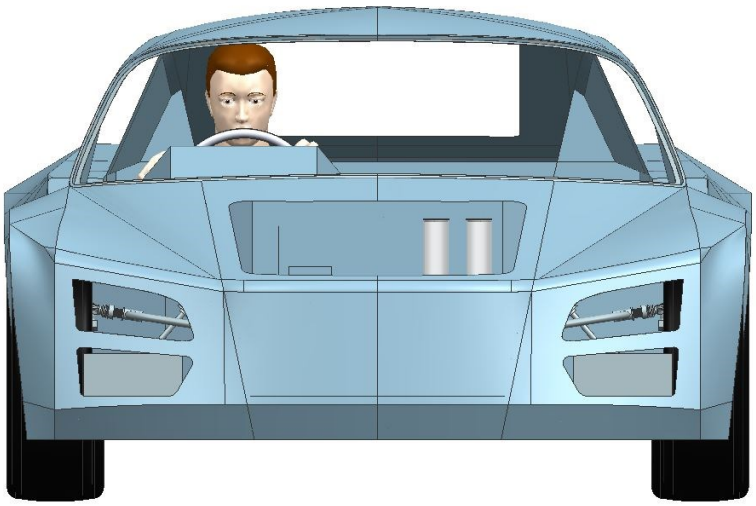

Figure 4-5. Front view of the Mamba EV occupied by a 50th percentile human model.

4.3 Vehicle Handling

The following section discusses the parameters and components that were considered to affect the handling characteristics of the Mamba EV.

4.3.1 Mass Distribution

The mass distribution of the EV was derived from the mass centres of all of its constituent components. The reference point used was 1160 mm from the front axle, laterally central, and 290 mm from the ground plane. Initially, a mass for the chassis was assumed, with the centre of mass being determined with an assumed constant panel thickness across all chassis surfaces. Using the data shown in Table 4-1, the overall mass centre and mass distribution were calculated.

Table 4-1. Component masses and positions.

Component	Mass [kg]	X Position [mm]	Y Position [mm]	Z Position [mm]
Accelerator	1	-995.84	217.42	107.01
Battery Pack Rear Left	31.2	663.79	-337	-50.46
Battery Pack Rear Right	31.2	663.79	337	-50.46
Battery 3 Pack Front	46.8	-1528.18	0	-50.46
BMS	2.43	-974.29	-124.46	294.93
Charger	6.35	797.9	519.93	275.03
Chassis	75	-406.27	-51.61	280.08
Controllers	27.88	802.51	-1.362	254.17
CV's	7	1190	0	19.9
Hand Brake	0.74	-204.19	0	-23.63
Headlights	2.32	-1630	0	160
Motors	97.91	1189.63	0	8.4
Passengers	170	-28.029	0	198.64
Pump	1.3	-1080	-182	-70
Radiator	3	-1560	0	-30
Reservoir	2	-1070	-185	222
Seats	14.54	20.58	0	-3.081
Steering Column	5.79	-562.38	304.2	338.65
Steering Rack	3.68	-1252.52	30.05	61.19
Suspension Assem. Front Left	16.27	-1160	-700	0
Suspension Assem. Front Right	16.27	-1160	700	0
Suspension Assem. Rear Left	16.02	1190	-690	-15
Suspension Assem. Rear Right	16.02	1190	690	-15
Wheel Front Left	14.22	-1160	-755	6.83
Wheel Front Right	14.22	-1160	755	6.83
Wheel Rear Left	18.62	1190	-747.5	19.9
Wheel Rear Right	18.62	1190	747.5	19.9
Windscreen	9.36	-767	0	617.1
Total	669.74			

The x-coordinate for the centre of mass was calculated using:

$$x = \frac{\sum_{i=1}^{n}(x_i m_i)}{\sum_{i=1}^{n}(m_i)} \tag{4.1}$$

where x_i is the longitudinal distance between the mass centre of each components and the reference point shown in Figure 4-1, and m_i is the mass of each component.

The y- and z-coordinates were calculated using the same equation, substituting x for the relevant coordinate. This resulted in a mass centre of CoM = CoG = (102.06, 0.86, 102.83), the position of which can be seen in Figure 4-6.

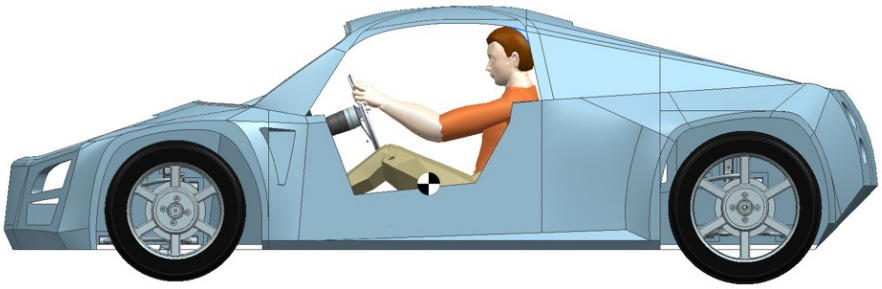

Figure 4-6. Centre of mass of the Mamba EV.

Using the centre of mass, which coincides with the centre of gravity, and equations (2.1) to (2.4), the static gravitational load on each of the wheels was calculated in both the longitudinal and lateral directions. The static loads are shown in Table 4-2.

Table 4-2. Static load on each wheel.

Wheel	Load [N]
Front left	1519.08
Front right	1522.51
Rear left	1762.27
Rear right	1766.19

4.3.2 Suspension Settings

Since the suspension system for the EV was purchased, there were limitations imposed that restricted which handling parameters could be adjusted. With the suspension having a fixed geometry, only the tyre dimensions and the mounting position of the arms required definition. The angle and position of the mounting points for the suspension arms significantly influence the caster and camber of the wheel and the vehicle's handling.

4.3.2.1 Tyres and Rims

In order to minimise energy losses, low rolling resistance tyres were specified for the Mamba EV. Continental EcoContact 5 tyres and A-line Mischief alloy rims with a 35 mm offset were selected due to their availability, affordability, and energy efficiency rating. At the front of the vehicle, 185/55-R15 tyres were used, while at the rear, a larger 225/45-R17 tyre was used. Care needs to be taken when selecting rims since the offset influenced the track, the scrub radius, and the roll axis.

4.3.2.2 Suspension Arm Mounts

In order to finalise the angles of suspension mounting panels in the chassis, as well as the location of the suspension arms on the mounting panels, the following parameters needed to be calculated and refined.

Roll Axis

Setting the roll axis had the greatest influence on the angle of the suspension mounting panels. Using the CAD geometry of the suspension system in NX, and the process outlined in Figure 2-10, the roll centre height was calculated for both the rear and front of the vehicle. For a fixed track, changes to the suspension arm angle affected not only the roll centre height, but also resulted in a lateral movement of the suspension mount panel, either enlarging or reducing the space available in the nose or tail sections of the chassis. The roll centre height at the CoG was calculated to be 42.7 mm.

Scrub

The scrub radius was calculated at the front wheels using the suspension model and a model of the tyre and rim, by measuring the lateral distance between the contact patch and the point of rotation on the ground plane. By adjusting the diameter of the selected tyre, the scrub radius could be varied, however to keep the ride height constant the vertical position of the suspension mounts had to be altered. The scrub radius for both the front and rear suspension was calculated to be 42mm.

Caster

The main constraint on the caster angle was the dimensions of the coil of the front shock absorber. The coil connects to the lower A-arm then passes through the 'V' of the upper arm. Based on the geometry of the suspension it was decided to set the caster angle on the front suspension knuckles to positive 8°, ensuring there was enough clearance for the coil for the full range of movement of the suspension system.

4.3.3 Shock Absorbers and Springs

The suspension system for the EV comprised a commercial shock absorber and a custom-made spring, which were selected and designed by a member of the project group (Sim et al., 2016). The shock absorber was directly mounted to the lower suspension arm, without a pushrod or rocker, and a steel mounting bracket was fastened to the suspension mount panel, passing through the fork of the upper suspension arm. The selection of the shock absorber and the mounting angle dictated the mounting position of the upper mounting bracket. In manufacturing the springs, it was critical to ensure that there was clearance between the upper suspension arm and the coils for

the full range of motion. Using an NX model, the maximum outer diameter of the spring was determined, which, coupled with the required spring rate and length, defined the spring for manufacture.

4.4 Chassis Design

The geometric design of the chassis was undertaken in three phases; the design of the inner tub structure to which the vehicle components would mount, the design of the outer shell of the vehicle which defines the aerodynamic surfaces of the EV as well as the aesthetics, and then the merger and refinement of these two structures, resulting in the completed chassis.

4.4.1 Initial inner structure

The inner tub of the chassis was designed using the constraints imposed by the spatial model in Figure 4-1. The primary focus of the design of the inner tub was to maximise the use of laminate plates, which would reduce manufacturing complexity and time. By maximising the use of laminate plates the number of moulds required was also reduced. The configuration of the initial inner structure is shown in Figure 4-7.

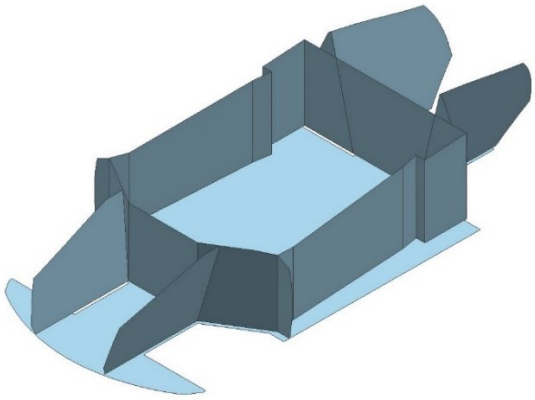

Figure 4-7. Initial inner chassis structure.

In order to keep the passenger cabin of the vehicle separate from the front and rear compartments, two firewalls were used. The firewalls were the primary lateral members in the vehicle, and provided a secure region to mount the heavier vehicle components such as the motor controllers and the battery charger.

The shape of the base panel was largely dictated by the suspension assembly and the wheels, as seen in Figure 4-12. The cut-outs needed to ensure that the tyres could freely rotate without coming into contact with the chassis in motion, as well as in turning. In order to verify turning

clearance, a turning profile of the tyre was produced on the plane that intersected the rotational centre of the tyre and passed closest to the chassis, as shown in Figure 4-8.

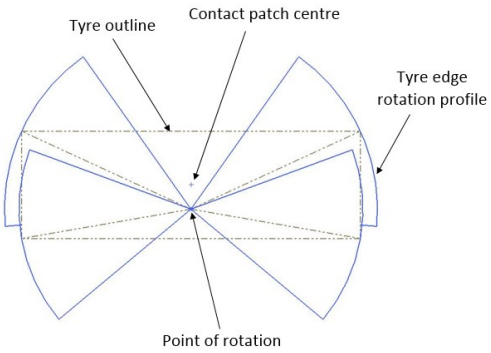

Figure 4-8. Tyre rotation profile for the front right tyre.

4.4.2 Initial Outer Body

The initial outer body shape of the chassis, illustrated in Figure 4-9, was designed and provided by a member of the Mamba EV project (Sim et al., 2016). The author worked with the team member to refine the body to meet the required specifications based on constraints imposed by selected components, such as the windscreen and suspension, as well as ensuring that the occupants could access and operate the vehicle. Aesthetics also had a large influence on the development of the outer body. The windscreen, purchased commercially, was three-dimensionally scanned to generate a field of points from which a virtual surface could be generated. This surface was used to design the frame in which the windscreen would be mounted. Using the frame and the height of the human models, the height and positioning of the roof could be set. The tyre dimensions were used to define the final dimensions for the wheel arches, allowing enough clearance for suspension travel, without the need for a suspension bump stop.

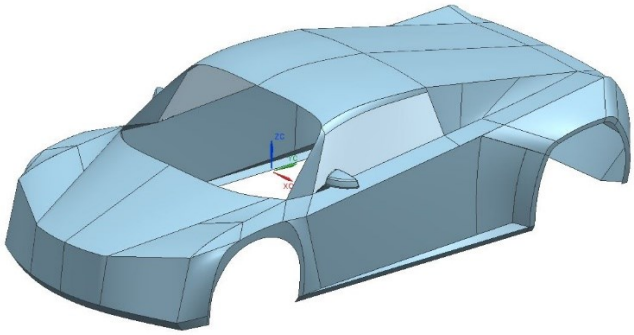

Figure 4-9. Outer body of the Mamba EV.

Based on aesthetics, several regions were then refined. These regions were the entire roof section, including the A-pillars, rear bumper, side panels, and wheel arches, which can be seen in Figure 4-12. This resulted in the structure seen in Figure 4-10.

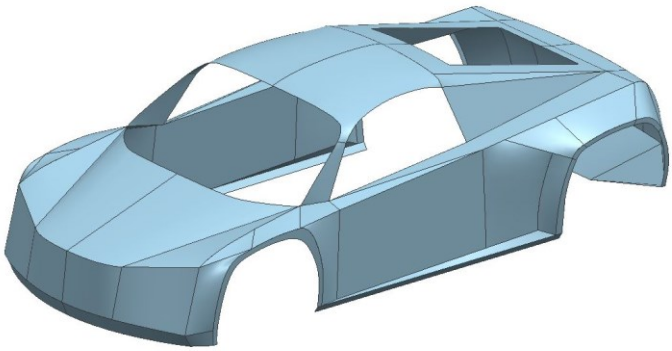

Figure 4-10. Aesthetically refined outer body.

4.4.3 Body Integration and Refinement

The monocoque chassis was formed by integrating the inner structure with the outer body, and then refining the model. The refinements undertaken were influenced by the results of associated computational fluid dynamics modelling (Sim et al., 2016), the spatial requirements of the components during assembly and operation, and the surface preparation required for modelling the chassis' constituent laminate lay-ups.

4.4.3.1 Refinements due to Aerodynamic Characteristics

Modifications to the chassis' spatial design to achieve improvements in aerodynamic performance could only be made to a limited extent due to the development time available (one year). These time constraints resulted in the commencement of the manufacture of the composite monocoque internal structure prior to the completion of the aerodynamic design of the outer body. This compromise was accepted by the project team since the aim of the prototype was to serve as a step towards securing funding for the development of a second iteration of the Mamba EV, one in which emphasis could be placed on aerodynamic optimisation.

4.4.3.2 Refinements due to Components Constraints

In order to ensure that the EV could be assembled, consideration had to be given to component access, as well as ease of component mounting. An integration sequence and process had to be developed for the formation of the chassis, as well as for the component installation process, prior to the completion of the chassis geometry. Component positioning and access also had to account for future maintenance and component replacement.

Regarding the battery, safety was a primary concern in both manufacture and assembly. Since the battery packs operated at high voltage, accidental contact could be hazardous or potentially lethal, and the cells therefore had to be contained to prevent contact by the passengers. Containment also prevented the chance of conductive objects falling across battery cell terminals, which could have shorted-circuited the modules, resulting in combustion.

The high voltage cable linking the front and rear battery packs ran inside a centre channel, shown in Figure 4-11, which also contained low voltage cabling between the various components of the vehicle. As well as forming a housing for the cabling, the channel contained the brake lines for the rear brakes, the coolant tubes for the motors, and the hand brake cable. In order to provide an accessible mounting point for the manual disconnection switch for the battery pack the end of the central channel widens towards the rear of the vehicle. The widened section also formed a mounting point for the directional control for the motor and miscellaneous electronics.

The steering rack was required to be mounted in plane with the tie rod connections on the front suspension, which meant it needed to be mounted above the front battery pack in the nose of the vehicle. The steering rack was mounted to a composite channel bonded directly to the front suspension mount panels, seen in Figure 4-11.

Openings were required in the sides of the tub structure to allow for passenger access into the cabin of the vehicle. The dimensions and shape of the cut-outs were based on the position of the human models within the spatial model, the ability and ease for a person to enter the vehicle, as well as aesthetics. Due to time constraints it was decided to leave the prototype chassis without doors initially, but make allowance in the composite lay-up for doors to be installed at a later date by bonding in an aluminium hardpoint in the sill to allow for door hinges. This meant that for experimental testing of the prototype's range and handling characteristics, simple plugs would be made to seal the door openings to improve aerodynamics. Based on the possibility that one might drive the vehicle without doors, at least initially, it was decided to ensure that the passengers sat further back in the vehicle than the end of the door cut-outs, shown in Figure 4-6. The chassis tub sills account for a large portion of a vehicle's torsional stiffness and therefore, since large regions of the tub sides had been removed, the sills needed to be reasonably deep to compensate for this.

4.4.3.3 Refinements Due to Model Preparation

For modelling the loading induced by the major components' masses, the least computationally expensive method was to represent the masses as appropriately positioned mass points and link those to the component footprint on the chassis using one-dimensional elements. This required the footprints of the major components to be split from their mounting panels. The footprints were split for the battery modules, the seat rails, the motor controllers, the battery charger, and the motor assembly. The points that would be defined as mass points were placed at the individual centre of masses for each of these components in the CAD model.

In order to generate a continuous mesh across the chassis, the boundaries of the surfaces that defined the CAD geometry needed to be connected. In Siemens NX, this can be done either by using the sewing tool in the part file, or by the stitching tool in the FEM file. It was advised by a consultant at Esteq, the South African agents for Siemens NX, to preferably sew the surfaces than stitch them. This is since surfaces in the part file are boundary-represented and follow defined rules and equations, but once opened in an FEM file, the geometry is converted to a mesh or tessellated representation.

The clearly defined nature of the boundary-represented geometry results in a more stable mesh. However, it was also suggested that the model in the part file should be sewn in a few large sections rather than a single overall section, since if ever a section of the model needed to be reloaded due to mesh instability or errors, only that particular section would need to be re-meshed, rather than the entire model. This approach was adopted and the model was sewn into fourteen sections.

For regions on a cored laminate with high, localised loading, hard-points needed to be inserted to prevent crushing of the core. Per general practice in composite structures manufacture, bolted sections should include hard-points. These localised regions within a surface needed to be split from the surface, defining their own boundaries. This allowed the author to apply a variation in the panel lay-up in that region. The regions of concern were the brake pedal mounting panel, the handbrake mounting panel, and the base section to which the motor assembly was mounted.

4.4.4 Final Chassis Geometry

After the adjustments for vehicle components and refinements to the CAD geometry for a less complex and more stable discretization process had been made to the chassis structure, the final geometry was ready to import into an FEM file for discretisation and material allocation. The structure was split by colour into regions which would share the same composite lay-up. The selection of the regions was influenced by the manufacturing procedure and assembly of the

chassis. The final internal structure and the terminology used for its associated regions can be seen in Figure 4-11. The finalised outer structure and the terminology used for its associated regions can be seen in Figure 4-12. The final integrated chassis structure can be seen in Figure 4-13.

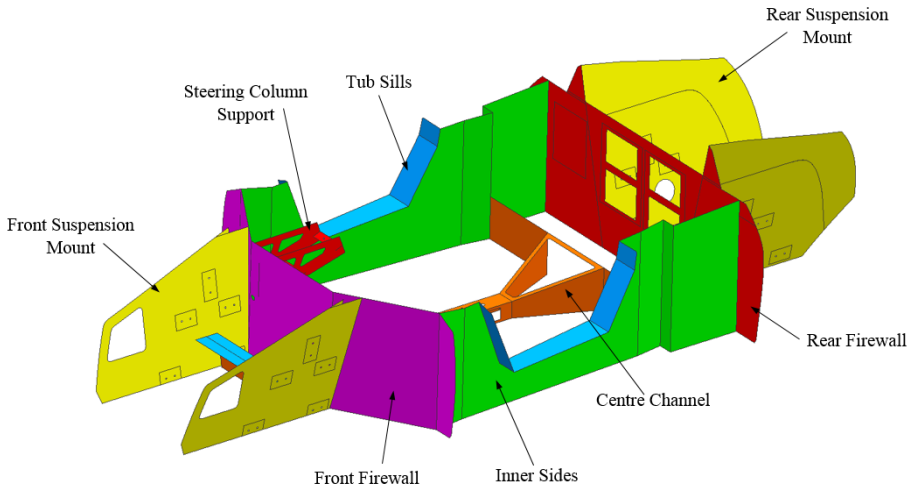

Figure 4-11. Final internal chassis structure and region terminology.

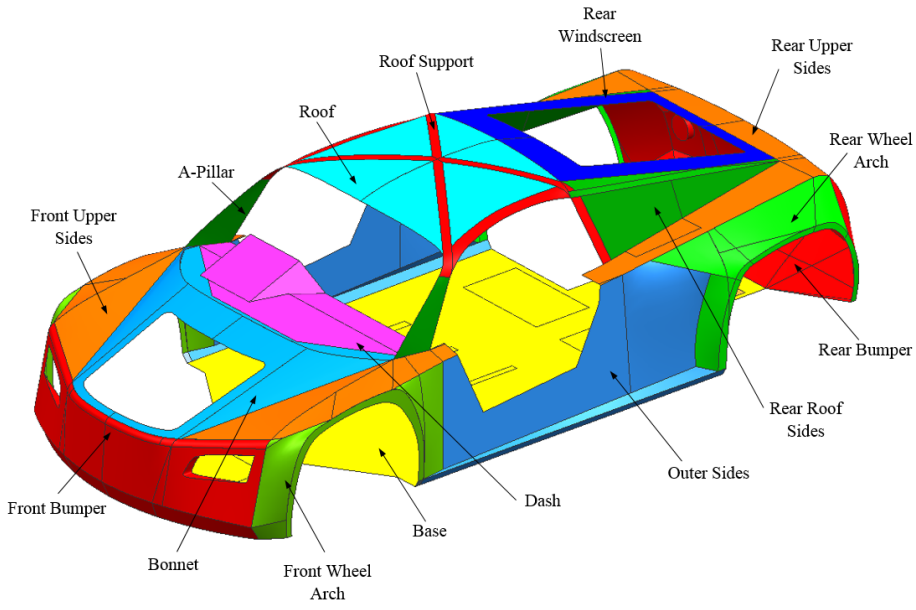

Figure 4-12. Final outer surface geometry and region terminology.

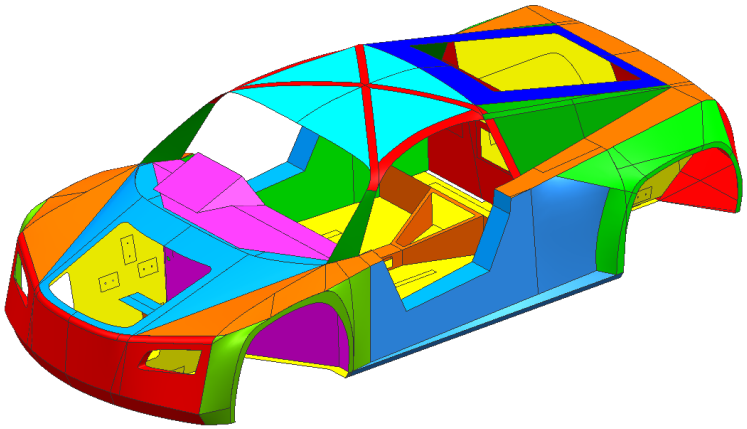

Figure 4-13. Final chassis model for the Mamba EV.

4.5 Final Mechanical Specifications

After the spatial layout and the chassis geometry had been finalised, the mechanical specifications of the Mamba EV were fixed. These can be seen in Table 4-3.

Table 4-3. Final Mamba EV chassis and suspension specifications.

Tyres	Front	185/55R15 (Ø 584.5 mm, Wall Height 101.75 mm)
	Rear	225/45R17 (Ø 634.3 mm, Wall Height 101.25 mm)
Brakes		Wilwood - 120-9736-SI
Windscreen		Mazda MX5
Wheel Base [mm]		2350
Length [mm]		3605
Width [mm]		1730
Track [mm]	Front	1510
	Rear	1495
Suspension Arm Angle [Front]	Upper	9° (Down)
	Lower	1.5° (Down)
Suspension Arm Angle [Rear]	Upper	8° (Down)
	Lower	2° (Down)
Suspension Mount Plate Angle	Front	11.62°
	Rear	13.14°
Shock Length [mm]	Front	325.45
	Rear	308.97
Roll Centre Height [mm]	Front	43.44
	Rear	42.05
Scrub Radius [mm]		41.93
Centre of Gravity	X	102.06
	Y	0.856127319
	Z	102.8316164
Mass Distribution [%]	Front	46.3
	Rear	53.7
	Left	49.94
	Right	50.06

4.6 Chapter Conclusion

The design process for the development of the geometric structure of the Mamba EV chassis is described in this chapter. The design considerations that influenced the shaping and refinement of the structure have been examined, as well as the component layout for the EV. With an emphasis on handling, parameters were calculated based on the final setting and mounting of the suspension geometry, as well as the final placements of components; this significantly influenced, and was influenced by, the vehicle weight distribution. Finally, the mechanical specifications for the prototype Mamba EV were defined.

CHAPTER 5

Preliminary Model and Analysis

The following chapter explores the discretisation of the developed two-dimensional geometric model, as well as the designation of materials to surfaces of the model within the FEM file. The initial anticipated zone-based composite laminate lay-up is also defined by applying material properties to the individual faces of the chassis structure. The global forces and boundary conditions are then applied, and the initial results of the four monitored parameters based on the anticipated composite lay-up are obtained.

5.1 Model Preparation

As discussed in section 4.4.3, a continuous surface was required to avoid a discontinuous mesh at surface edges, which resulted in the author stitching the sections sewn in the part file in the FEM file. The NX stitching tool requires the user to specify either an edge-to-edge stitch or an edge-to-surface stitch, both allowing for orthogonal surface stitching, ensuring a continuous mesh between sewn regions.

5.2 Material Properties and Collector Creation

In order to simulate the response of a structure to a defined load, material properties need to be specified and assigned to the structure. For the prototype chassis, a zone-based process was followed, where materials are assigned to the surfaces and bodies by being defined in material collectors. Collectors allow the user to group meshes with the same material properties without having to individually assign the properties to every mesh. Collectors were created following the regions defined in Figure 4-11 and Figure 4-12. Within the *laminate physical properties* tool in the FEM file, the laminate stacking recipe, fibre orientation, ply thicknesses, failure criteria, and reference properties were defined. The laminate physical properties of the various laminate panels were defined and then assigned to the relevant collectors. Since the analysis was being done on a two-dimensional structure, a two-dimensional orthotropic material definition was used for the defined materials. This material definition requires three material constants, E_1, E_2, ν_{12}, to define the composite ply. In addition, stress limits were also required for the failure criteria used.

Based on research concerning fibre reinforced plastic composite materials, it was decided to use a twill weave fabric reinforcement with an epoxy matrix, due to the fabric's drapability, availability, and cost, while the resin was chosen due to its comparably high mechanical strength. The mechanical properties for 200 g/m^2, 2/2 twill weave (Engineered Cramer Composites, 1994) laminate with an Ampreg 21 epoxy matrix (Gurit, n.d.-a) was obtained from the Durban

University of Technology's Composite Research Group, which has experimentally derived mechanical properties for the above constituent combination. These data are given in Appendix A, Table A-1.

Since the aramid fibre and glass fibre with epoxy resin plies were used for non-structural purposes, a general set of mechanical properties was used (ACP Composites, 2014). These properties are provided in Appendix A, Table A-2 and Table A-3.

The mechanical properties associated with the PVC core materials were obtained from a supplier-provided datasheet (Gurit, n.d.-b). AMT Composites stocked the Gurit Corecell M60 3 mm sheets, and the Gurit Corecell M80 10 mm and 20 mm sheets. The material properties for the CoreCell M60 and CoreCell M80 PVC cores are shown in Appendix A, Table A-4 and Table A-5 respectively.

For the component mounting hardpoints, a combination of marine plywood and aluminium were used. The properties of the marine plywood can be found in Appendix A, Table A-6 (Forest Products Laboratory, 1999). For the aluminium hardpoints, a 6061 grade was used, for which the material properties are shown in Appendix A, Table A-7 (ASM International, 1990).

5.3 Material Orientation

In composite structure analysis, correctly orientating the fibres of the laminate relative to the structure being analysed is critical for accurate solution. In order to differentiate between the fibre direction of the laminate and the material direction of the mesh, the fibre orientation axes are denoted 1 and 2, and the material mesh direction are denoted x and y, with the z axis perpendicular to the element surface. When applied to the mesh, the laminate fibre 1-axis follows the x-axis of the element. After initially meshing a panel, the material direction for each of the elements do not necessarily point in a uniform direction, but are arbitrarily orientated, which in the case of an isotropic material definition, does not matter. For an orthotropic material definition, the material orientation of the individual elements within a surface are required to be orientated in the same direction. This could be defined in the *Mesh Associated Data* tool by defining the material orientation either in the direction of a vector, specified angle, or tangent curve. The material mesh direction for each of the panels of the chassis were orientated by vector, with the x-axis running longitudinally or in the direction of travel, except for the lateral structural members such as the firewalls, which were orientated with the x-axis running laterally.

5.4 Ply Failure Theory

After a discussion with a consultant from Esteq Pty (Lotus Cars Ltd), it was decided that the Tsai-Wu failure theory (Tsai & Wu, 1971) was the most appropriate failure theory to employ for the load case simulations due to its widely-accepted application in industry. The Tsai-Wu failure theory requires the strength limits of the materials used to be defined, as well as a stress interaction term F_{12}, which is required to be calculated using experimentally obtained strength values. However based on the work by H. M. Adelman and R. Narayanaswami (Adelman & Narayanaswami, 1977), it is reasonable for the F_{12} factor to be taken as zero. In order for NX to calculate the ply and bond failure criterion, the laminate modeller requires the interlaminar shear strength of the resin to be defined within the *Laminate Physical Property* tool. The interlaminar shear strength of Ampreg 21 epoxy is 50 MPa when the slow hardener is employed (Gurit, n.d.-a).

5.4.1 Failure Criterion

The two parameters observed in the simulation post processing that indicate predicted failure are the ply failure index and the bond failure index. Both criterion are scalar and unitless. A ply failure index greater than 1 indicates potential failure in a region within a single ply, where a bond failure index greater than 1 indicates potential delamination between plies.

5.5 Initial Anticipated Lay-up

In order to have a starting point for the chassis analysis an initial lay-up had to be anticipated. Based on prior composite materials experience, it was decided to use a four ply laminate as a base lay-up. This laminate comprised two plies of 2/2 twill weave fabric, orientated 0/90, and two plies of 2/2 twill weave fabric (Engineered Cramer Composites, 1994), orientated -45/45, impregnated with Ampreg 21 epoxy resin (Gurit, n.d.-a). Regions that were thought to require more stiffness were thickened with a PVC core. A 3 mm PVC core was applied in the roof structure and bonnet, a 10 mm PVC core was used in the front and rear firewalls and in the suspension mount panels, and a 20 mm core was used in the base panel. The base panel also incorporated an aramid fibre layer for penetration resistance. For the components that required bolted joints for mounting, marine plywood was initially used for the hardpoints.

5.6 Meshed Model

For the discretization of the Mamba EV chassis, several different types of mesh elements were used, which influenced the runtime of the simulations and the accuracy of the results.

5.6.1 Zero-Dimensional Elements

In order to simulate the component loads on the chassis, the centre of masses needed to be modelled. Each of the components, as mentioned in section 4.4.3.3, was modelled as a CONM2 0D concentrated mass element, each with their own assigned mass. Each element was linked to a point in the model at the mass centre for each of the components. The 0D points were then linked to the rest of the model using a point-to-surface connection element, joining the mass centre points to the surface split base profile of the component they represented.

5.6.2 One-dimensional Elements

For the simulation, 1D elements were used to model the suspension assemblies, steering column, handbrake, rear suspension mount panel support bar, and the connections between nodes and edges or faces.

Since the suspension system had been purchased, the ability of the suspension arms and knuckle to survive the expected loads was not a concern. This was decided due to the fact that the Birken suspension was performing without failure in vehicles in the same weight class as the Mamba EV. It was therefore decided to model the assembly as an infinitely stiff structure in order to more accurately load the chassis by applying loads at the contact patch, and not at the suspension arm brackets on the suspension mount panels. A CBEAM element type was used, with a circular cross section and wall thickness that resulted in the correct suspension system mass, but with an exaggerated cross section diameter to increase geometric stiffness.

The steering column was modelled to test the steering column supports under load when the driver applies their weight to it. The steering column was modelled as a 32 mm tube with a 4 mm wall thickness using CBEAM elements.

Like the suspension system, the handbrake had been purchased and therefore the primary concern was the response of the handbrake mounting panel, which was the top of the central channel. The handbrake was modelled using CBEAM elements with a 30 mm circular cross section.

5.6.3 Two-dimensional Elements

For the Mamba EV chassis model, 2D meshing formed the bulk of the model discretization. 2D elements were used for the chassis, for the suspension arm mounts, the handbrake base, and the windscreen. Since a large portion of the chassis comprised flat panels or panels with low curvature, a CQUAD4 element type was used, which required fewer nodes in comparison to using second order CQUAD8 elements. For the initial model mesh a 10 mm base element size was used as a starting point, which was locally refined based on the initial results.

5.6.4 Three-Dimensional Elements

In order to accurately model the mass of the motors, while applying the required torque loads, the motor was modelled as three dimensional, and was meshed using CTETRA4 elements. A coarse base element size of 10 mm was used since the reaction of the motor structure was not of interest in the model, and therefore little accuracy in this region was needed. Having a coarser mesh on the motor helped to reduce simulation runtimes by having fewer nodal points.

5.7 Simulation Set-up

Before a simulation can be analysed, the model imported from the FEM file needs to have boundary conditions that most closely represent reality applied to it to ensure that the global stiffness matrix [K] is not singular. This prevents the body moving as a rigid structure in space. In order to solve for the displacement of the structure, known global forces need to be applied.

5.7.1 Loads

In order to accurately simulate a range of vehicle operating scenarios, the relevant loadings had to be determined. Based on research it was found that generalised static load limits haven't been globally formalised, but rather, it appears that manufacturers determine their own set of criteria in their designs based on experimental failure testing. For a vehicle to be roadworthy in South Africa there are no structural standards to comply with, however the vehicle needs a certificate of roadworthiness.

Abuse loads experienced by a vehicle vary with time and therefore a dynamic finite element analysis achieves a better representation of reality than a static one. However, for an initial prototype, static analysis, implemented correctly, gives a conservative indication of the responses of the chassis within a relatively shorter time period, due to lower modelling complexity (Blundell & Harty, 2015). A dynamic analysis can subsequently be done to optimise the composite structure.

5.7.1.1 Torsional Stiffness

For the torsional stiffness model there is no specific load since the parameter of interest is the degree of angular rotation about the longitudinal axis. Two equal but opposite loads of 1000 N were applied on the chassis for this simulation, one on each of the front wheel contact patches in the z- and negative z-direction, shown in Figure 5-1.

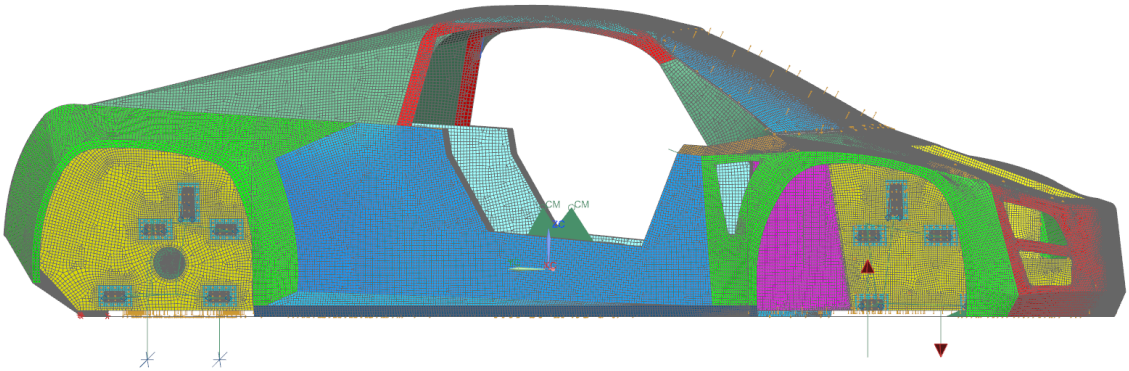

Figure 5-1. Torsional stiffness loads and constraints.

5.7.1.2 Motor Induced Loads

In order to simulate the loading on the chassis induced by the motors, a worst case scenario needed to be determined. It was determined that the peak applied loads due to the motors would be at the instant of maximum acceleration from standstill, where the motors would be producing peak torque. The maximum torque the motors can output is 800 Nm, which was applied to each outer cylinder (output shaft) of the motor geometry, with a 7 m/s^2 peak acceleration field being applied to the entire body. The loads are visualised in Figure 5-2. The peak acceleration was determined based on a full vehicle energy model produced by a member of the team (Woods, 2018).

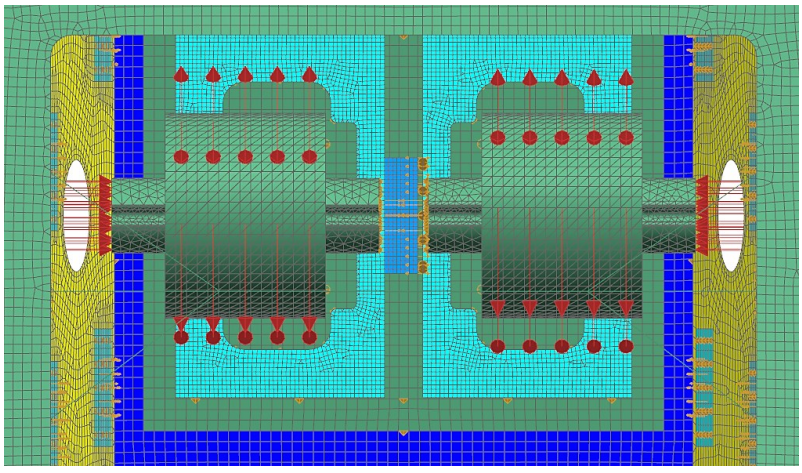

Figure 5-2. Motor induced loads.

5.7.1.3 Operational Loads

The operational and shock loading simulation conditions for modelling the prototype were based on the static loading scenarios outlined by Blundell and Harty (2015), these are:

1. Vertical bump (3G)
2. Vertical rebound (2G)
3. Lateral cornering - outer wheel (0.75G)
4. Lateral cornering - inner wheel (0.75G)
5. Forward braking (1G)
6. Reverse braking (0.35G)
7. Kerb impact
8. Pothole braking

For the kerb impact and pothole braking scenarios, a 'G' loading was not specified therefore it was decided to proportionately scale the loading specified by Blundell and Harty between the mass they used for their wheel loading and the mass on the relevant wheel of the Mamba EV.

The load cases will not always be experienced independently. Coupled load cases, such as the scenario of cornering at 0.75 G and striking a curb on an outer wheel, result in higher loading and were taken as the worst case scenarios. For cornering, the chassis needs to survive loading for both right and left turns, but since the suspension mount panels are symmetric, turning in only one direction was analysed. For the forward travel braking scenarios, only pothole braking cases for the front wheels were analysed since, in comparison to the independent 1G braking load case, the loads were more severe in the same directions. The final operational loading scenarios used for the simulations were,

1. A 3 G bump load applied at each wheel independently, while the remaining three wheels were constrained.
2. A 2 G rebound load applied at each wheel independently, while the remaining three wheels were constrained.
3. A 0.75 G cornering load coupled with a kerb impact, with the kerb impact being applied at each outer wheel independently, while the remaining three wheels were constrained.
4. A pothole braking load applied at each wheel independently, while the remaining three wheels were constrained.
5. A 0.35 G reverse braking load applied at each wheel independently, while the remaining three wheels were constrained.

Due to the uncertainty of the load magnitude used for the prototype, a one and a half times safety factor was applied to the above coupled load cases (US Department of Defense, 2002). To reduce this level of uncertainty, the prototype could be experimentally tested to develop a more accurate

set of test conditions for future iterations of the Mamba EV. Based on the calculations shown in Appendix B, equations (B.1) to (B.25), the loads used for each scenario are shown in Table 5-1.

Table 5-1. Operational and shock loads.

Load Case	F_x [N]	F_y [N]	F_z [N]
3G Bump (Front)			6851.3
3G Bump (Rear)			7946.1
2G Rebound (Front)			-4567.54
2G Rebound (Rear)			-5297.4
0,75G Cornering & Kerb (Outer Rear Wheel)		9467.655	6768.81
0,75G Cornering & Kerb (Outer Front Wheel)		7958.895	5563.77
1G Braking (Front Wheel)	-4684.55		6246.06
1G Braking (Rear Wheel)	-2711.07		3614.76
0,35G Reverse Braking (Front Wheel)	3004.43		4005.9
0,35G Reverse Braking (Rear Wheel)	4391.19		5854.92
Pothole Braking (Front)	9740.84		7572.12
Pothole Braking (Rear)	11297.37		8782.11

5.7.1.4 Localised Loads

Within the vehicle cabin several components experience loading exerted by the driver, namely the handbrake, brake pedal, and steering wheel. The mounts of these components required localised testing to ensure that the panels they were mounted on did not fail under loading. The loads used were based on worst case estimates and were deemed to be conservative.

For the handbrake, the worst loading case was taken to be a 70 kg load oriented vertically at the end of the lever arm, shown in Figure 5-3. The worst case scenario loading for the brake pedal was taken to be a 150 kg load longitudinally on the tip of the brake pedal arm, shown in Figure 5-4. For the steering column, the worst case loading scenario was taken as the full weight of the driver pulling down on the steering wheel, which could occur during ingress, egress, or during a shift of seating position. The load applied in the analysis was 140 kg vertically downwards on the end of the steering column shown in Figure 5-5.

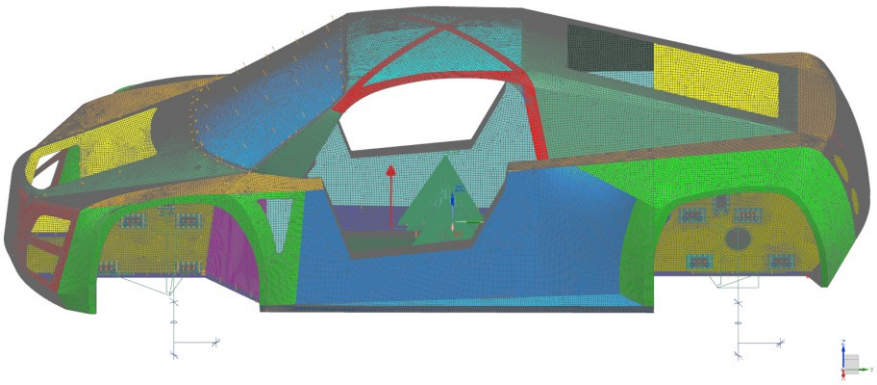

Figure 5-3. Applied handbrake load.

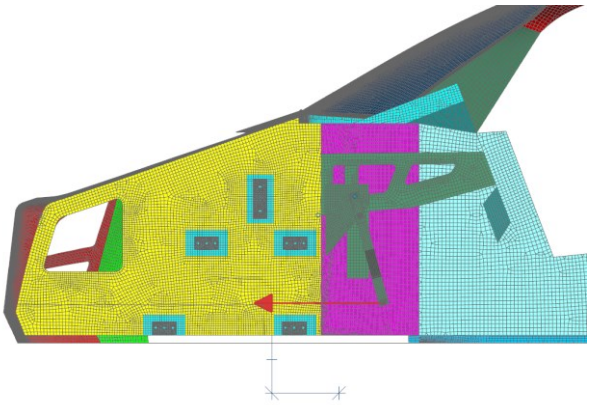

Figure 5-4. Applied brake pedal load.

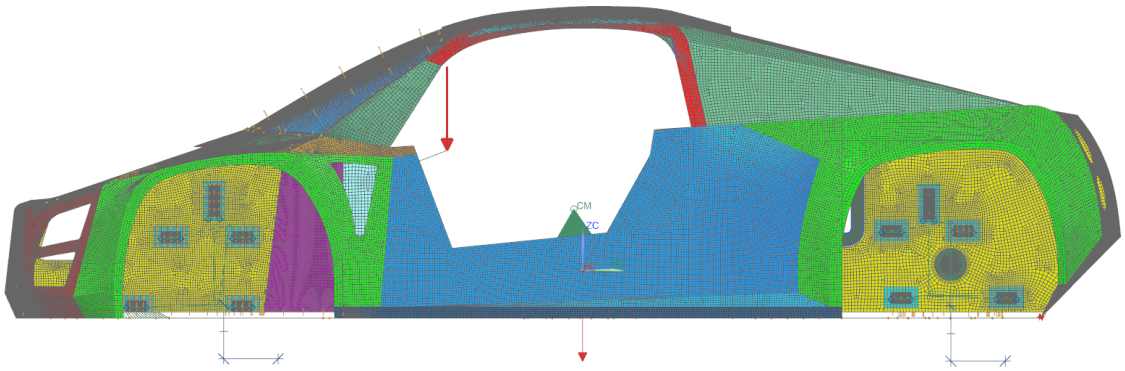

Figure 5-5. Applied steering column load.

5.7.1.5 Roof Loads

Due to time constraints it was decided that for the prototype car, the chassis would be designed via a carefully conducted static analysis, and that a focus on vehicle safety and crash analysis, including crumple zones, would be a primary focus of future structural modelling activities. However, in order to ensure that the roof structure could withstand a vehicle roll-over, a 5 G load was applied vertically downward on the roof panel, shown in Figure 5-6. This correlated to a load of 32.85 kN.

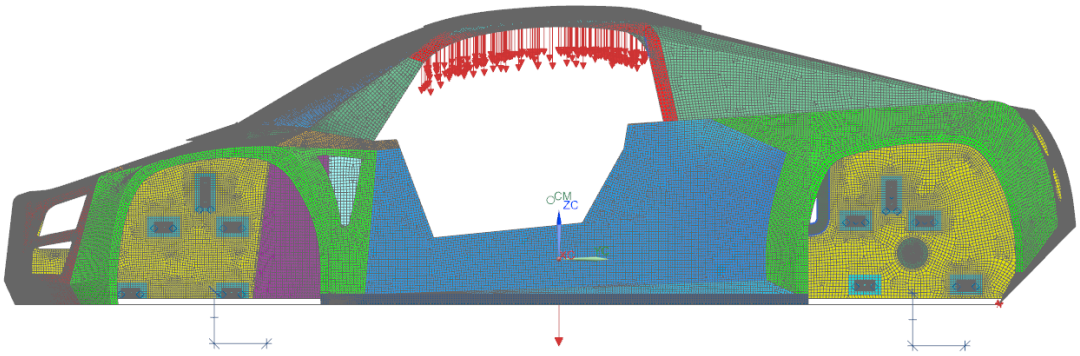

Figure 5-6. Applied roof load.

5.7.2 Constraints

While analysing the Mamba EV chassis the global constraints were applied at the contact patches of the wheels. With the loads for each scenario being applied at individual contact patches, the remaining wheels were constrained using user defined constraints, allowing any of the six degrees of freedom (DOF) to be fixed. By default, all nodes imported from the FEM file to the sim file are unconstrained. In order to avoid inducing artificial chassis stiffness careful consideration had to be given to the physical nature of each constraint applied.

5.7.2.1 Torsional Stiffness Model

For the chassis torsional stiffness model the front two wheels were loaded, without the chassis experiencing a gravitational field, and the rear two wheels were constrained.

5.7.2.2 Motor Induced Loads

For the motor induced load scenario all four wheels had a completely fixed constraint applied, since the focus of the analysis was on the response of the chassis base to the motor loading, not on the response of the suspension geometry.

5.7.2.3 Operational Loads

For the operational loads one of two user defined constraint scenarios were used for each of the analyses. The first group of simulations (3 G bump, 2 G rebound, reverse braking, and pothole braking) were all constrained in the same manner, whilst the second group of simulations (coupled 0.75 G cornering and kerb strike) were constrained differently, as described below.

For the first group of simulations mentioned, the load was applied on either a front or rear wheel, with the other three wheels constrained. The wheel laterally opposite to the load was translationally constrained in lateral and vertical direction, and rotationally constrained about the

vertical axis. For the longitudinally opposite wheels, all three translational directions were constrained, and rotation was constrained about the vertical axis. By leaving the laterally opposite wheel to translate in the longitudinal direction, the distance between front and rear contact patches was allowed to vary as the chassis flexed due to the applied loads, which more accurately represented the vehicle response. All three constrained wheels were allowed to rotate about the longitudinal and lateral axes, which essentially allowed the model to pivot about the contact patches in the longitudinal-lateral plane, preventing artificial stiffness being provided to the chassis.

For the second group if simulations mentioned, the wheel laterally opposite to the load was constrained only in the vertical translational direction and about the vertical rotational axis, while the longitudinally opposite wheels were constrained in all three translational directions and about the vertical rotational axis. Since the load was being applied laterally, permitting the laterally opposite wheel to translate in the longitudinal-lateral plane resulted in bending within the chassis. This approach provided a more accurate representation in comparison to a translationally-fixed laterally opposite wheel, which would result in compression of the chassis.

5.7.2.4 Localised Loads

For the localised loads the primary focus of the analyses was to specifically monitor the response of the mounting panels, not the response of the entire chassis. Therefore all the contact patches were fully constrained.

5.7.3 Simulation Object Type

In Siemens NX, within the sim file, the *simulation object type* tool allows the user to define interactions between different faces and edges of the model. The user can define contact or glued connections between two surfaces, or an edge and a surface. For the chassis of the Mamba EV, panel-edge-to-surface joins were connected using gluing, rather than continuously stitched surfaces. For this scenario gluing was more accurate since when a two-dimensional meshed surface that is continuously connected along an edge experiences a load that causes bending, only the edge resists rotation, where in reality the load is distributed along the thickness of the panel. By gluing the edge to the surface, load distribution across the thickness of the surface is achieved. When modelling the surfaces, a gap of half the thickness of the mounting surface was left between the two-dimensional surface and the joining edge. This ensured that artificial stiffness was not created in the region by elements overlapping at the join.

5.8 Initial Simulations

Based on the initial anticipated lay-up, applied global loads, and constraints for the various loading scenarios, results were obtained for each of the load cases. These initial results were used to determine critical areas in the chassis that required localised mesh refinement for a more accurate analysis, and for regions of failure based on the failure criteria specified. Four parameters were monitored in particular: chassis deflection, ply stress, ply failure, and bond failure. A first ply failure approach was taken, meaning that if any element within a ply failed, the chassis was considered to have insufficient strength in that region. An iterative process of refinement was then undertaken to ensure survivability across all load cases. The monitored results are tabulated, with the peak stresses being referenced to the relevant composite ply identification number. For the stresses and failure criterion seen in the following results tables within this thesis the identification numbers for the corresponding plies were denoted by roman numerals for easier differentiation from the result itself.

5.8.1 Torsional Stiffness

Based on the results of the initial torsional stiffness simulation, the chassis torsional stiffness was calculated, as shown in Appendix B, Equation (B.26). Due to the slightly non-symmetrical nature of the chassis there was a fractional difference in the deflection of the chassis at each front wheel relative to the ground plane. However, since the variation in the deflection was small enough to be considered insignificant relative to the track width, an average of the two deflections was used in the calculations. Based on the applied loading conditions and constraints, an average deflection of 2.408 mm was measured, resulting in a torsional stiffness of 8263.16 Nm/deg. Due to the later refinements to the chassis lay-up, to ensure survivability under all other loading scenarios, the chassis stiffness changed. It was therefore revaluated after the chassis laminate structure was finalised.

5.8.2 Motor Induced Load Case

The motor induced loading scenario focused on ensuring that the chassis base could withstand the induced motor load, without excessive deflection or failure. The reaction of the motor base hardpoint was also monitored to ensure that a marine plywood core was suitable for the application. The results of the initial simulation can be seen in Table 5-2.

Table 5-2. Motor induced load case initial results.

Deflection [mm]	Peak Ply Stress [MPa]					Ply Failure Index	Bond Failure Index
	σ_{11t}	σ_{11c}	σ_{22t}	σ_{22c}	σ_{12}		
2.32	43.73[V]	-62.62[V]	36.57[II]	-87.5[V]	13.9[IV]	0.243[III]	0.323[III]

Based on the deflection results, a peak displacement of 2.3 mm occurred on the roof edges, above the door openings, with the centre of the base panel experiencing a displacement of 2 mm. The deflection experienced is a result of the passenger mass, rather than the loading induced by the motors. There was no significant deflection of the chassis base beneath the motor assembly relative to the surrounding region, indicating that the base had sufficient strength and stiffness to support the drive train.

The peak stresses predicted by the simulation were well below the strength limits of the material, and this, in conjunction with the maximum ply and bond failure indices of 0.243 and 0.323 respectively, indicated good survivability of the chassis.

5.8.3 Motion Load Cases

Simulations for the five operational load cases were run based on the specified loads and constraints, with the peak results for the four monitored parameters summarised in Table 5-3. These results were used to determine areas of weakness within the chassis, and to provide a starting point for the iterative process of refining the composite laminate lay-up. The load cases are denoted by numbers as follows:

1. 3G Bump load case
2. 2G Rebound load case
3. Coupled cornering and kerb strike load case
4. Pothole braking load case
5. Reverse braking load case

Table 5-3. Operational load cases' initial results.

		Deflection [mm]	Peak Ply Stress [MPa]					Ply Failure Index	Bond Failure Index
			σ_{11t}	σ_{11c}	σ_{22t}	σ_{22c}	σ_{12}		
1)	**Front**	40.97	377.04[V]	-357.73[V]	307.98[II]	-340.21[I]	47.05[IV]	7.24[III]	0.521[III]
	Rear	33.95	479.11[II]	-430.56[V]	356.04[IV]	-318.28[II]	53.66[IV]	7.16[III]	0.601[III]
2)	**Front**	54.56	510.14[V]	-519.72[V]	397.31[IV]	-409.23[II]	64.82[IV]	9.19[III]	0.575[III]
	Rear	47.77	527.05[V]	-514.19[V]	432.6[II]	-393.1[V]	65.75[IV]	13.27[III]	0.749[III]
3)	**Front**	12.4	136.09[I]	-165.28[II]	164.75[II]	-149.97[I]	22.06[I]	0.778[III]	0.291[III]
	Rear	27.64	495.74[I]	-335.03[I]	336.92[V]	-356.51[II]	53.5[II]	3.28[III]	0.676[III]
4)	**Front**	42.35	401.25[V]	-379.76[I]	373.19[II]	-359.74[I]	50.17[IV]	7.55[III]	0.781[III]
	Rear	34.58	934.44[II]	-704.7[V]	740.27[I]	-630.88[V]	77.16[I]	12.43[III]	0.789[III]
5)	**Front**	18.58	163.87[V]	-186.21[V]	149.65[V]	-193.9[I]	20.94[V]	1.79[III]	0.287[III]
	Rear	19.79	316.91[V]	-302.09[V]	247.78[IV]	-221.06[II]	37.64[IV]	2.89[III]	0.407[III]

The results seen in Table 5-3 show that the initial lay-up is not suitable for the Mamba EV chassis due to failure predicted by the failure indices, as well as by ply strength being exceeded in the plies. Based on the material properties for the carbon fibre 2/2 twill weave with epoxy matrix, shown in Appendix A, Table A-1, the tensile strength, compressive strength, and shear strength values for a ply are 464.4 MPa, 286.6 MPa, and 53.4 MPa respectively. It can be seen that the peak stress in several simulations exceeds the tensile and compressive strength of the material, indicating regions that needed to be modified.

Several regions of high stress were common to several load cases. The mesh density in these regions was checked by analysing the stress contour gradient in the elements surrounding the element exhibiting the peak stress, where a high gradient indicates a large decrease in stress over a short distance. If the elements surrounding the peak stress element have widely varying results, the mesh density may be too large. Stressed regions were also analysed by checking the nodal averaging plot during the post processing. This plot averages the gauss points of elements surrounding a node to obtain an average stress at the node. Large variations between the results indicated with nodal averaging turned off and turned on could indicate that the region requires a finer mesh. The areas of focus for the refinement were the edge of the air ducts on the rear suspension mounting panels, and the suspension mount panels themselves, graphically indicated in Figures 5-7 and 5-8.

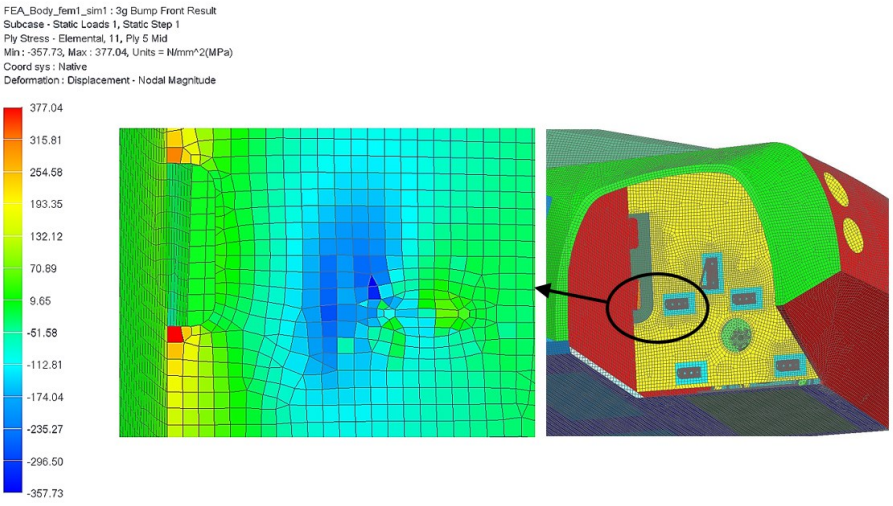

Figure 5-7. Peak σ_{11t} in the 5th ply of the rear suspension mount panel in the 3G bump load case

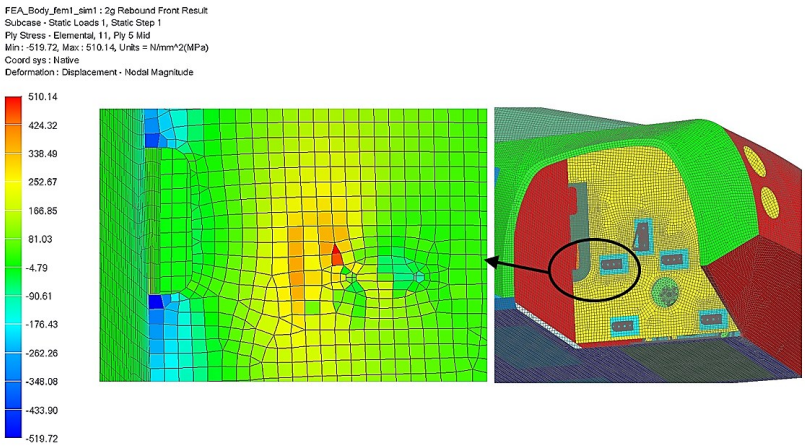

Figure 5-8. Peak σ_{11c} in the 5th ply of the rear suspension mount panel in the 2G rebound load case.

With regards to the failure indices, all the simulations show that bond failure would be unlikely, however, based on the ply failure index, one can see that the majority of the simulations predict failure. The peak ply failure index was shown to be in the region of the rear hardpoint for the suspension arms, illustrated in Figure 5-9. This indicated that marine ply was probably not suitable as a hardpoint material.

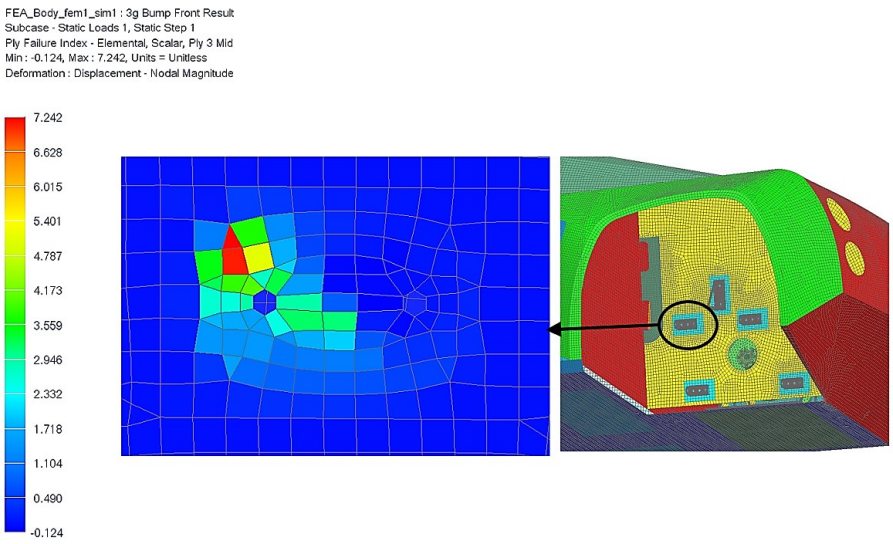

Figure 5-9. Ply failure in the rear suspension arm hardpoint for the 3G bump load case.

5.8.4 Localised Load Cases

The localised load cases focused on the response of the mounting points for the steering column, hand brake and brake pedal, ensuring that they had sufficient strength to survive peak loading. The worst-case results of the local load cases based on the initial anticipated lay-up can be seen in Table 5-4.

Table 5-4. Initial results for the localised load cases.

	Deflection [mm]	Peak Ply Stress [MPa]					Ply Failure Index	Bond Failure Index
		σ_{11t}	σ_{11c}	σ_{22t}	σ_{22c}	σ_{12}		
Steering Column	45.24	2077.18 [IV]	-2076.43 [I]	1890.01 [IV]	-1859.45 [I]	231.21[IV]	36.87[I]	3.04[II]
Handbrake	5.68	230.93[I]	-265.09[I]	249.03[I]	-257.59[I]	41.99[I]	1.417[I]	0.467[II]
Brake Pedal	0.871	106.92[II]	-80.87[IV]	134.68[I]	-103.46[IV]	17.44[II]	0.263[V]	0.126[III]

The results for the steering column mount load case show excessive deflection in the cross braces and bowing in the longitudinal supports, seen in Figure 5-10. The high deflection and stress indicated that the steering column support required stiffening by using a core material within the sandwich structure.

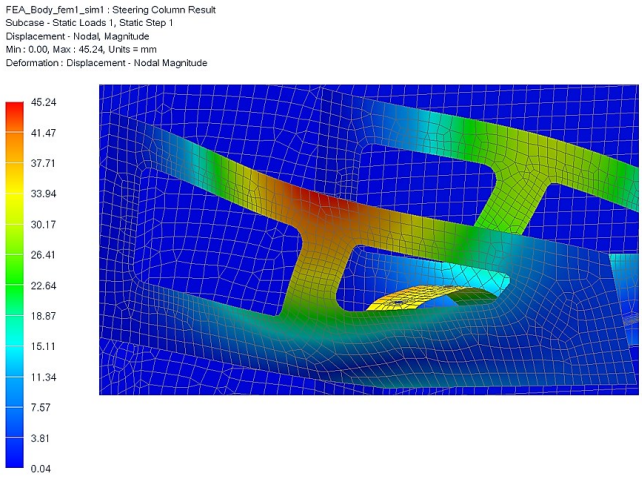

Figure 5-10. Deflection in the steering column mount.

The results for the handbrake mount predicts ply failure in the mount as well as relatively high deflection, seen in Figure 5-11. High deflection in the handbrake, even on a mount that can survive expected loading, would reduce the passenger's perception of quality, which is key in marketing the vehicle. This indicated that the handbrake mount also required a core material within the lay-up.

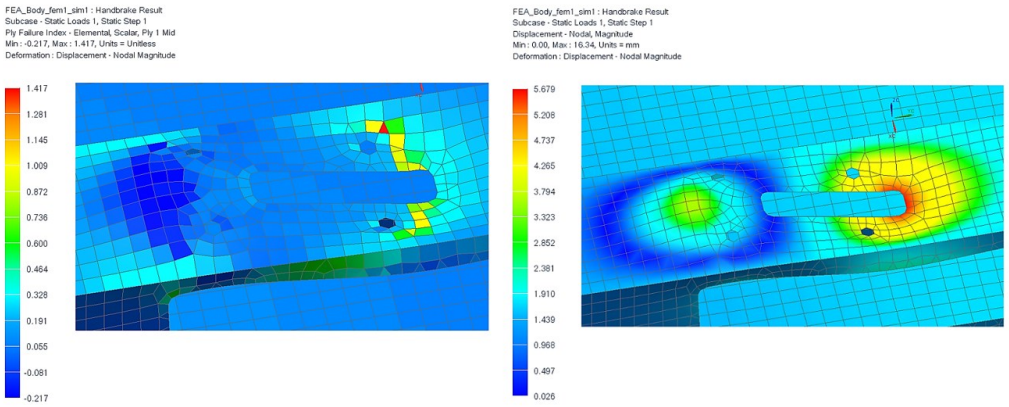

Figure 5-11. Initial handbrake load case: a) ply failure plot, b) deflection plot.

The results of the brake pedal simulation predict good survivability of the mount, with low peak stresses. The peak stress occurs in the region between the mounting holes for the master cylinder and the hole for the master cylinder plunger, which, based on the stress plot seen in Figure 5-12, requires mesh refinement around the hole edges.

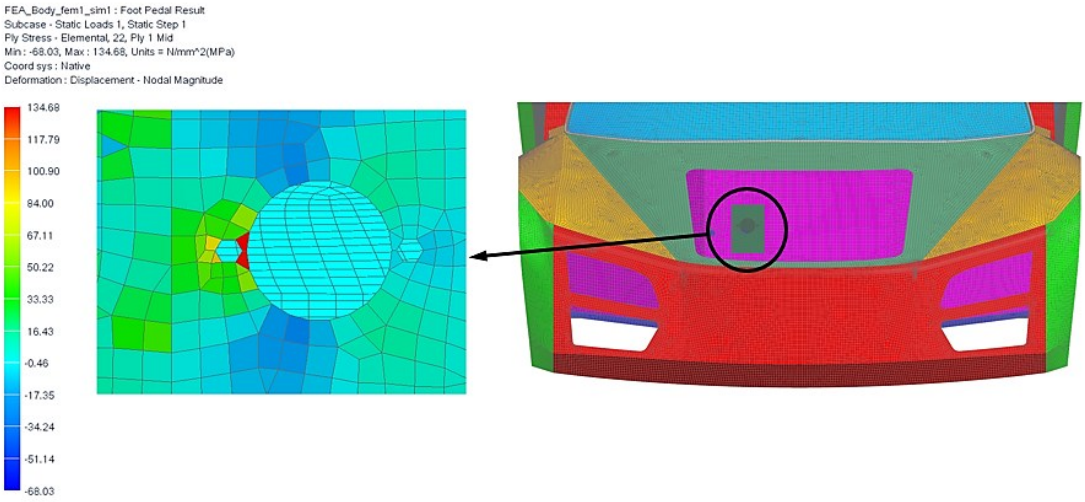

Figure 5-12. Peak stress in the master cylinder mount.

5.8.5 Roof Load Case

The roof load case was carried out as a static test to simulate the roof structure during a roll, it must withstand a roll. Crash testing was not a priority for the prototype as it was to be used as a testing platform for future iterations of the Mamba EV. The worst-case results of the initial roof loading simulation are shown in Table 5-5.

Table 5-5. Roof load case initial results.

Deflection [mm]	Peak Ply Stress [MPa]					Ply Failure Index	Bond Failure Index
	σ_{11t}	σ_{11c}	σ_{22t}	σ_{22c}	σ_{12}		
67.46	810.48[I]	-984.76[I]	493.74[IV]	-948.52[II]	132.15[I]	10.99[I]	1.96[III]

Based on the results it can be seen that there is a large degree of deflection along the roof edges, as well as along the top edge of the rear window, shown in Figure 5-13. This indicated that stiffening was required along these regions.

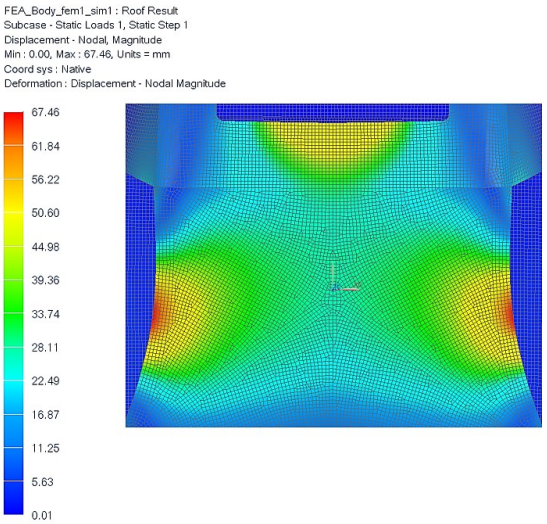

Figure 5-13. Initial roof load case deflection of the roof structure.

The peak stresses in the roof panel far exceed the laminate strength of the carbon composite, with stress concentrations forming in the region where the top of the roof structure joined the sides of the rear roof section, shown in Figure 5-14, as well as mid-way along the arch above the door cut-outs, seen in Figure 5-15. Refinement to the structure was needed to alleviate the stress concentration in the corner, as well a finer mesh to more accurately observe the response of the structure in this region. The region of peak ply failure coincided with the peak stress, while peak bond failure was observed on a skewed element on the top of the A-pillar, which required mesh refinement.

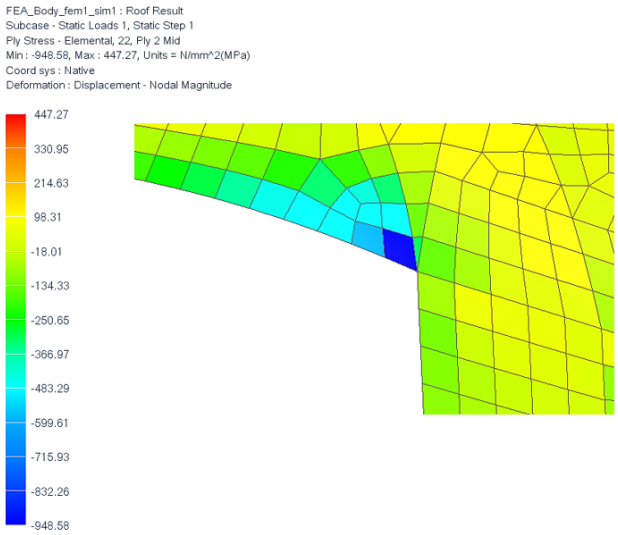

Figure 5-14. Initial roof load case peak compressive stress in the 22 direction.

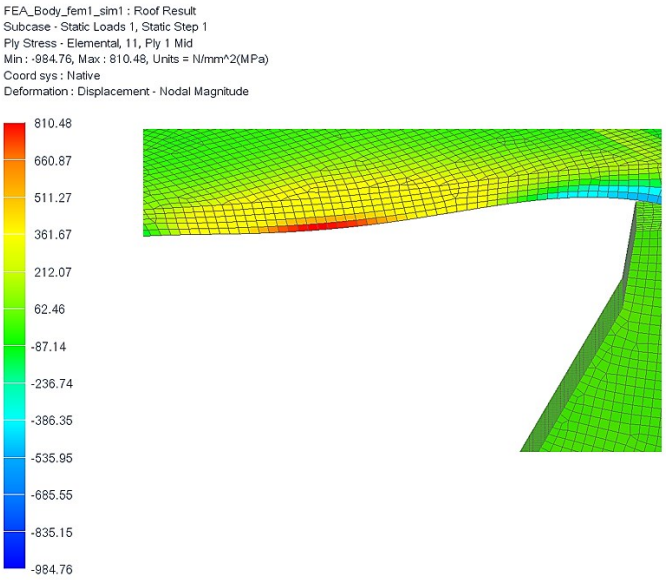

Figure 5-15. Initial roof load case peak tensile stress in the 11 direction.

5.9 Chapter Conclusion

The current chapter has detailed the discretisation process of the Mamba EV chassis. The definition of all materials used has been described, with an emphasis on the procedure of defining a composite material. The failure theory used for the study has been implemented. The chapter detailed all loading conditions and constraints for the load-case simulations that the chassis structure was subjected to; with the results of the simulations based on the initial anticipated composite lay-up being attained.

CHAPTER 6

Design Refinement & Final Results

Chapter 6 outlines the chassis geometry and mesh refinements required based on the results of the initial simulations. The final composite ply stacking configurations and final results are then presented, indicating good survivability of the chassis under all the loading conditions.

6.1 Refinement

The results presented in section 5.8 highlighted structural weaknesses and the areas that experience peak stress within the chassis. The approach taken in adjusting the model was to first ensure a good mesh density in regions of high stress, by locally refining the areas highlighted in the initial results. The load case simulations were then re-run using the refined mesh model. After the mesh was considered satisfactory, the stressed panels' composite lay-ups were adjusted until survivability of the chassis subject to the applied loading was indicated.

6.1.1 Mesh Refinement

Mesh refinement in local regions of particularly high stress increase the accuracy of the results without drastically increasing the solve time of the simulations, assuming that there are no singularities present. Refinement was achieved by surface splitting in conjunction with the *mesh control* tool in the .fem file. Splitting the surface allowed the author to define different mesh sizes on the same structural panel, while the *mesh control* tool assisted in developing a smooth transition between mesh densities, as well as improving the mesh quality within the refined regions. After refinement, the mesh was then checked using the *element quality* tool in the .fem file to ensure there were no meshing errors.

Based on the results, for the initial loading simulations, the regions of peak stress were the motor controller air inlet ducts on the rear suspension mounting panels, the hardpoints in the suspension mounting panels, and the corner of the roof structure where the top of the roof connects to the sides of the rear roof section. The cut outs for the brake master cylinder required mesh refinement due to the presence of skewed elements between the mounting holes.

For the motor controller air ducts, a smaller region was split from the rear suspension mounting panels, which was then meshed using a finer mesh of 6 mm. In order to smooth the transition between the different mesh densities, the *mesh control* tool was used. An edge density of 6 mm was applied around the boundary of the air duct region too. Since the suspension mounting

brackets were being glued to the hardpoints in the .sim file, the holes were supressed in order to avoid artificial stress spikes in the results at the hole edges. Comparing the meshes of the rear suspension mount panel before and after refinement, seen in Figure 6-1, it can be seen that there are fewer split QUAD elements along the cut out edge of the air duct and a reduction in skewness to the elements on the hardpoint after the suppression of the mounting holes.

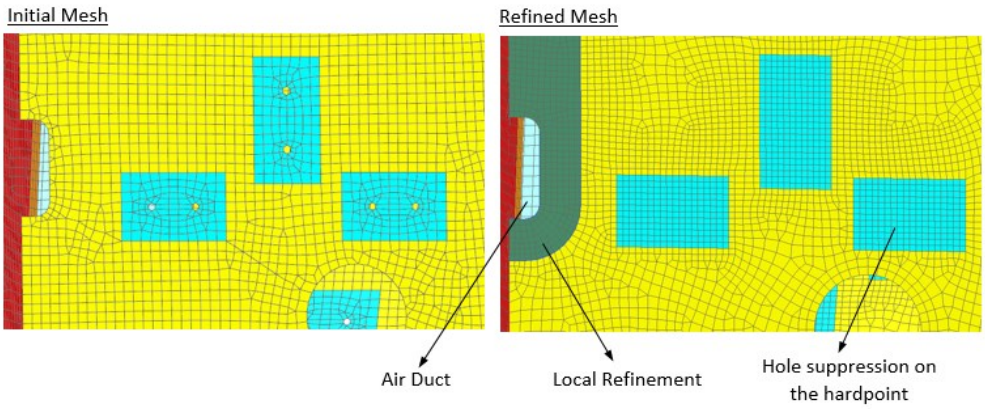

Figure 6-1. Motor controller air duct mesh refinement comparison.

The third area of mesh refinement was the cut-out and mounting holes for the brake master cylinder. Mesh distortion occurred between the central plunger hole and the bolt holes. Since the bolts themselves were not articles of interest in the simulation, the brake pedal mounting had been connected by gluing the pedal mount to the master cylinder hardpoint. Therefore, in order to improve the mesh quality, the bolt holes were removed and the plunger hole was refined using the mapped hole density type in the *mesh control* tool. The comparison of the initial mesh and refined mesh for the master cylinder can be seen in Figure 6-2.

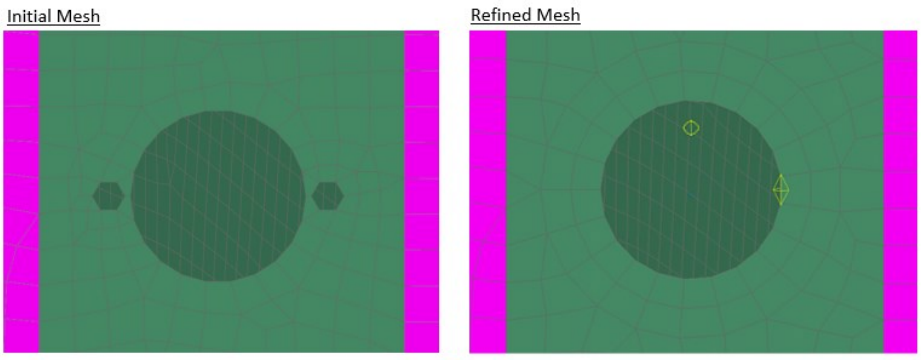

Figure 6-2. Master cylinder plunger cut out.

For the roof corner refinement, the geometry was adjusted where the upper roof joined the rear roof sides. A fillet was added to reduce the stress concentration, seen in Figure 6-3(a), which was then meshed and refined, shown in Figure 6-3(b).

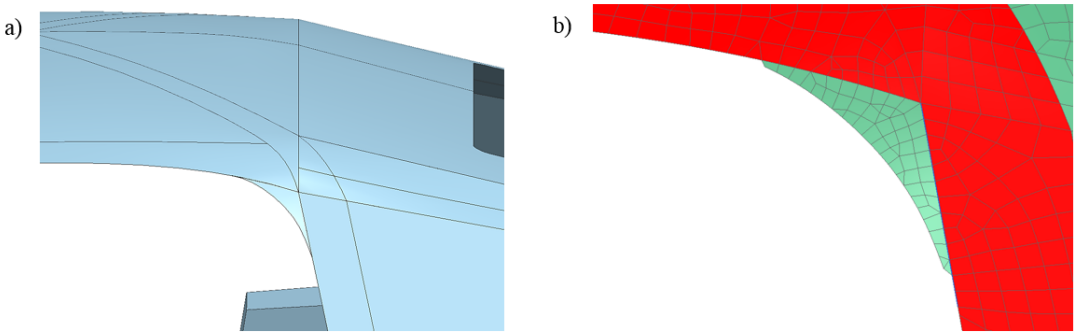

Figure 6-3. Roof refinement: a) structural adjustment, b) mesh.

6.1.1.1 Mesh Refinement Results

The load cases were rerun using the refined mesh model in order to compare the results against the initial results. The focus of the comparison was not only the peak values of the parameters monitored, but the distribution of the stress in the peak stressed regions as well. This was done by analysing the colour contours of the stress load plot, ensuring there were no outlying anomalies, and by monitoring the colour gradient across the stressed region. The peak results of the mesh refined simulations can be seen in Table 6-1 to Table 6-4.

Table 6-1. Motor induced load case: mesh refined results.

Deflection [mm]	Peak Ply Stress [MPa]					Ply Failure	Bond Failure
	σ_{11t}	σ_{11c}	σ_{22t}	σ_{22c}	σ_{12}		
2.26	46.41[V]	-63[IV]	45.9[I]	-92.83[V]	14.76[IV]	0.279[III]	0.374[III]

Table 6-2. Operational load cases: mesh refined results.

		Deflection [mm]	Peak Ply Stress [MPa]					Ply Failure	Bond Failure
			σ_{11t}	σ_{11c}	σ_{22t}	σ_{22c}	σ_{12}		
1)	Front	39.85	495.01[V]	-420.57[I]	260.13[V]	-377.51[V]	64.14[IV]	9.57[III]	0.689[III]
	Rear	33.95	460[I]	-525.3[V]	440.41[I]	-400.16[IV]	67.17[IV]	11.15[III]	0.814[III]
2)	Front	54.78	548.95[I]	-640.28[V]	398.6[IV]	-420.13[V]	81.95[IV]	15.05[III]	0.713[III]
	Rear	47.78	640.78[V]	-613.04[V]	544.36[V]	-526.78[IV]	82[IV]	17.85[III]	0.92[III]
3)	Front	12.47	151.79[II]	-164.7[II]	132.48[IV]	-146.04[I]	21.99[I]	0.855[III]	0.574[III]
	Rear	27.48	460.95[I]	-389.86[I]	332.04[IV]	-426.97[II]	49.19[II]	2.82[III]	2.17[III]
4)	Front	40.3	458.76[V]	-410.39[I]	431.49[II]	-375.61[IV]	58.8[IV]	8.27[III]	0.65[III]
	Rear	33.91	611.97[I]	-616.58[V]	874.29[II]	-732.6[IV]	81.43[I]	14.75[III]	1.36[III]
5)	Front	18.68	201.38[V]	-195.78[II]	168.49[V]	-190.13[I]	25.76[IV]	2.19[III]	0.298[III]
	Rear	19.78	320.88[V]	-374.51[V]	279.38[I]	-255.89[IV]	47.89[IV]	3.59[III]	0.343[III]

Table 6-3. Localised load cases: mesh refined results.

	Deflection [mm]	Peak Ply Stress [MPa]					Ply Failure	Bond Failure
		σ_{11t}	σ_{11c}	σ_{22t}	σ_{22c}	σ_{12}		
Steering Column	68.96	3880.9 [I]	-3881.87 [IV]	2428.52[IV]	-2329.44 [I]	304.66 [IV]	111.04 [IV]	4.73[II]
Handbrake	5.05	277.38 [IV]	-288.19 [IV]	304.92 [IV]	-308.05 [IV]	46.48 [IV]	1.65[IV]	0.81[II]
Brake Pedal	0.924	95.78[II]	-99.87[IV]	119.01 [II]	-85.68 [IV]	20.02[I]	0.255[V]	0.136 [III]

Table 6-4. Roof load case: mesh refined results.

Deflection [mm]	Peak Ply Stress [MPa]					Ply Failure	Bond Failure
	σ_{11t}	σ_{11c}	σ_{22t}	σ_{22c}	σ_{12}		
65.85	812.46[I]	-843.11[I]	483.81[IV]	-532.55[V]	107.09[II]	7.439[I]	10.95[III]

Comparing the results in Table 5-2 to Table 5-5 with the results in Table 6-1 to Table 6-4 it can be seen that the peak stress values increased in the observed parameters. Variation in the results was expected as the local mesh densities in these critical regions were increased. The peak results for the 3G bump and 2G rebound load cases can be seen in Figure 6-4 and Figure 6-5 respectively.

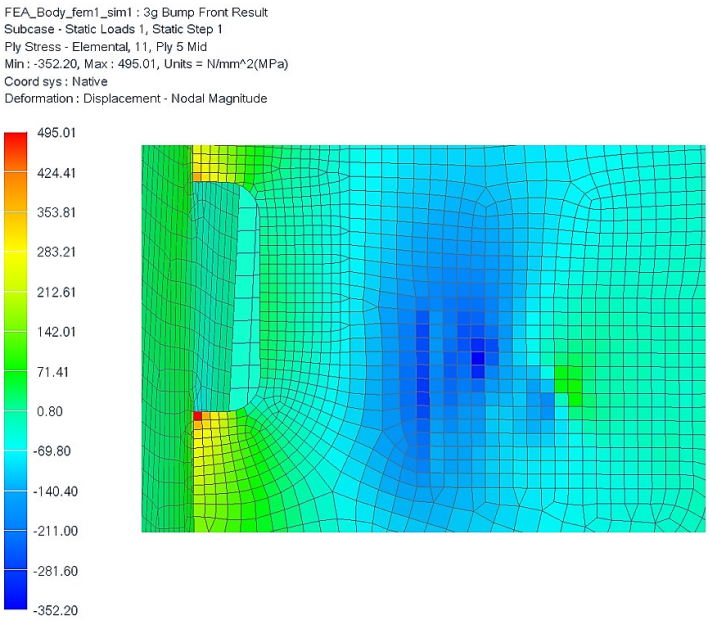

Figure 6-4. Peak σ_{11t} in the 5th ply of the rear suspension mount panel for the refined mesh model 3G bump load case.

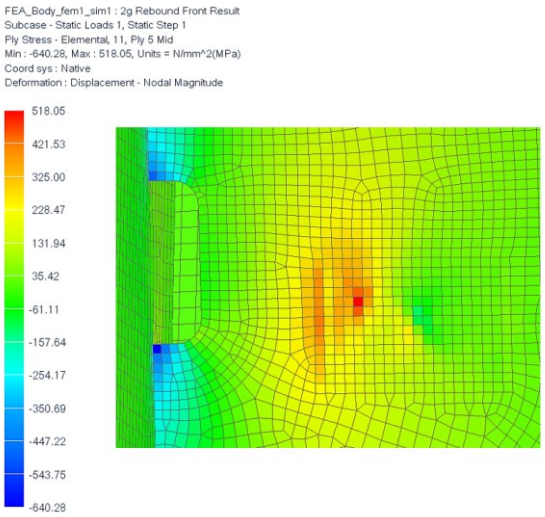

Figure 6-5. Peak σ_{11c} in the 5th ply of the rear suspension mount panel for the refined mesh model 2G rebound load case.

For the roof, the stress concentration was removed by adding the fillet to the corner of the joins between the upper roof and the rear sides. Figure 6-6 shows the peak compressive stress distribution across the fillet.

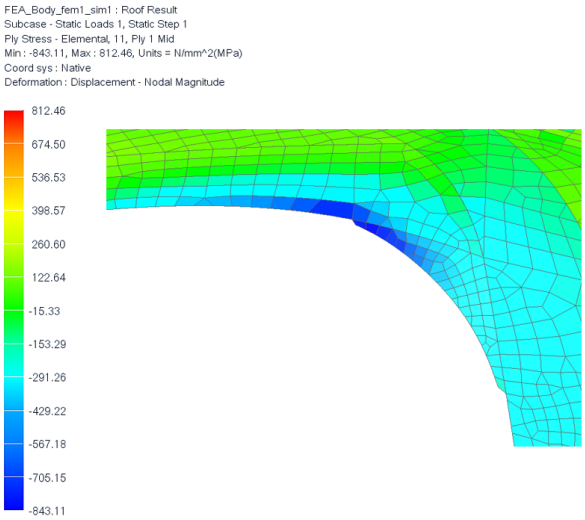

Figure 6-6. Roof refinement peak compressive stress plot.

The last region of mesh refinement was that in the hardpoint for the brake pedal, a stress region on the front firewall. As seen in Figure 6-7, the removal of the bolt holes combined with the mapped hole mesh control around the edge improved the quality of the mesh and eliminated skewed elements.

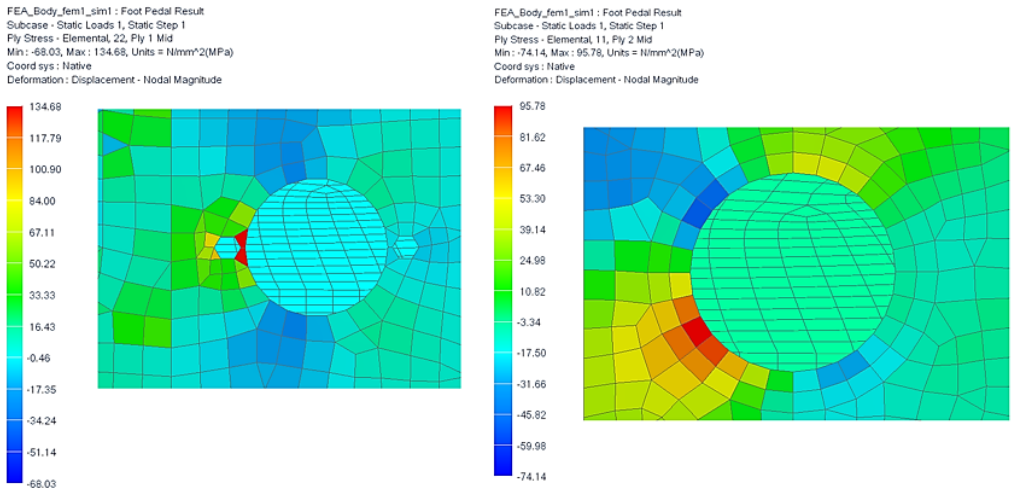

Figure 6-7. Mesh refinement for the master cylinder cut-out in the front firewall.

6.1.2 Composite Lay-up Adjustment

Looking at the results of the simulations based on the refined mesh model, it was decided to start the composite lay-up refinement by first ensuring survivability of the general chassis under the operational loads, after which the local regions' composite lay-ups would be adjusted. Based on the peak stress results seen in Table 6-2, it can be seen that the stresses experienced in the pothole braking simulation were the most severe, therefore refinements for this load case were undertaken first. Subsequent load cases were then analysed using the adjusted composite lay-up based on the pothole braking results. Since a safety factor had already been imposed on the operational loads, structural survivability was predicted once all the monitored parameters were indicated to be below their required limits.

The refinement of the composite laminate was an iterative process of adjusting the stacking configuration of the panel being analysed, running the load case with the new configuration, and comparing the results with those of the previously simulated models. As stated above, the pothole braking load case was adjusted first. Based on the results shown in section 6.1.1.1, the regions requiring strengthening were the suspension mounting panels and the hardpoints for the suspension arm mounts. The iterative approach taken for the composite adjustment was to first replace the hardpoints with a stronger material, rerun the simulations for both the front and rear pothole braking load cases, and then, based on the results, strengthen the mounting panel by adding carbon fibre plies. With failure in the rear suspension mount hardpoint being predicted, the marine ply core was replaced with aluminium 6061, with the results shown in Table 6-5.

Table 6-5. Pothole braking load case: first iteration of the composite laminate adjustment.

	Deflection [mm]	Peak Ply Stress [MPa]					Ply Failure	Bond Failure
		σ_{11t}	σ_{11c}	σ_{22t}	σ_{22c}	σ_{12}		
Front	36.58	451.58[V]	-418.78[V]	344.15[II]	-313.25[II]	57.74[IV]	1.92[I]	0.345[III]
Rear	29.94	451.7[V]	-428.12[I]	441.18[I]	-466.02[V]	57.78[IV]	2.13[V]	0.394[III]

Comparing the results to Table 6-2 load case 4, the peak deflection, stresses and ply failure index decreased after the marine ply hardpoints were replaced with aluminium. For the front wheel loaded model, peak tensile stresses fell just below the tensile strength of the material, however the compressive stresses still indicated failure in the second and fifth ply, and the peak shear stress indicated failure in the fourth ply. The peak ply failure index value had shifted from the hardpoint itself to the first ply of the rear suspension mount panel. For the rear wheel loaded model, peak tensile stresses also fell just below the tensile strength of the material, however the compressive stresses still indicated failure in the first and fifth ply. The shear strength of the material was also exceeded in the fourth ply. The peak ply failure index value had shifted from the hardpoint to the fifth ply of the rear suspension mount panel. For the suspension mount panels, the ply reference numbering started at one on the outer most ply, increasing with each consecutive ply inwards.

The approach taken for increasing the number of carbon plies in a laminate lay-up was to analyse the results of the prior iteration, and then add a ply to the same side of the core that any failed ply is situated. Since failure was still predicted in the first, second, fourth and fifth plies on the rear suspension mounting panel, a carbon fibre ply was added to both sides of the core. The model was then rerun, with the results shown in Table 6-6.

Table 6-6. Pothole braking load case: second iteration of the composite laminate adjustment.

	Deflection [mm]	Peak Ply Stress [MPa]					Ply Failure	Bond Failure
		σ_{11t}	σ_{11c}	σ_{22t}	σ_{22c}	σ_{12}		
Front	31.4	291.8[I]	-330.29[II]	339.67[II]	-303.58[I]	43.32[I]	1.4[II]	0.344[III]
Rear	27.27	274.17[VII]	-262.22[I]	388.79[V]	-311.46[VII]	41.87[I]	1.15[VII]	0.374 [III]

After adding an extra ply to each side of the core on the rear suspension mounting panel there was an improvement to all the monitored parameters. For the front wheel loaded model, the peak compressive strength of the material was exceeded in the first ply on the front suspension mount panel, and the second ply of the rear roof structure, around the rear windscreen. The peak ply failure index value, while reducing in magnitude, shifted from the rear suspension mount panel to the upper corner of the rear windscreen cut-out. For the rear wheel loaded model, compressive strength was exceeded, and ply failure was predicted on the seventh ply of the rear suspension mount panel.

For the next iteration, a carbon fibre ply was added to the outer surface of the front suspension mount panels, the inner surface of the rear suspension mount panel, and the rear roof structure panel, the results of which are shown in Table 6-7.

Table 6-7. Pothole braking load case: third iteration of the composite laminate adjustment.

	Deflection [mm]	Peak Ply Stress [MPa]					Ply Failure	Bond Failure
		σ_{11t}	σ_{11c}	σ_{22t}	σ_{22c}	σ_{12}		
Front	28.99	235.13[I]	-283.67[II]	292.52[II]	-209.32[I]	41.33[I]	1.09[II]	0.483[III]
Rear	25.19	224.35[I]	-246.74[I]	375.59[V]	-260.49[V]	40.4[IV]	0.92[VIII]	0.435[IV]

After the third iteration, the last parameter indicating failure was the ply failure criteria. Failure was indicated in the second ply of the rear roof structure, in the upper corner of the rear windscreen cut-out. Another carbon fibre ply was added to the inner surface for the third iteration, the results of which are shown in Table 6-8.

Table 6-8. Pothole braking load case: fourth iteration of the composite laminate adjustment.

	Deflection [mm]	Peak Ply Stress [MPa]					Ply Failure	Bond Failure
		σ_{11t}	σ_{11c}	σ_{22t}	σ_{22c}	σ_{12}		
Front	28.51	234.81[I]	-250.36[II]	267.78[VI]	-209.19[I]	35.7[I]	1.09[III]	0.483[III]
Rear	24.76	224.96[I]	-246.44[I]	375.29[V]	-260.6[V]	40.35[IV]	0.921[VIII]	0.435[IV]

After the fourth iteration, the element indicating ply failure had shifted from the rear roof structure to the corner of the core ply in the motor controller hardpoint. This failure indicated that marine plywood was not a suitable core material, and therefore for the fifth iteration, the motor controller hardpoint material was replaced with aluminium. The results of the fifth iteration of the pothole braking load cases can be seen in Table 6-9.

Table 6-9. Pothole braking load case fifth iteration of the composite laminate adjustment.

	Deflection [mm]	Peak Ply Stress [MPa]					Ply Failure	Bond Failure
		σ_{11t}	σ_{11c}	σ_{22t}	σ_{22c}	σ_{12}		
Front	27.61	233.28[I]	-262.63[I]	267.51[VI]	-209.01[I]	36.25[I]	0.907[II]	0.483[III]
Rear	24.45	234.94[I]	-267.53[I]	376.61[V]	-260.24[V]	40.42[IV]	0.922[VIII]	0.436[IV]

Based on the results of the fifth iteration it can be seen that survivability of the chassis, under pothole braking load conditions, was predicted. The next step in the adjustment of the chassis composite lay-up was to re-evaluate the response of the chassis under the remaining load cases, then, following the same procedure used for refining the lay-up under pothole braking loading conditions, adjust the composite lay-up until survivability was predicted for all loading conditions.

6.1.2.1 Final Composite Lay-up

Once survivability had been predicted, the prototype chassis composite lay-up had been finalised. The regions shown in Figure 4-11 and Figure 4-12 coincided with the collectors in the .fem file, and therefore the panels within the region share the same composite stacking configuration. Table 6-10 shows the final stacking configurations for each of the regions of the chassis, with Table 6-11 showing the stacking configurations for the mounting hardpoints within several of the regions. Each ply in the stacking configuration is denoted by its ply angle, with the cores being denoted by the core thickness followed by the material used. The abbreviations Ar, PVC, Ply, and Al, refer to aramid fibre, PVC core, marine plywood core, and aluminium 6061 core respectively.

Table 6-10. Stacking configurations for the regions of the Mamba EV.

Region	Lay-up
A-Pillar	[0;45;90;45;0;45;10mmPVC;45;0;45;90;45;0]
Base	[0Ar;45Ar;0;45;20mmPVC;45;0]
Bonnet	[0;45;3mmPVC;45;0]
Centre Channel	[0;45;0;45;0;45]
Dash	[0;45;3mmPVC;45;0]
Front Bumper	[0;45;45;0]
Front Firewall	[0;45;10mmPVC;45;0]
Front Suspension Mount	[0;45;90;10mmPVC;45;0]
Front Upper Sides	[0;45;45;0]
Front Wheel Arch	[0;45;45;0]
Inner Sides	[0;45;3mmPVC;45;0]
Outer Sides	[0;45;3mmPVC;45;0]
Rear Bumper	[0;45;45;0]
Rear Firewall	[0;45;90;10mmPVC;45;0]
Rear Roof Sides	[0;45;3mmPVC;45;0]
Rear Suspension Mount	[0;45;90;45;0;10mmPVC;45;0;45;90]
Rear Upper Sides	[0;45;45;0]
Rear Wheel Arch	[0;45;45;0]
Rear Windscreen	[0;45;90;45;6mmPVC;45;90;45;0]
Roof	[0;45;6mmPVC;45;0]
Roof Support	[0;45;90;45;0;10mmPVC;0;45;90;45;0;45;90;45;0;45]
Steering Column Support	[0;45;3mmPVC;45;0]
Tub Sills	[0;45;3mmPVC;45;0]

Table 6-11. Stacking configurations for mounting hardpoints in the Mamba EV.

Region	Layup
Column U-Bolt	[0;45;90;10mm;90;45;0]
Controller	[0;45;10mmAl;45;0]
Front Suspension Mount	[0;45;90;10mmAl;45;0]
Handbrake Mount	[0;45;90;5mmPly;45;0;45]
Master Cylinder	[0;45;10mmAl;45;0]
Motor Mount	[0Ar;45Ar;0;45;20mmPly;45;0]
Rear Suspension Mount	[0;45;90;45;0;10mmAl;45;0;45;90]

6.2 Final Results

Based on the final chassis lay-up shown in Table 6-10 and Table 6-11, the final results of the monitored parameters for the chassis under the operational and local load cases are shown in Table 6-12 to Table 6-15, predicting the survivability of the structure.

Table 6-12. Motor induced load case: mesh final results.

Deflection [mm]	Peak Ply Stress [MPa]					Ply Failure	Bond Failure
	σ_{11t}	σ_{11c}	σ_{22t}	σ_{22c}	σ_{12}		
1.72	44.36[VI]	-62.63[VI]	42.68[VI]	-76.56[V]	13.99[VI]	0.435[IV]	0.282[III]

Table 6-13. Operational load cases: mesh final results.

		Deflection [mm]	Peak Ply Stress [MPa]					Ply Failure	Bond Failure
			σ_{11t}	σ_{11c}	σ_{22t}	σ_{22c}	σ_{12}		
1)	**Front**	21.1	246.66[V]	-178.82[II]	273.23[VI]	-202.69[I]	24.21[XI]	0.62[I]	0.377[V]
	Rear	19.87	197.95[VI]	-191.23[X]	167.8[VI]	-180.43 [I]	28.17[XI]	0.55[X]	0.691[V]
2)	**Front**	28.82	226.58[VI]	-233.55[X]	192.12[II]	-228.29[II]	34.39[XI]	0.746[II]	0.447 [V]
	Rear	28.52	250.4[V]	-243.11[II]	283.62[VI]	-219.93[I]	34.26[XI]	0.822[II]	0.589[V]
3)	**Front**	8.29	100.2[V]	-101.84[II]	110.24[VI]	-86.49[I]	13.29[I]	0.423[IV]	0.256[III]
	Rear	21.61	367.02[I]	-213.83[I]	282.65[V]	-203.4[I]	44.43[V]	0.676[VI]	0.577[III]
4)	**Front**	20.89	229.31[VI]	-206.81[I]	265.36[VI]	-207.68[I]	26.14[V]	0.722[II]	0.484[III]
	Rear	20.25	216.72[II]	-194.62[VI]	334.22[V]	-228.81[V]	36.06[IV]	0.698[V]	0.686[VI]
5)	**Front**	9.65	156.42[V]	-105.88[II]	166.11[VI]	-119.17[I]	13.67[V]	0.358[IV]	0.247[III]
	Rear	11.4	131.01[VI]	-138.09[X]	114.9[II]	-122.17[II]	20.29[XI]	0.523[IV]	0.557[VI]

Table 6-14. Localised load cases: mesh final results.

	Deflection [mm]	Peak Ply Stress [MPa]					Ply Failure	Bond Failure
		σ_{11t}	σ_{11c}	σ_{22t}	σ_{22c}	σ_{12}		
Steering Column	4.07	124.09[VII]	-136.12[I]	132.02[VI]	-102.62[II]	14.14[VII]	0.405[IV]	0.381[IV]
Handbrake	1.45	78.02[I]	-88.83[VI]	63.84[VII]	-67.75[II]	12.99[VII]	0.659[IV]	0.224[III]
Brake Pedal	0.841	86.06[II]	-96[IV]	88.91[I]	-81.05[IV]	9.39[III]	0.243[V]	0.125[III]

Table 6-15. Roof load case: mesh final results.

Deflection [mm]	Peak Ply Stress [MPa]					Ply Failure	Bond Failure
	σ_{11t}	σ_{11c}	σ_{22t}	σ_{22c}	σ_{12}		
17.6	295.28[IV]	-257.65[I]	173.31[IV]	-224.86[II]	41.17[V]	0.906[I]	0.625[VI]

6.2.1 Torsional Stiffness

Once the survivability of the chassis was predicted an updated chassis torsional stiffness was determined. Using the averaged deflection of 1.613 mm, a torsional stiffness of 12335.81 Nm/° was calculated, as seen in Appendix B, using equation (B.27). The final chassis torsional stiffness showed a 49.3% increase in stiffness in comparison to the initial calculation before layup adjustment.

6.3 Chapter Conclusion

The refinement to the model meshing as well as the iterative composite lay-up design process has been outlined, and the results of the ensuing analysis detailed. The final composite ply stacking configurations for all model collectors have been determined, with the final results of the loading simulations predicting the survivability of the chassis under all expected loading scenarios.

CHAPTER 7

Manufacture

Chapter 7 details the manufacture of the Mamba EV chassis using high density foam moulds, as well as offering insight into the powertrain and assembly of the complete vehicle.

7.1 Moulding

The starting point for the chassis manufacture was the preparation and development of the tooling required to produce the desired geometry. The chassis structure was split into two sections, flat panels and complex curvature, which had drastically different manufacturing procedures and complexity. The lay-up of the flat panels required no tooling, only a flat surface on which the panels could be produced before being cut to shape. Since the outer structure of the chassis comprised of complex curvature, tooling was required for its manufacture. The outer structure was manufactured in sections due to lay-up time limitations, as well as ease of tooling manufacture. The use of epoxy resin meant that the laminate had to be laid-up within a relatively short time frame, before it began to cure. Figure 7-1 shows the separate sections manufactured (Sim et al., 2016).

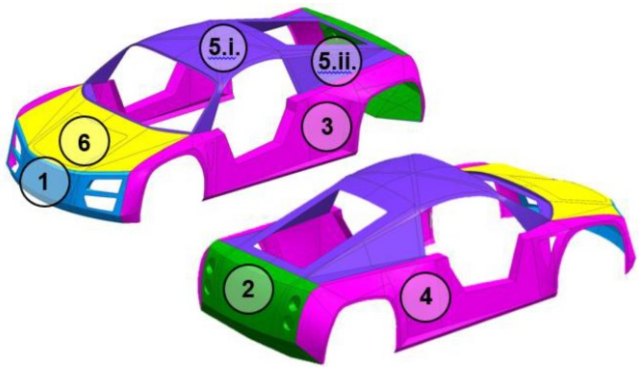

Figure 7-1. Outer body sections manufactured (Sim et al., 2016).

It was decided to manufacture the tooling out of high density polyurethane foam since it was cost effective, produced a good surface finish, and could be produced in a relatively short period of time, which suited the time pressured nature of the project. The high density foam mould was produced by stacking and gluing foam blocks, and then using a CNC mill to cut the desired geometry, forming a negative of the desired component, as seen in the case of the roof panel shown in Figure 7-2. Once the geometry of the mould had been cut, the mould underwent a hand finishing process. The mould was hand sanded to remove the ridges left by the cutting bits during

milling, followed by three coats of sealer. The mould was then body filled to seal any remaining pin holes.

Lastly, the mould was painted with two coats of primer and finished with light sanding using water paper to produce a smooth finish (Sim et al., 2016). Figure 7-3 shows the final hand finished mould for the front bumper panel.

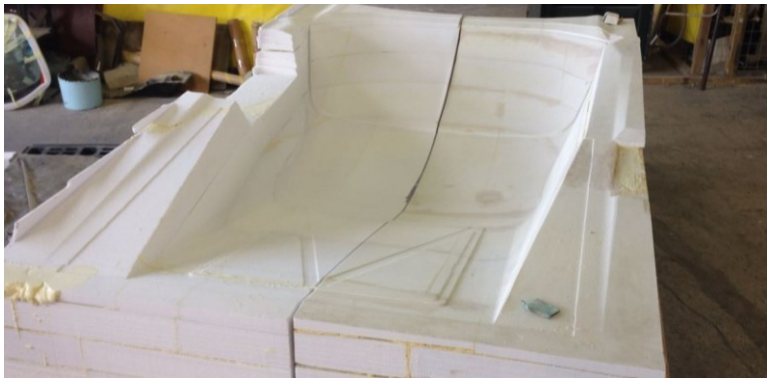

Figure 7-2. High density foam mould for the manufacture roof panel.

Figure 7-3. Hand finished and sealed mould for the front bumper panel.

7.2 Composite Lay-up and Assembly

The composite lay-up of the chassis components was split into two sections, the lay-up of the flat panels, which was completed at the Durban University of Technology Composites Research Laboratory, and the manufacture of the outer chassis structure, which was completed at Stealth Performance Products CC. Both sets of composite laminates were manufactured using the out-of-autoclave, hand lay-up, vacuum bagging process. Once the carbon fibre panels were removed from the mould, the excess material that overlapped the components edges had to be trimmed. Figure 7-4 shows the roof panel once it had been removed from the mould.

After the manufacture of the individual composite sections, the chassis needed to be assembled. The assembly process started with the inner flat structure, which was aligned using jigs, and then bonding on the outer structure (Sim et al., 2016), as seen in Figure 7-5.

Figure 7-4. Roof panel of the Mamba EV chassis.

Figure 7-5. Jigs used in assembly of the flat panel inner structure, with bonded side panels.

7.3 Electric Powertrain

The electric powertrain of the Mamba EV comprised two 60 kW, liquid cooled, electric hub motors, seen in Figure 7-6, and a 21 kWh lithium ion battery pack. Each of the hub motors contained two stators, which each needed a motor controller for operation, shown in Figure 7-7.

Figure 7-6. Electric hub motors for the Mamba EV.

Figure 7-7. Motor controllers and charger mounted on the rear firewall of the Mamba EV.

7.4 Mamba EV Prototype

With the prototype of the Mamba EV completed and operational, experimental testing for the next iteration of the vehicle can commence, once a certificate of roadworthiness is obtained. The prototype of the Mamba EV is shown in Figure 7-8.

Figure 7-8. Assembled prototype of the Mamba EV.

CHAPTER 8

Discussion

The principal aim of this study was to develop the prototype chassis for the first iteration of the Mamba EV, ensuring that the structure was capable of remaining structurally sound while experiencing expected urban driving loads. The design method also aimed at being a proof of concept for flat plate composite manufacturing, in an attempt to produce a complete carbon fibre monocoque chassis on a limited budget.

The design of the Mamba EV chassis could be split into three development processes - the geometric design, the modelling of the carbon fibre composite structure layup, and the simulation of representative static loading cases. The geometric design details the development of the chassis structure, defining the physical proportions, shape, ergonomics and component mounting. The model definition details the discretisation of the geometric structure and the process of applying the selected materials to the surfaces. The load simulations detail the conditions under which the chassis was tested, and key changes and results. Finally, future developments for the Mamba EV chassis are discussed, focusing on progressing the prototype to a commercially viable product.

8.1 Geometric Design

While needing to withstand all vehicle loading, the chassis was also required to provide mounting points for all other vehicle components. Thus a spatial model of all required components was constructed to give constraints to the volume space. The spatial model allowed the determination of an optimal component layout while monitoring the influence component positioning and mounting had on vehicle handling parameters. Throughout the development of the chassis structure, emphasis was placed on component integration and post-installation accessibility.

One of the aims of the Mamba EV project was to provide an affordable alternative to current personal transport. For energy efficient vehicles, low mass is highly beneficial. To achieve this costs related to the CFRP chassis design had to be minimised, which lead to the implementation of a flat plate design methodology. By prioritising flat plate surfaces before complex curvature in chassis designs for low volume manufacture, the need for complex tooling is reduced. The development of the spatial model combined with the flat plate design ideology shaped the development of the internal chassis. It was possible to design the entire inner structure from two-dimensional flat surfaces.

8.2 Model Definition

Confidence in the simulated response the chassis structure exhibits under expected urban driving loads hinges on good correlation between the defined simulation model and the manufactured vehicle. Load safety factors and conservative design decisions may account for differences between the simulated results and the response experienced in practice, however the error between the two should be minimised. Ensuring that the modelled and real structure geometries match closely in all respects, and that the composite ply stacking configurations closely match those used in manufacture is important.

Since the aim of the study was to develop a prototype chassis to be used as a testing platform for the first iteration of the Mamba EV, certain assumptions were made in modelling the structure. Such assumptions are intended to aid in reducing the complexity of the structural model, translating to a less computationally expensive model, while not significantly influencing results. This was vital for meeting the deadlines defined in the project funding agreement. The assumptions in this case included that the composite fibres were continuous between connected panels, and that the fibres followed the material orientation angle without deviation. For the chassis, a zone-based lay-up approach was taken, which does not take into account fibre deviation during the lay-up process. This meant that the assigned materials' fibre directions would follow the material orientation angle despite running over curved planes. This simplified the modelling process, and with the entire inner structure being flat, fibre deviation during draping was of little concern. The panels for the outer surface had low curvature, which allowed for reasonably consistent fibre direction.

8.3 Simulation and Results

Structural survivability needed to be achieved in the simulation to ensure that the Mamba EV would not fail under urban driving conditions. To achieve this the defined model of the chassis was subjected to static loading conditions representing the worst case scenario loads, with the response of four parameters being monitored. Through the iterative simulation process implemented, the geometry and composite lay-up were refined, until failure indices and mechanical strength limits were not exceeded.

Initially an anticipated composite layup of four carbon plies with PVC core in key regions was used to create a starting point for the composite structure refinement. Based on the results of the initial simulations regions of high stress were identified, with the results of the monitored parameters greatly exceeding safe limits, seen in Table 5-2 to Table 5-5. Mesh refinement was done to the coarse base mesh in the regions of high stress to more accurately capture the results. The simulations were rerun with the new mesh, with the results seen in Table 6-1 to Table 6-4.

Comparing these results with the initial simulations an increase in peak elemental stresses was observed. With a coarse mesh there can be a large deviation of stress results between the integration points in an element. When the element size is reduced, the average stress of the integration points within that element can increase. This shows that mesh refinement was necessary to more accurately capture the stress in the region. Using the refined mesh, a composite ply refinement was done to strengthen the regions that exceeded the peak allowable stress and to ensure that the failure criterion were below 1, indicating that the structure would survive the applied load case. For the composite material refinement the load case with the highest value across the observed parameters was selected as a starting point. The region exhibiting the peak stress and element with the highest failure criteria was reinforced by adding a ply and the simulation rerun, after which the results were analysed. This process was iteratively run until survivability was predicted for that load case. Once all the observed parameters were within their respective limits the other load cases were re-run using the refined material layup. This process was repeated until all load case parameters were within safe limits. The final composite layup can be seen in Table 6-10 and Table 6-11. Of the operational load cases, the 2G rebound and pothole braking cases were seen to be the most severe, having a failure index of 0.822 and 0.722 respectively. The roof load case showed a higher failure index in comparison to both the 2G rebound and pothole braking load cases, 0.906, however the chances of flipping the vehicle are significantly lower and therefore the result is of less concern.

During the refinement process, several high stress regions were identified. These regions were the rear suspension mount panels, the lower edge of the motor controller air ducts, and the upper corner of the rear windscreen cut-out. It was expected that the rear suspension mounting panels would have a higher loading in comparison to the front panels, due to the 45/55 weight distribution, which resulted in an increased number of composite plies. On the rear suspension mount panels the peak stresses were found at the edge of the aluminium hardpoints used for mounting the suspension arms, and the corner of the air duct cut-out where the rear panel was bonded to the rear firewall. The high load around the hardpoints was to be expected since the load on the suspension is transmitted to the chassis at these regions. Although the flat plate design approach may reduce the cost of complex tooling, for the suspension mount panels the large flat regions are not well suited for out of plane loading. This was mitigated marginally by adding a steel cross support between the rear suspension panels, however by adding curvature to the panel there is the potential to reduce the material used in the composite layup due to the increased geometric stiffness. The cost analysis of manufacturing cost savings vs increase in material cost should be explored in future work.

8.4 Future Development

With the chassis developed in this thesis being for a first prototype, there is a large opportunity for extension to the work. For future iterations it would be advantageous to model dynamic loading, as well as to explore dynamic crash testing with an emphasis on occupant safety.

Development and manufacture of components, such as the suspension system, would be a preferable alternative to purchasing, as it would allow for more flexibility in the chassis design and provide better control of handling parameters. The prototype provides a platform to work from for future iterations and for refinement based on physical testing. Physical testing would also allow for the development of simulation load criteria based on measured results.

CHAPTER 9

Conclusion

The geometric design of the chassis structure that was developed provided suitable mounting for all vehicle subsystems, while carefully assessing the impact component positioning, particularly suspension and associated systems, had on vehicle handling parameters and ergonomics. The inner chassis structure and vehicle body were successfully integrated, with the final design being refined based on aerodynamics, component access, and model preparation for pre-processing.

During the pre-processing of the structure, the model was discretised while ensuring that the resulting mesh was continuous across all panel boundaries. The materials used in modelling the physical structure were defined, with the initial predicted composite laminate layup being assigned to relevant mesh collectors. The loads and boundary conditions for a variety of extreme urban driving conditions were defined and applied in the preliminary simulations, providing a base set of results from which the refinement of the composite laminate could be implemented.

The iterative process of refining mesh and material lay-up lead to achieving the primary aim of developing a prototype chassis that was suitable for urban driving conditions and that was predicted to survive all expected loading conditions, while fulfilling its function as an integration platform for all other subsystems of the EV. The final vehicle geometry and composite ply stacking configuration was thus completed.

Not only did the physical chassis meet the aim of developing a platform from which testing and further research can be conducted, but the structure is a proof of concept for the flat plate FRP composite design ideology, with the aim of reducing manufacturing cost and making progress towards producing an affordable and sustainable alternative to personal transport.

REFERENCES

ACP Composites. (2014). Mechanical Properties of Carbon Fiber Composite Materials, Fiber / Epoxy resin (120°C Cure) [Datasheet]. Retrieved from https://www.acpsales.com/upload/Mechanical-Properties-of-Carbon-Fiber-Composite-Materials.pdf

Adams, H. (1992). *Chassis Engineering: Chassis Design Building & Tuning for High Performance Handling*. New York: HP Books.

Adelman, H. M., & Narayanaswami, R. (1977). Evaluation of the Tensor Polynomial and Hoffman Strength Theories for Composite Materials. *Journal of Composite Materials, 11*(4), 366-377.

AlexPB. (n.d.). Resin Infusion Molding [Image]. Retrieved from http://alexpb.com/notes/wp-content/uploads/2007/12/resin_infusion_molding-diagram.jpg

Art Morrison. (n.d.). MORRISON "STRAIGHT RAIL" FRAMES [Image]. Retrieved from http://www.artmorrison.com/images/straight-profile/2014/2013-frame-pg27.jpg

ASM International. (1990). *Metals Handbook - Properties and Selection: Nonferrous Alloys and Special-Purpose Materials* (Vol. 2).

ASM International. (2001). *Composites* (Vol. 21).

AUSmotive. (2013). Frankfurt 2013: Porsche 918 Spyder [Image]. Retrieved from http://www.ausmotive.com/pics/2013/Porsche-918-Spyder-05.jpg

Barbero, E. J. (2010). *Introduction to Composite Materials Design*: CRC Press.

Barbero, E. J. (2013). *Finite Element Analysis of Composite Materials*: CRC Press.

Barnett, J. (2014). The Porsche 918 Sypder production line will blow your mind - part one. Retrieved from https://www.total911.com/the-porsche-918-spyder-production-line-will-blow-your-mind-part-one/

Beatty, M. F., Jr. (2006). Principles of Engineering Mechanics, Volume 2: Dynamics - The Analysis of Motion (pp. 50): Springer.

Bloomberg New Energy Finance. (2017). Electric Vehicle Outlook 2017.

Blundell, M., & Harty, D. (2015). *The Multibody Systems Approach to Vehicle Dynamics*: Elsevier.

BMW. (n.d.). BMW i8. Retrieved from https://www.bmwusa.com/vehicles/bmwi/bmw-i8.html

Camanho, P. P. (2002). FAILURE CRITERIA FOR FIBRE-REINFORCED POLYMER COMPOSITES.

Campbell, F. C. (2010). *Structural Composite Materials*: ASM International.

Cheah, L. W. (2010). *Cars on a Diet: The Material and Energy Impacts of Passenger Vehicle Weight Reduction in the U.S.* (Doctoral Dissertation), Massachusetts Institute of Technology.

Costin, M., & Phipps, D. (1961). *Racing and Sports Car Chassis Design*: B. T. Batsford LTD.

Danielsson, O., & Cocaña, A. G. (2015). *Influence of Body Stiffness on Vehicle Dynamics Characteristics in Passenger Cars*. (Master's thesis), Chalmers University Of Technology.

Enertrac Corporation. (n.d.). MHM602 & MHM603. Retrieved from http://www.enertrac.net/images/productspecs.pdf

Engineered Cramer Composites. (1994). Technical Datasheet [Datasheet]. Retrieved from http://www.amtcomposites.co.za/sites/default/files/media/data-sheets/ECC_Style452_E.pdf

FactoryFive. (n.d.). GTM Supercar Design [Image]. Retrieved from https://www.factoryfive.com/wp-content/uploads/2012/02/gtmframe-694x413.jpg

Ferrari. (n.d.). LaFerrari. Retrieved from https://auto.ferrari.com/en_EN/sports-cars-models/past-models/laferrari/

Ford. (2017, Jan 3). FORD ADDING ELECTRIFIED F-150, MUSTANG, TRANSIT BY 2020 IN MAJOR EV PUSH; EXPANDED U.S. PLANT TO ADD 700 JOBS TO MAKE EVS, AUTONOMOUS CARS [Press release]. Retrieved from https://media.ford.com/content/fordmedia/fna/us/en/news/2017/01/03/ford-adding-electrified-f-150-mustang-transit-by-2020.html

Forest Products Laboratory. (1999). *Wood Handbook: Wood as an Engineering Material*.

Graf, M., Fries, E., Renkl, J., Henning, P. D. F., Chaudhari, R., & Thoma, B. (n.d.). HP- RTM - Process Advancements. Retrieved from http://www.3dnanocomposites.com/uploads/Dieffenbacher-ET5-2010.pdf

Gurit. (n.d.-a). Ampreg 21: Epoxy Wet Laminating System [Datasheet]. Retrieved from http://www.gurit.com/-/media/Gurit/Datasheets/ampreg-21.ashx

Gurit. (n.d.-b). Gurit® Corecell™ M THE MARINE FOAM [Datasheet]. Retrieved from http://www.gurit.com/-/media/Gurit/Datasheets/guritcorecell-m.ashx

Happian-Smith, J. (2001). *An Introduction to Modern Vehicle Design*.

International Energy Agency. (2016). Global EV Outlook 2016.

International Energy Agency. (2017). Global EV Outlook 2017.

Koenigsegg. (n.d.). THE REGERA - A NEW ERA. Retrieved from https://www.koenigsegg.com/regera/

Kong, B. (2013). THE HYPERCAR BLUEPRINT - 2014 MCLAREN P1. Retrieved from http://www.motortrend.com/news/hypercar-blueprint/

Logan, D. L. (2011). *A First Course in the Finite Element Method* (5th ed.): Cengage Learning.

Lotus Cars Ltd. (1996). Service Notes - Elise. Retrieved from https://elise.bidouille.info/docs/LotusEliseS1-ServiceManual.pdf

Mallick, P. K. (2007). Fiber-Reinforced Composites: Materials, Manufacturing, and Design (3rd ed.): CRC Press.

McLaren. (n.d.). P1 - Design and Innovation. Retrieved from http://cars.mclaren.com/ultimate-series/p1/design-and-innovation

Meywerk, M. (2015). *Vehicle Dynamics*: Wiley.

Milliken, W. F., & Milliken, D. L. (1995). *Race Car Vehicle Dynamics*: Society of Automotive Engineers.

Multitex Composites. (n.d.). Vacuum Bagging Tooling [Image]. Retrieved from http://www.multitex-composites.com/images/Picture_Kapitel__Vacuum_Bagging_Tooling.jpg

National Center for Health Statistics. (2018). National Health and Nutrition Examination Survey. Retrieved from https://www.cdc.gov/nchs/nhanes/index.htm

NetComposites. (n.d.). Woven Fabrics. Retrieved from http://www.netcomposites.com/guide/woven-fabrics/40

Pauwelussen, J. P. (2014). *Essentials of Vehicle Dynamics*: Elsevier.

Puhn, F. (1976). *How To Make Your Car Handle*: H.P. Books.

Reimpell, J., Stoll, H., & Betzler, J. W. (2001). *The Automotive Chassis: Engineering Principles* (Second ed.): Butterworth-Heinemann.

RIMAC. (n.d.). CONCEPT_ONE - THE SUPERCAR OF THE FUTURE. TODAY. Retrieved from http://www.rimac-automobili.com/en/supercars/concept_one/

Sheahan, M. (2017, Dec 21). BMW aims to have sold 500,000 hybrid, electric cars by end-2019. *Reuters*. Retrieved from https://www.reuters.com/article/us-bmw-electric/bmw-aims-to-have-sold-500000-hybrid-electric-cars-by-end-2019-idUSKBN1EF0TY

Siemens PLM Software (Producer). (2013). MT15029: NX Laminate Composites. [PowerPoint Slides]

Sim, B., Woods, D., Mons, S., & Chetty, S. (2016). *Design and research project 2 - Second semester report* University of KwaZulu-Natal.

Speed Industries. (2011). Nissan Skyline - The R Platform [Image]. Retrieved from http://www.speed-industries.ch/wordpress/wp-content/uploads/2011/03/mcpherson_2wish.jpg

Tesla. (n.d.). Model S - The Best Car. Retrieved from https://www.tesla.com/models

The Truth About Cars. (n.d.). The Most Influential Sports Car Ever Made?: The Lotus Elan [Image]. Retrieved from http://www.thetruthaboutcars.com/wp-content/uploads/2014/08/toyota2000gtframe.jpg

Thompson, C. (2017, Nov 15). Everything Tesla wants to accomplish by 2020. *Business Insider*. Retrieved from http://www.businessinsider.com/tesla-expansion-plans-2-years-2017-11/#finish-building-its-giant-battery-plant-called-gigafactory-1-1

Toyota. (2017, Dec 18). Toyota Aims for Sales of More Than 5.5 Million Electrified Vehicles Including 1 Million Zero-Emission Vehicles per Year by 2030 [Press release]. Retrieved from https://newsroom.toyota.co.jp/en/corporate/20353243.html

Tsai, S. W., & Wu, E. M. (1971). A general theory of strength for anisotropic materials. *Journal of Composite Materials, Vol 5*, 58-80.

Tutu, A. (2016). Koenigsegg Regera Carbon Chassis Surfaces, Looks Like Stripped-Down Track Car. Retrieved from https://www.autoevolution.com/news/koenigsegg-regera-carbon-chassis-surfaces-looks-like-stripped-down-track-car-111414.html#

U.S. Army Natick Soldier Research Development and Engineering Center. (2014). *2012 ANTHROPOMETRIC SURVEY OF U.S. ARMY PERSONNEL: METHODS AND SUMMARY STATISTICS*. Retrieved from www.dtic.mil/get-tr-doc/pdf?AD=ADA611869

U.S. Department of Transportation. (2012). *Aviation Maintenance Technician Handbook - Airframe* (Vol. 1).

United Nations Framework Convention on Climate Change. (2015). Adoption of the Paris Agreement. Retrieved from https://unfccc.int/resource/docs/2015/cop21/eng/l09.pdf

US Department of Defense. (2002). *MIL-HDBK-17-3F: COMPOSITE MATERIALS HANDBOOK VOLUME 3. POLYMER MATRIX COMPOSITES MATERIALS USAGE, DESIGN, AND ANALYSIS.*

Volkswagen plans electric option for all models by 2030. (2017, Sept 11). *BBC News*. Retrieved from http://www.bbc.com/news/business-41231766

Waldmeir, P. (2017, Oct 2). GM aims to have 20 all-electric car models by 2023. *Financial Times*. Retrieved from https://www.ft.com/content/1b6319bf-8b82-3b5a-b84c-0f6037124f89

Woods, M. A. R. (2018). *DEVELOPMENT OF A COMPREHENSIVE ENERGY MODEL TO SIMULATE THE ENERGY EFFICIENCY OF A BATTERY ELECTRIC VEHICLE TO ALLOW FOR PROTOTYPE DESIGN OPTIMISATION AND VALIDATION.* University of KwaZulu-Natal.

APPENDIX A

Material Properties

Table A-1. Carbon fibre and epoxy ply experimental data obtained from DUT Composite Research Lab.

Property	Symbol	Units	0/90	Uni-dir.	-45/+45
In-plane elastic modulus - 0°	E_1	GPa	47	100.2	11.75
In-plane elastic modulus - 90°	E_2	GPa	47	5.73	11.75
In-plane shear modulus	G_{12}	GPa	5.1	3.24	24.3
Poisson Ratio	ν_{12}		0.05	0.32	0.8
Ult. Tensile strength - 0°	F_{1t}	MPa	464.4	1000	92.88
Ult. Tensile strength - 90°	F_{2t}	MPa	464.4	26	92.88
Ult. Compressive strength - 0°	F_{1c}	MPa	286.6	550	85.98
Ult. Compressive strength - 90°	F_{2c}	MPa	286.6	78	85.98
Ult. In-plane shear strength	F_4	MPa	53.4	47.6	213.6

Table A-2. Aramid fibre and epoxy ply material properties (ACP Composites, 2014).

Property	Symbol	Units	0/90
In-plane elastic modulus - 0°	E_1	GPa	30
In-plane elastic modulus - 90°	E_2	GPa	30
In-plane shear modulus	G_{12}	GPa	5
Poisson Ratio	ν_{12}		0.2
Ult. Tensile strength - 0°	F_{1t}	MPa	480
Ult. Tensile strength - 90°	F_{2t}	MPa	480
Ult. Compressive strength - 0°	F_{1c}	MPa	190
Ult. Compressive strength - 90°	F_{2c}	MPa	190
Ult. In-plane shear strength	F_4	MPa	50

Table A-3. Glass fibre and epoxy ply material properties (ACP Composites, 2014).

Property	Symbol	Units	0/90
In-plane elastic modulus - 0°	E_1	GPa	25
In-plane elastic modulus - 90°	E_2	GPa	25
In-plane shear modulus	G_{12}	GPa	4
Poisson Ratio	ν_{12}		0.2
Ult. Tensile strength - 0°	F_{1t}	MPa	440
Ult. Tensile strength - 90°	F_{2t}	MPa	440
Ult. Compressive strength - 0°	F_{1c}	MPa	425
Ult. Compressive strength - 90°	F_{2c}	MPa	425
Ult. In-plane shear strength	F_4	MPa	40

Table A-4. Gurit CoreCell M60 PVC core material properties (Gurit, n.d.-b).

Property	Symbol	Units	0/90
In-plane elastic modulus - 0°	E_1	MPa	44
In-plane elastic modulus - 90°	E_2	MPa	44
In-plane shear modulus	G_{12}	MPa	20
Poisson Ratio	ν_{12}		0.3
Ult. Tensile strength - 0°	F_{1t}	MPa	0.81
Ult. Tensile strength - 90°	F_{2t}	MPa	0.81
Ult. Compressive strength - 0°	F_{1c}	MPa	0.55
Ult. Compressive strength - 90°	F_{2c}	MPa	0.55
Ult. In-plane shear strength	F_4	MPa	0.68

Table A-5. Gurit CoreCell M80 PVC core material properties (Gurit, n.d.-b).

Property	Symbol	Units	0/90
In-plane elastic modulus - 0°	E_1	MPa	72
In-plane elastic modulus - 90°	E_2	MPa	72
In-plane shear modulus	G_{12}	MPa	29
Poisson Ratio	ν_{12}		0.3
Ult. Tensile strength - 0°	F_{1t}	MPa	1.62
Ult. Tensile strength - 90°	F_{2t}	MPa	1.62
Ult. Compressive strength - 0°	F_{1c}	MPa	1.02
Ult. Compressive strength - 90°	F_{2c}	MPa	1.02
Ult. In-plane shear strength	F_4	MPa	1.09

Table A-6. Plywood core material properties (Forest Products Laboratory, 1999).

Property	Symbol	Units	0/90
In-plane elastic modulus - 0°	E_1	GPa	13.1
In-plane elastic modulus - 90°	E_2	GPa	13.1
In-plane shear modulus	G_{12}	GPa	0.761
Poisson Ratio	ν_{12}		0.26
Ult. Tensile strength - 0°	F_{1t}	MPa	27.6
Ult. Tensile strength - 90°	F_{2t}	MPa	27.6
Ult. Compressive strength - 0°	F_{1c}	MPa	34.5
Ult. Compressive strength - 90°	F_{2c}	MPa	34.5
Ult. In-plane shear strength	F_4	MPa	7.6

Table A-7. Aluminium core material properties (ASM International, 1990).

Property	Symbol	Units	0/90
In-plane elastic modulus - 0°	E_1	GPa	68.9
In-plane elastic modulus - 90°	E_2	GPa	68.9
In-plane shear modulus	G_{12}	GPa	26
Poisson Ratio	ν_{12}		0.33
Ult. Tensile strength - 0°	F_{1t}	MPa	310
Ult. Tensile strength - 90°	F_{2t}	MPa	310
Ult. Compressive strength - 0°	F_{1c}	MPa	310
Ult. Compressive strength - 90°	F_{2c}	MPa	310
Ult. In-plane shear strength	F_4	MPa	207

APPENDIX B

Load Calculations

3G Bump Calculation

3G bump load for the front wheels,

$$F_z = 3mg$$
$$F_z = (3)(155.2)(9.81) \quad \text{(B.1)}$$
$$F_z = 4567.54\ N$$

3G bump load for the rear wheels.

$$F_z = 3mg$$
$$F_z = (3)(180)(9.81) \quad \text{(B.2)}$$
$$F_z = 5297.4\ N$$

2G Rebound Calculation

2G rebound load for the front wheels,

$$F_z = 2mg$$
$$F_z = (2)(155.2)(9.81) \quad \text{(B.3)}$$
$$F_z = 3045.02\ N$$

2G rebound load for the rear wheels,

$$F_z = 2mg$$
$$F_z = (2)(180)(9.81) \quad \text{(B.4)}$$
$$F_z = 3531.6\ N$$

0.75G Cornering Calculations

The lateral load experienced by the vehicle while cornering at 0.75G,

$$F_y = m\ g\ a$$
$$F_y = (0.75)(669.74)(9.81) \quad \text{(B.5)}$$
$$F_y = 4927.61\ N$$

The front roll stiffness of the vehicle,

$$C_1 = 2\left(\frac{s_1}{2}\right)^2 k_1$$

$$C_1 = 2\left(\frac{0.86}{2}\right)^2 (46592) \tag{B.6}$$

$$C_1 = 17229.7\ Nm/deg$$

The rear roll stiffness of the vehicle,

$$C_2 = 2\left(\frac{s_2}{2}\right)^2 k_2$$

$$C_2 = 2\left(\frac{0.8}{2}\right)^2 (84108) \tag{B.7}$$

$$C_2 = 26914.6\ Nm/deg$$

The difference in vertical load on the front wheels while cornering,

$$\Delta F_{f,z} = \left(\frac{C_1}{C_1 + C_2}\right)\left(\frac{hF_y}{t_1}\right)$$

$$\Delta F_{f,z} = \left(\frac{17229.7}{17229.7 + 26914.6}\right)\left(\frac{(0.396)(4927.61)}{1.51}\right) \tag{B.8}$$

$$\Delta F_{f,z} = 504.38\ \text{N}$$

The difference in vertical load on the rear wheels while cornering,

$$\Delta F_{r,z} = \left(\frac{C_2}{C_1 + C_2}\right)\left(\frac{hF_y}{t_2}\right)$$

$$\Delta F_{f,z} = \left(\frac{26914.6}{17229.7 + 26914.6}\right)\left(\frac{(0.396)(4927.61)}{1.495}\right) \tag{B.9}$$

$$\Delta F_{f,z} = 795.8\ \text{N}$$

The vertical load on the inner front wheel while cornering at 0.75G,

$$F_{f,z(inner)} = m_f g - \Delta F_{f,z}$$

$$F_{f,z(inner)} = (155.2)(9.81) - 504.38 \tag{B.10}$$

$$F_{f,z(inner)} = 1018.53\ N$$

The vertical load on the outer front wheel while cornering at 0.75G,

$$F_{f,z(outer)} = m_f g + \Delta F_{f,z}$$
$$F_{f,z(outer)} = (155.2)(9.81) + 504.38 \quad \text{(B.11)}$$
$$F_{f,z(outer)} = 2026.49\ N$$

The vertical load on the inner rear wheel while cornering at 0.75G,

$$F_{r,z(inner)} = m_r g - \Delta F_{r,z}$$
$$F_{r,z(inner)} = (180)(9.81) - 795.8 \quad \text{(B.12)}$$
$$F_{r,z(inner)} = 970.64\ N$$

The vertical load on the outer rear wheel while cornering at 0.75G,

$$F_{r,z(outer)} = m_r g + \Delta F_{r,z}$$
$$F_{r,z(outer)} = (180)(9.81) + 795.8 \quad \text{(B.13)}$$
$$F_{r,z(outer)} = 2560.96\ N$$

The lateral load on the inner front wheel while cornering at 0.75G,

$$F_{f,y(inner)} = \mu F_{f,z(inner)}$$
$$F_{f,y(inner)} = (0.75)(1018.53) \quad \text{(B.14)}$$
$$F_{f,y(inner)} = 763.9\ N$$

The lateral load on the outer front wheel while cornering at 0.75G,

$$F_{f,y(outer)} = \mu F_{f,z(outer)}$$
$$F_{f,y(outer)} = (0.75)(2026.49) \quad \text{(B.15)}$$
$$F_{f,y(outer)} = 1519.87\ N$$

The lateral load on the inner rear wheel while cornering at 0.75G,

$$F_{r,y(inner)} = \mu F_{r,z(inner)}$$
$$F_{r,y(inner)} = (0.75)(970.64) \quad \text{(B.16)}$$
$$F_{r,y(inner)} = 727.98\ N$$

The lateral load on the outer rear wheel while cornering at 0.75G,

$$F_{r,y(outer)} = \mu F_{r,z(outer)}$$
$$F_{r,y(outer)} = (0.75)(2560.96) \quad \text{(B.17)}$$
$$F_{r,y(outer)} = 1920.72\ N$$

1G Braking Calculation

The vertical load on the rear wheels while the vehicle brakes with a 1G deceleration,

$$F_{r,z} = \frac{m}{L}\left(gL_f - ah\right)$$
$$F_{r,z} = \frac{669.74}{2.35}\left((9.81)(1.26) - (9.81)(0.396)\right) \quad \text{(B.18)}$$
$$F_{r,z} = 2409.84\ N$$

The longitudinal load on the rear wheels while the vehicle brakes with a 1G deceleration,

$$F_{r,x} = \mu F_{r,z}$$
$$F_{r,x} = (0.75)(2409.84) \quad \text{(B.19)}$$
$$F_{r,x} = 1807.4\ N$$

The vertical load on the front wheels while the vehicle brakes with a 1G deceleration,

$$F_{f,z} = \frac{m}{L}(gL_r + ah)$$
$$F_{f,z} = \frac{669.74}{2.35}\left((9.81)(1.09) + (9.81)(0.396)\right) \quad \text{(B.20)}$$
$$F_{f,z} = 4164.04\ N$$

The longitudinal load on the front wheels while the vehicle brakes with a 1G deceleration,

$$F_{f,x} = \mu F_{f,z}$$
$$F_{f,x} = (0.75)(4164.04) \quad \text{(B.21)}$$
$$F_{f,x} = 3123.03\ N$$

0.35G Reverse Braking

The vertical load on the rear wheels while the vehicle reverse brakes with a 0.35G deceleration,

$$F_{r,z} = \frac{m}{L}(gL_f + ah)$$

$$F_{r,z} = \frac{669.74}{2.35}\big((9.81)(1.26) + (0.35)(9.81)(0.396)\big) \quad \text{(B.22)}$$

$$F_{r,z} = 3903.28\ N$$

The longitudinal load on the rear wheels while the vehicle reverse brakes with a 0.35G deceleration,

$$F_{r,x} = \mu F_{r,z}$$

$$F_{r,x} = (0.75)(3903.28) \quad \text{(B.23)}$$

$$F_{r,x} = 2927.46\ N$$

The vertical load on the front wheels while the vehicle reverse brakes with a 0.35G deceleration,

$$F_{f,z} = \frac{m}{L}(gL_r - ah)$$

$$F_{f,z} = \frac{669.74}{2.35}\big((9.81)(1.09) - (0.35)(9.81)(0.396)\big) \quad \text{(B.24)}$$

$$F_{f,z} = 2670.6\ N$$

The longitudinal load on the front wheels while the vehicle reverse brakes with a 0.35G deceleration,

$$F_{f,x} = \mu F_{f,z}$$

$$F_{f,x} = (0.75)(2670.6) \quad \text{(B.25)}$$

$$F_{f,x} = 2002.95\ N$$

Torsional Stiffness

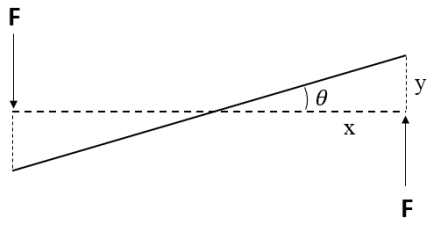

Figure B-1. Diagram for calculating torsional stiffness.

The initial chassis torsional stiffness, based on the initial predicted composite lay-up,

$$k_{chassis,i} = \frac{F\,x}{\tan^{-1}(\theta)}$$

$$k_{chassis,i} = \frac{1000(1.51)}{\tan^{-1}\left(2.408/755\right)} \tag{B.26}$$

$$k_{chassis,i} = 8263.16\ Nm/deg$$

The final chassis torsional stiffness, based on the refined composite lay-up,

$$k_{chassis,f} = \frac{F\,x}{\tan^{-1}(\theta)}$$

$$k_{chassis,f} = \frac{1000(1.51)}{\tan^{-1}\left(1.613/755\right)} \tag{B.27}$$

$$k_{chassis,f} = 12335.81\ Nm/deg$$